JYU DISSERTATIONS 604

Joonas Ojala

Combined γ-ray and Electron Spectroscopy

Study of Shape Coexistence in ^{186}Pb

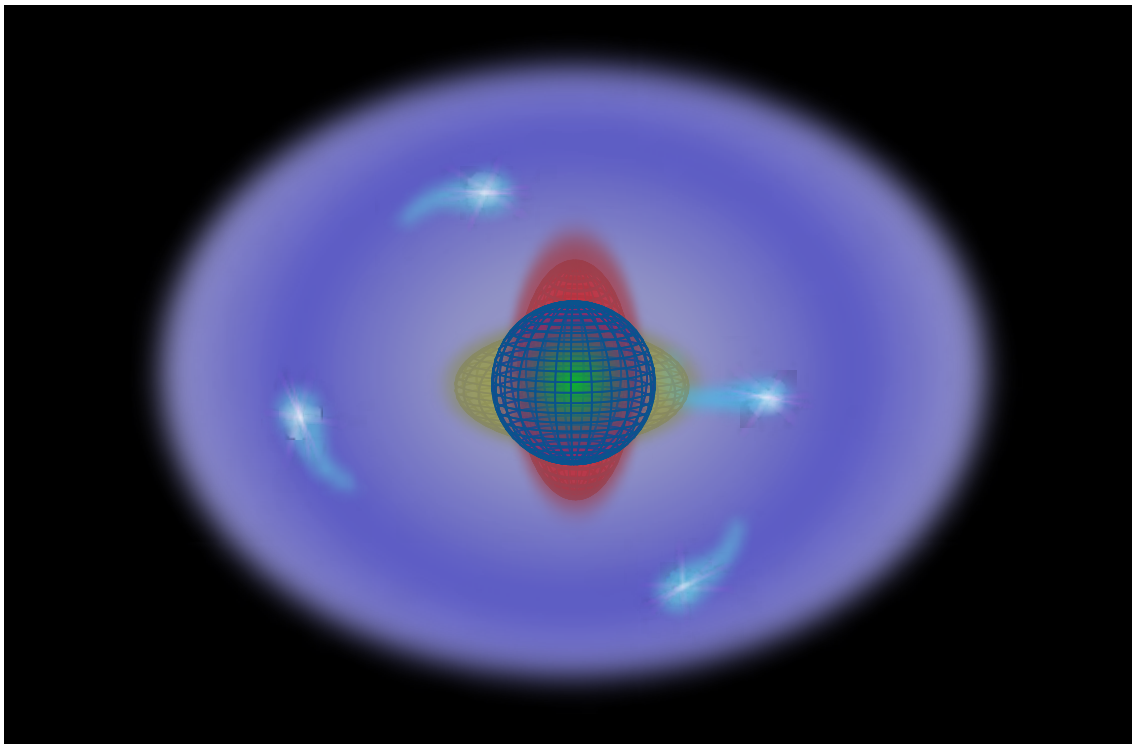

UNIVERSITY OF JYVÄSKYLÄ
FACULTY OF MATHEMATICS
AND SCIENCE

JYU DISSERTATIONS 604

Joonas Ojala

Combined γ-ray and Electron Spectroscopy

Study of Shape Coexistence in ^{186}Pb

Esitetään Jyväskylän yliopiston matemaattis-luonnontieteellisen tiedekunnan suostumuksella
julkisesti tarkastettavaksi yliopiston Ylistönrinteen salissa FYS1
maaliskuun 3. päivänä 2023 kello 12.

Academic dissertation to be publicly discussed, by permission of
the Faculty of Mathematics and Science of the University of Jyväskylä,
in Ylistönrinne, auditorium FYS1, on March 3, 2023, at 12 o'clock.

JYVÄSKYLÄN YLIOPISTO
UNIVERSITY OF JYVÄSKYLÄ

JYVÄSKYLÄ 2023

Editors
Ilari Maasilta
Department of Physics, University of Jyväskylä
Päivi Vuorio
Open Science Centre, University of Jyväskylä

ISBN 978-951-39-9288-0 (PDF)
URN:ISBN:978-951-39-9288-0
ISSN 2489-9003

ABSTRACT

Ojala, Joonas
Combined γ-ray and electron spectroscopy: Study of shape coexistence in ^{186}Pb
Jyväskylä: University of Jyväskylä, 2023, 96 p.
(JYU Dissertations
ISSN 2489-9003; 604)
ISBN 978-951-39-9288-0 (PDF)
Diss.

Structures in ^{186}Pb have been under extensive investigation for several decades. ^{186}Pb is the system having a low-lying triplet of zero-spin states, which are assigned with different shapes (spherical, prolate and oblate). This nucleus has been previously studied using α-decay and in-beam γ-ray spectroscopic methods but the transitions near the ground state remained a mystery due to the large conversion coefficient. In this thesis, the low-lying structure of ^{186}Pb was experimentally investigated by combined γ-ray and electron spectrometer, SAGE, and utilising the recoil-decay tagging method. As a result, the $E0$ $2_2^+ \rightarrow 2_1^+$ and $4_2^+ \rightarrow 4_1^+$ interband transitions could be assessed. Also, the feeding of the first excited 0_2^+ state was observed for the first time. Results allowed for reassigning the shapes of 0^+ states in ^{186}Pb, which provide input for new theoretical calculations.

Recent developments for in-beam γ-ray spectroscopy at the Accelerator Laboratory of Jyväskylä forms part of this thesis work. The properties of the JUROGAM 3 germanium array, such as energy resolution, add-back factor and photopeak detection efficiency, can be found in the fifth chapter. Also, the sum-peak method to determine the absolute photopeak detection efficiency of a germanium array is explained in this chapter. The issue with pile-up marking in the DAQ system is also raised to notify other potential users.

Keywords: Shape coexistence, conversion electron spectroscopy, γ-ray spectroscopy, SAGE, JUROGAM 3.

TIIVISTELMÄ (ABSTRACT IN FINNISH)

Väitöskirjassa käsitellään tutkimustuloksia ^{186}Pb-ytimen rakenteista lähellä perustilaa, jotka on kerätty käyttäen yhdistettyä gamma- ja konversioelektronispektrometristä menetelmää. ^{186}Pb-ydin poikkeaa kaikista tunnetuista ytimistä siten, että se on ainoa tunnettu tapaus, jossa kolmen alimman viritystilan kokonaispyörimismäärä on nolla. Tätä ydintä on aikaisemmin tutkittu käyttäen alfahajoamis- ja gammaspektroskopisia menetelmiä. Niissä kokeissa havaittiin alimmat 0^+ viritystilat ja oletettavasti niiden päälle muodostuneet pyörimissarjat, jotka on tulkittu olevan prolaatin ja oblaatin muodon pyörimissarjoiksi. Osa ytimen siirtymistä ovat jääneet aikaisemmissa tutkimuksissa havaitsematta siirtymien suurista konversiokertoimista johtuen. Työssä esitelty mittaus suoritettiin Jyväskylän yliopiston kiihdytinlaboratoriossa käyttäen SAGE spektrometria ja rekyyli-hajoamis-merkitsemis-menetelmää (RDT). Työssä havaittiin ensimmäistä kertaa pyörimissarjojen väliset $2_2^+ \rightarrow 2_1^+$ ja $4_2^+ \rightarrow 4_1^+$ $E0$ siirtymät, sekä alimman 0^+ viritystilan syöttö. Tulosten avulla onnistuimme uudelleen määrittelemään ^{186}Pb 0^+ viritystilojen muodot. Tulokset antavat lisäinformaatiota uusille teoreettisille laskuille.

Väitöskirja sisältää myös osion gammaspektroskopisten mittalaitteiden kehitystyöstä Jyväskylän yliopiston kiihdytinlaboratoriossa. JUROGAM 3 -germaniumilmaisinjärjestelmän ominaisuuksia energiaresoluutio eri konfiguraatioissa sekä järjestelmälle ominainen gammasirontatekijä (add-back factor) ja absoluuttinen havaitsemistehokkuus määritettynä summapiikkimenetelmän avulla esitetään viidennessä kappaleessa. Tiedonkeruujärjestelmän (DAQ) kasautumismerkinnässä (pile-up marking) havaittu ongelma on tuotu esiin mahdollisten käyttäjien tiedostettavaksi.

Avainsanat: Muotojen rinnakkaiselo, konversioelektronispektroskopia, gammaspektroskopia, SAGE, JUROGAM 3

Author

Joonas Ojala
Department of Physics
University of Jyväskylä
Jyväskylä, Finland

Supervisor

Dr Janne Pakarinen
Department of Physics
University of Jyväskylä
Jyväskylä, Finland

Reviewers

Dr Martin Venhart
Department of Nuclear Physics
Slovak Academy of Sciences
Bratislava, Slovakia

Dr Kerttuli Helariutta
Department of Physics
University of Helsinki
Helsinki, Finland

Opponent

Dr Daniel Doherty
Department of Physics
University of Surrey
Surrey, United Kingdom

PREFACE

This journey was indeed a longer and more eventful experience than I anticipated. I want to thank my supervisor Dr Janne Pakarinen for introducing me to γ-ray and and conversion electron spectroscopy. Even PhD did not go as it was planned initially, I am happy with the outcome of this work. I also want to express my gratitude to Professor Rauno Julin for his insights about nuclear structure physics, especially with interpretation $E0$ transitions.

I also want to express my gratitude the Nuclear Spectroscopy group for taking me as part of their member. I want to thank especially Dr Juha Uusitalo for his support and vast knowledge about nuclear reactions, decay spectroscopy and ion optics. Also, I would like to thanks for Dr Jan Sarén for introducing me in the physics department in my first year and pushing me to think out of the box. Special thanks to Dr Andrés Illana-Sison, who was there throwing ideas with me for my analysis and being co-spokesperson for the successful ^{185}Hg experiment (We probably made a record of breaking the SOD and DOS cards there!) Also, in memory of Jari Partanen, who gave me an introduction to electronics and taught me that there is always room for some capacitors, you are truly missed.

The colleagues who did the work in the laboratory, detector hospital and measurement room enjoyable, Minna, Holly, Ulrika, George, Andy, Alvaro, Kalle, Jussi and Adrian, thank you for these years. Thanks, Andy, for proofreading the manuscript, I really appreciated it! I also want to thank all the FL125 officemates for make the environment for enjoyable and fun. In that office, I was under the influence of French and Spanish languages (Currently, I recognise lots of words without knowing the meaning of those words.)

This thesis would not be possible without time-to-time breaks from it. All lunch discussions, sports activities, music events and having just a couple of excellent pints. I owe huge thanks for sharing these moments with Jyrki, Topi, Janne, Teemu, Oskari, Henri, Joni, Tero, Sarina, Marjut, Arus, Elise, Ana, Hussam, Criss, Marek, Jorge, Alex, Andrea,... and many more.

Kiitokset myös seinäjokisille kavereille, sukulaisille, vanhemmille ja siskolle tuesta ja kannustuksesta näinä vuosina. Se on ollut äärimmäisen tärkeää, että on pystynyt jatkamaan tällä uralla. Ja lopuksi, muttei vähäisemmäksi, kiitos Henna loputtomasta tuesta ja oikolukemisesta! Jouduit kuuntelemaan paljon valitusta tästä yhdestä kirjasta, mutta nyt se on ohi! Lupaan tehdä saman muutaman vuoden päästä!

Liverpool, November 2022

Joonas Ojala

ACRONYMS

ACC-LAB	The Accelerator Laboratory of the University of Jyväskylä
BGO	Bismuth germanate
Coulex	Coulomb excitation
DAQ	Data acquisition
DoS	Differential to Single-ended
DSSDs	Double-sided silicon strip detectors
Δ E	Energy loss
GO cards	Gain and offset cards
HV	High voltage
MWD	Moving window deconvolution
MWPC	Multi-wire proportional counter
RDT	Recoil-decay-tagging; recoil-gated α-particle tagged
RDDS	Recoil distance doppler shift
SoD	Single-ended to differential
TDR	Total data readout
ToF	Time-of-flight
VMI	Variable moment of inertia
W. u.	Weisskopf unit

LIST OF PUBLICATIONS

P1 Joonas Ojala, Janne Pakarinen, Philippos Papadakis, ..., Robert Wadsworth . Reassigning the shapes of the 0^+ states in the ^{186}Pb nucleus. *Communications Physics* **5**, *213 (2022) doi: 10.1038/s42005-022-00990-4*.

P2 Janne Pakarinen, Joonas Ojala, Panu Ruotsalainen, ..., George Zimba. The JUROGAM 3 spectrometer. *The European Physical Journal A* ***56****, 149 (2020) doi: 10.1140/epja/s10050-020-00144-6*.

AUTHOR'S CONTRIBUTION

P1: The author did the analysis, contributed in the writing of the manuscript and was part of interpreting the data.
P2: The author was part of installing team of JUROGAM 3, analysed the source test data and participated in preparation of the manuscript.

In addition, the author has participated in installation of the SPEDE spectrometer in the IDS station at CERN-ISOLDE and the SAGE spectrometer in conjunction with the MARA separator. The author was the spokesperson and liaison in the experiment studying ^{185}Hg using SAGE in conjunction with the MARA separator. The author contributed to the experimental part and the writing process of 21 peer-reviewed publications for measurements performed at JYFL, Finland (15) and CERN-ISOLDE, Switzerland (6).

CONTENTS

1 INTRODUCTION

An atomic nucleus consist of particles, protons and neutrons, commonly known as nucleons. The number of nucleons varies, which makes nuclei diverse laboratory for studying quantum many-body systems. Theories to describe these many-body systems have been developed from a simple shell model theory by Mayer *et al.* [1], to more elegant theoretical models which describe the heavy nuclei. For example, rotational models [2], mean-field approach [3], interactive boson model [4], and Monte Carlo shell model [5] are used to describe the heavy nuclei. The theoretical description is complex for heavy nuclei as the number of nucleon-nucleon correlations increases rapidly with increasing mass number. One indication of collective behaviour is the rotation of nuclei which are distorted from spherical shape and these nuclei are called as deformed nuclei.

Nuclei can exhibit different deformed shapes such as prolate and oblate. Different deformations can be found in the same nucleus, a phenomenon known as shape coexistence. One of the most exciting regions for shape coexistence lies near the neutron $N = 104$ midshell with proton number Z close to 82. This part of the nuclear chart is shown in Figure 1.1.

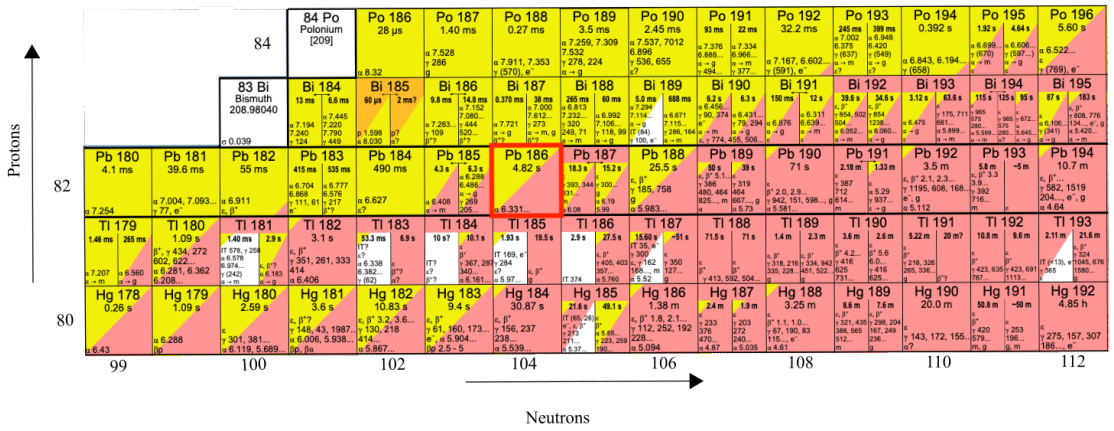

FIGURE 1.1 Detailed view of the nuclear chart in the neutron-deficient lead region. The ^{186}Pb nucleus studied in this work is highlighted with a red box. The different decay modes are indicated by different colours. Yellow represents α decay, red represents for β^+/EC decay, and orange represents for proton decays. Non-observed isomeric decay branches are marked with small white boxes. Nuclear chart is take from [6].

In atomic nucleus, transitions between states can proceed typically via electric quadrupole transition, known as $E2$ transition, or magnetic dipole de-excitation, known as $M1$ transition, depending on the spin and parity of the initial and final state. The de-excitation of nucleus usually happens by emitting a γ-ray but there is an alternative de-excitation mode through internal conversion. In internal conversion, the transition energy is transferred to an atomic electron, which is emitted from the atomic orbital. In special case, transitions can only happen through internal conversion, known as electric monopole ($E0$) transition, and these types of transitions are common in nuclei with the shape coexistence [7]. The $E0$ transition is often seen as a fingerprint for configuration mixing between different shapes [7].

This thesis focuses on experimental results obtained in a simultaneous in-beam electron and γ-ray spectroscopic measurement of ^{186}Pb. Theoretical calculations have predicted multiple shapes in the ^{186}Pb nucleus. These shapes were previously studied through α-decay study of ^{190}Po [8] and γ-ray spectroscopic experiments [9, 10]. In the α-decay studies of ^{190}Po, the band-heads of different deformed structures were observed for the first time. The rotational structures of yrast and non-yrast structures (assigned as prolate and oblate shape) were examined utilising γ-ray spectroscopy but the feeding transitions to band-head states remained unobserved.

Combined in-beam γ-electron spectroscopy is a powerful tool in searches for the $E0$ transitions. In this work, combined in-beam γ-electron spectroscopy was used to study the ^{186}Pb utilising the SAGE spectrometer to obtain more information

about the band-head states and configuration mixing between the yrast and non-yrast bands. The results of this thesis work revealed the feeding of one of the band-head states. This work also allowed to reassign of the band-head states. These new results also allowed for evaluating the configuration mixing of the 2_1^+ and 4_1^+ states. The results of this work will provide more input to theoretically study the quantum many-body systems and shape coexistence in the neutron-deficient Pb region.

This thesis also includes the development work done with in-beam arrays in the Accelerator Laboratory of Jyväskylä. The new JUROGAM 3 spectrometer [11] was installed during spring 2019. The JUROGAM 3 array is movable between the MARA and the RITU separators. Moving JUROGAM 3 between MARA and RITU separators broadens access to a different region of the nuclear chart as the RITU separator is developed for mass region $Z \geq 82$ and MARA for lighter mass nuclei using symmetric and inverse kinematics fusion-evaporation reactions. The MARA separator experiments are focused for nuclei around the $N = Z$ line.

2 THEORETICAL BACKGROUND

2.1 Electromagnetic transitions in nuclei

Electromagnetic transitions can occur between nuclear states. An excited nucleus de-excites by emitting γ rays or conversion electrons*. States are characterized by angular momentum and parity, transitions are characterized with transition type (electric E or magnetic M) and multipole order.

The angular momentum of the de-excitation process follows the triangular rule

$$\left|I_i - I_f\right| \leq L \leq I_i + I_f \tag{2.1}$$

where I_i (I_f) is the angular momentum of the initial (final) state and multipolarity L is an integer that represents all possible angular momenta values for transitions between the I_i and I_f states. Since a photon carries-out angular momentum $L = 1$, single γ-ray emission is forbidden for an $E0$ transition. However, the $E0$ transition can proceed via internal conversion [12]. Pure transitions are transitions that have no admixture of other multipolarities due to the selection rule. For example, a $2^+ \rightarrow 0^+$ transition is a pure $E2$ transition, while a $0^+ \rightarrow 0^+$ transition can only proceed via an $E0$ transition. In the following sections, these transitions are discussed in more details.

2.1.1 γ-ray emission

The multipolarity of a transition can be determined by measuring the polarisation and angular distribution of the γ rays. Therefore, γ rays can provide information on excited states of nucleus.

*internal pair production is neglected here

The transition rate between the initial and the final states can be described as

$$W(\sigma L) = \frac{1}{\tau} = \frac{2}{\epsilon_0 \hbar} \frac{L+1}{L\left[(2L+1)!!\right]^2} \left(\frac{E_\gamma}{\hbar c}\right)^{2L+1} B\left(\sigma L; I_i \rightarrow I_f\right), \tag{2.2}$$

where σ represents the type of transition, E_γ is the γ-ray energy, $\hbar$ is the reduced Planck constant, c is the speed of light and $B\left(\sigma L; I_i \rightarrow I_f\right)$ is the reduced transition probability of γ-ray transition [13]. The reduced transition probability can be written as [13]

$$B\left(\sigma\lambda; I_i \rightarrow I_f\right) = \frac{1}{2I_i+1} \left|\langle I_f|\hat{M}(\sigma L)|I_i\rangle\right|^2, \tag{2.3}$$

where $\langle I_f|\hat{M}(\sigma L)||I_i\rangle$is the reduced matrix element.

In even-even nuclei, transitions within rotational bands have a characteristic de-excitation mode as an electric quadrupole transition $E2$. For an electric quadrupole transition, the reduced transition probability can be calculated by

$$B(E2) = \frac{1}{1.223 \times 10^9 E_\gamma^5 \tau_\gamma} \frac{1}{5.940 \times 10^2 A^{4/3}} \text{W. u.}, \tag{2.4}$$

where τ_γ is a partial mean lifetime of the $E2$ multipolarity , γ-ray, transition in units of s, E_γ is energy of γ-ray in units of MeV and A is the mass number and results are given in Weisskopf units ($W.u.$) [13].

2.1.2 Internal conversion

Besides γ rays, the de-excitation process can also happen through an internal conversion. In internal conversion, the excited nucleus interacts electromagnetically with a bound electron in the atomic shell and ejects the electron from its atomic orbit. The kinetic energy E_e of the electron depends on the transition energy E_{tr} and the binding energy B_i of the atomic electron (atomic shells $i = K, L, M, N...$) as follows

$$E_e = E_{tr} - B_i, \tag{2.5}$$

The probability of internal conversion to occur relative to γ-ray emission is described by the conversion coefficient

$$\alpha = \frac{W_e}{W_\gamma}, \tag{2.6}$$

where W_e and W_γ are transition rates for conversion electrons and γ rays, respectively. The conversion coefficient depends on the proton number of the nucleus, the transition energy and multipolarity. Conversion coefficients can be defined in a similar manner for major atomic shells (α_K, α_L, α_M...) and subshells (α_{LI}, α_{LII}, α_{LIII}). The dependence of conversion coefficient on different multipolarity is shown in Figure 2.1 for Pb nuclei ($Z = 82$) as an example.

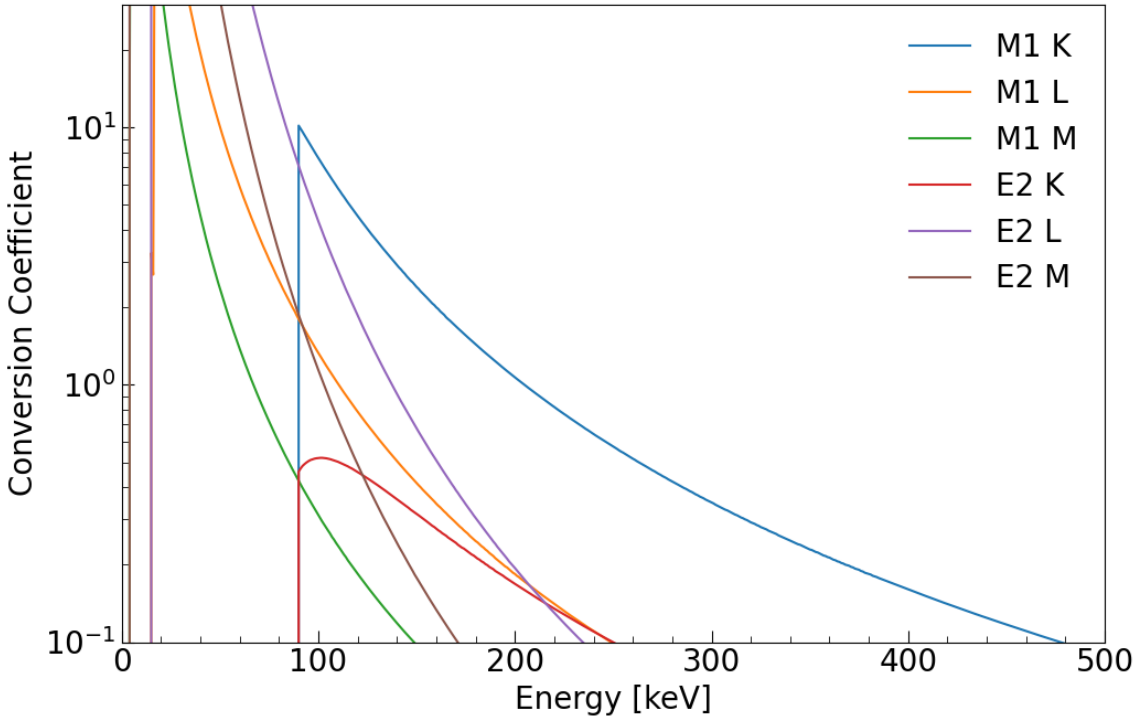

FIGURE 2.1 Internal conversion coefficients as a function of transition energy for $Z = 82$ [14].

The ratio of K- and L-electron intensities can be used to determine the transition multipolarity without information on conversion coefficient. The K/L ratio for three different multipolarities as a function of transition energy for Pb nuclei is shown in Figure 2.2.

In heavy nuclei, such as $Z \approx 82$, the internal conversion for an $E2$ transition is rather strong in the energy region below 250 keV as more than 20% of de-excitation proceeds via internal conversion. In comparison, the 70% of de-excitation proceeds via internal conversion for a 250 keV $M1$ transition which is much higher than for $E2$ transition.

2.1.3 $E0$ transition

The $E0$ transition can occur between states with $\Delta I = 0$. The $E0$ transitions a can be associated with changes in nuclear charge radii [15, 16] and can be employed as a tool for studying structural changes in nuclei. Often, the main interest is to study the transition monopole strength $\rho^2(E0)$. It can be defined as

$$\rho(E0) = \frac{\langle f|\hat{M}(E0)|i\rangle}{eR^2} = \frac{\langle f|\sum_j er_j^2|i\rangle}{eR^2}, \tag{2.7}$$

where R is the radius of nuclei, $\langle f|\hat{M}(E0)|i\rangle$ is the monopole matrix element, e is the elementary charge and r_j is the radial coordinate of the proton in the

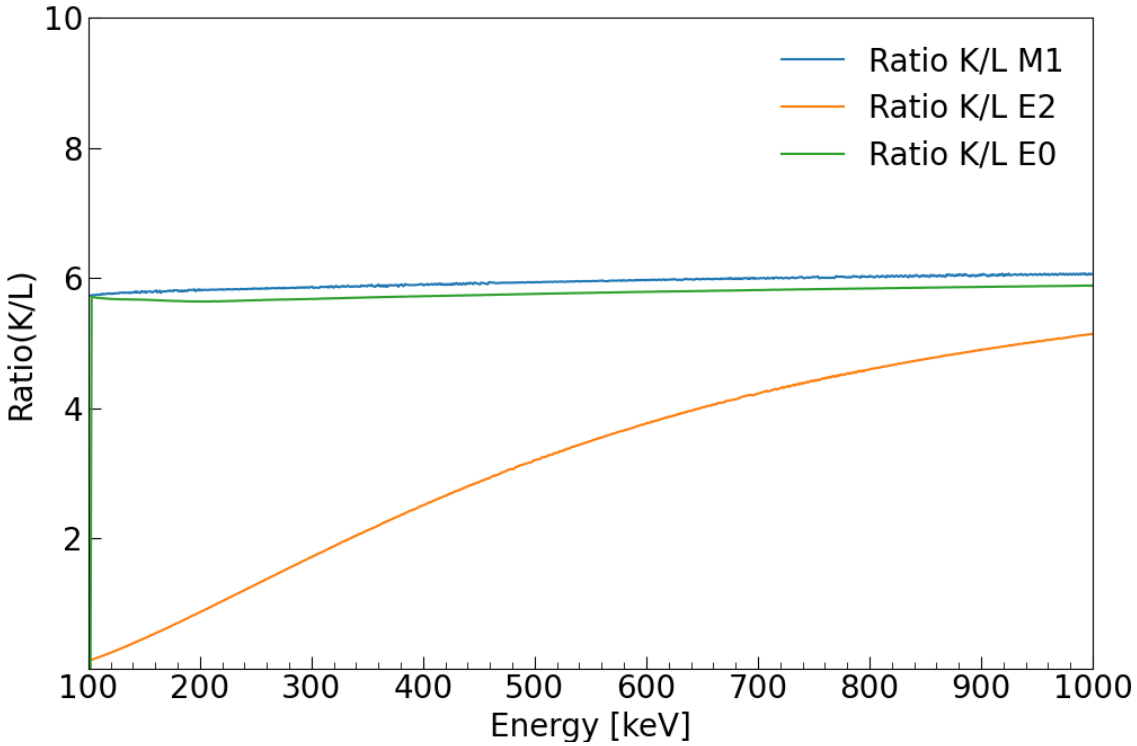

FIGURE 2.2 The ratio of emitted K and L conversion electrons for the $E0$, the $M1$ and $E2$ transitions in Pb nuclei as a function of transition energy. [14].

centre-of-mass frame.

The $E0$ transition rate can be expressed by the following equation

$$W(E0) = \frac{1}{\tau(E0)} = \Omega(Z,k)|\rho(E0)|^2, \tag{2.8}$$

where $\Omega(Z,k)$ is the electronic factor and $\rho(E0)$ is the monopole transition strength [17]. For nuclear transition energies $2m_e c^2$ or above, one needs to take into account the pair production in Equation 2.8, which is not case in this thesis.

The electronic factor Ω(Z,k) can be described as an atomic component of the transition rate. This factor does not depend on the nuclear spin but instead on the nuclear transition energy [17]. An electron has to be within the charge distribution of nucleus for the monopole interaction to occur, which is described by this factor [17]. The electronic factor is defined in [18] and the values of electronic factors are can be found tabulated in [14, 18, 19, 20], for example.

The monopole transition strength for an $E0$ transition from a state, which can also

de-excite via competing $E2$ transition, can be expressed as

$$\frac{W_K(E0)}{W_\gamma(E2)} = \frac{I_{K,E0}}{I_{E2,\gamma}} \tag{2.9}$$

$$\rho^2(E0) = \frac{I_{K,E0}}{I_{E2,\gamma}} \frac{1}{\Omega_K(Z, E_{E0})} W_\gamma(E2) \tag{2.10}$$

$$\rho^2(E0) = \frac{I_{K,E0}}{I_{E2,\gamma}} \frac{1}{\Omega_K(Z, E_{E0})} 1.223 \times 10^9 E_\gamma^5 B(E2), \tag{2.11}$$

where $I_{K,E0}$ is the intensity of K-electron of the $E0$ transition, Ω_K is the electronic factor, E_{E0} is the $E0$ transition energy, E_γ is the γ-ray energy of the $E2$ transition in units of MeV and $B(E2)$ is in units of $e^2\text{fm}^4$ [13].

For interband transitions between states with the same spin and parity $I^+ \rightarrow I^+$, the relation between the K-conversion electron intensity of the $E0$ transition and measured K-electron intensity, assuming $E0$, $M1$ and $E2$ being possible multipolarities, can be determined with equation

$$I_{K,E0} = I_K(exp) - \alpha_K(E2+M1) I_\gamma = I_K(exp) - \frac{\delta^2 \alpha_K(E2) + \alpha_K(M1)}{1+\delta^2} I_\gamma, \tag{2.12}$$

where $I_K(exp)$ is the experimental K-electron intensity, $\alpha_K(E2+M1)$ is the K-conversion electron coefficient for the mixed $E2/M1$, I_γ is the γ-ray intensity, δ^2 is the multipole mixing ratio between $E2$ and $M1$, $\alpha_K(E2)$ and $\alpha_K(M1)$ are the K-conversion electron coefficient for $E2$ and $M1$ multipolarities, respectively.

2.1.4 Total conversion coefficients for the $I^+ \rightarrow I^+$ interband transitions

For the $I^+ \rightarrow I^+$ transition with experimental K-conversion coefficient $\alpha_K(exp)$ being larger than the any possible $\alpha_K(M1+E2)$ value, it is possible to derive the equation for a total conversion coefficient $\alpha_{tot}(exp)$

$$\alpha_{tot}(exp) = \alpha_K(exp) \frac{\alpha_{tot}(calc)}{\alpha_K(calc)}, \tag{2.13}$$

where $\alpha_{tot}(calc)$ is the calculated total conversion coefficient for the $M1$ and $E2$ transitions and taking account electrons from $E0$ transition. The $\alpha_K(calc)$ is the calculated K-electron conversion coefficient. The $\alpha_{tot}(calc)$ can be written as

$$\begin{aligned} \alpha_{tot}(calc) &= \frac{I_{tot,e}(E2) + I_{tot,e}(M1) + I_{tot,e}(E0)}{I_\gamma} \\ &= \frac{\alpha_{tot}(M1+E2) + \frac{\Omega_{tot}}{\Omega_K} I_{K,e}(E0)}{I_\gamma} \\ &= \frac{\delta^2 \alpha_{tot}(E2) + \alpha_{tot}(M1)}{1+\delta^2} + \frac{\Omega_{tot}}{\Omega_K} \frac{I_{K,e}(E0)}{I_\gamma}, \end{aligned} \tag{2.14}$$

where $I_{K,e}$ is the K-electron intensity, $I_{tot,e}$ is intensity of all conversion electrons, I_γ is the intensity of γ rays, δ^2 is the $E2/M1$ multipole mixing ratio, Ω_{tot} and Ω_K are the total and K electronic factors of the $E0$ transition. Similarly, $\alpha_K(calc)$ can be written as

$$\alpha_K(calc) = \frac{\delta^2\alpha_K(E2) + \alpha_K(M1)}{1+\delta^2} + \frac{I_{K,e}(E0)}{I_\gamma}. \tag{2.15}$$

If there is an excess counts of conversion electrons associated with the transition, they may indicate an $E0$ transition. With respect to γ-ray intensity, value for $\frac{I_{K,e}(E0)}{I_\gamma}$ can be deduced using the experimental conversion coefficient $\alpha_K(exp)$

$$\frac{I_{K,e}(E0)}{I_\gamma} = \alpha_K(exp) - \frac{\delta^2\alpha_K(E2) + \alpha_K(M1)}{1+\delta^2}. \tag{2.16}$$

By combining results from Equations 2.14, 2.15 and 2.16 with Equation 2.13, the value for the total conversion coefficient $\alpha_{tot}(exp)$ can be obtained as follows

$$\begin{aligned}\alpha_{tot}(exp) &= \alpha_K(exp)\frac{\alpha_{tot}(calc)}{\alpha_K(calc)} \\ &= \alpha_K(exp)\frac{\frac{\delta^2\alpha_{tot}(E2)+\alpha_{tot}(M1)}{1+\delta^2} + \frac{\Omega_{tot}}{\Omega_K}\left(\alpha_K(exp) - \frac{\delta^2\alpha_K(E2)+\alpha_K(M1)}{1+\delta^2}\right)}{\frac{\delta^2\alpha_K(E2)+\alpha_K(M1)}{1+\delta^2} + \alpha_K(exp) - \frac{\delta^2\alpha_K(E2)+\alpha_K(M1)}{1+\delta^2}}\end{aligned}$$

and finally it can be derived

$$\alpha_{tot}(exp) = \frac{\delta^2\alpha_{tot}(E2)+\alpha_{tot}(M1)}{1+\delta^2} + \frac{\Omega_{tot}}{\Omega_K}\left(\alpha_K(exp) - \frac{\delta^2\alpha_K(E2)+\alpha_K(M1)}{1+\delta^2}\right). \tag{2.17}$$

The Equation 2.17 is used to evaluate the total conversion coefficient for the interband transitions in ^{186}Pb as discussed in Section 4.9.2.

2.2 Collective behaviour of deformed nuclei

While the Mayer's nuclear shell model has successfully predicted some of the ordering principles governing nuclei [1], it fails to reproduce (like many the other nuclear models to date) many of the observed phenomena. For example, rotation and vibration of nuclei could be understood by collective models [2, 21]. In the ^{186}Pb nucleus, three different shapes (spherical, prolate and oblate), have been proposed, see Figure 2.3.

A deformed nucleus cannot be described using the spherical shell model. The

surface of the deformed nucleus can be described using radius vector [12]

$$R(\theta,\phi) = R_0\left(1+\sum_{\lambda\mu}\alpha_{\lambda\mu}Y_{\lambda\mu}(\theta,\phi)\right), \tag{2.18}$$

where R_0 is the radius of the spherical nucleus of the same volume, $\alpha_{\lambda\mu}$ is a multipole parameter, $Y_{\lambda\mu}(\theta,\phi)$ is spherical harmonic function, λ is the multipolarity and $\mu = (-\lambda...\lambda)$. Assuming axially symmetric deformation leads to $\mu = 0$ (note that for $\alpha_{\lambda 0}$ notation β_λ is commonly used) [12]. The quadrupole deformation ($\lambda = 2$) is often of interest in nuclear physics. In those cases, equation (2.18) can be expressed as

$$R(\theta,\phi) = R_0\left(1+\beta_2 Y_{20}(\theta,\phi)\right), \tag{2.19}$$

where β_2 is known as the deformation parameter. The deformation parameter β_2 gives information about the eccentricity of the ellipse shape nucleus and can be written as

$$\beta_2 = \frac{4}{3}\sqrt{\frac{\pi}{5}}\frac{\Delta R}{R_0}, \tag{2.20}$$

where ΔR is the difference between semimajor and semiminor axis lengths [22]. The corresponding shapes for different β_2 values are shown in Figure 2.3.

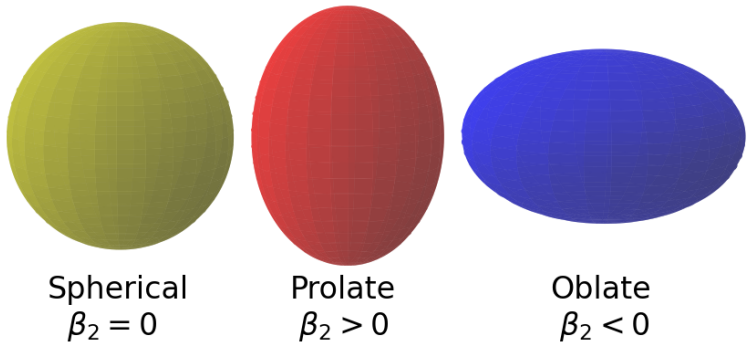

FIGURE 2.3 Common shapes of nuclei; spherical (yellow), prolate (red) and oblate (Blue). The corresponding β_2 deformation parameter values for each shape are also given.

The deformation parameter β_2 can be acquired by measuring quadrupole moments. The transitional quadrupole moments can be obtained through lifetime measurements [23] and spectroscopic quadrupole moments of a state can be acquired via Coulomb excitation (Coulex) experiments [24].

2.2.1 Rotating nucleus

The evidence for collectivity, related to deformations, was obtained in the electric quadrupole moment analysis by Goldhaber and Sunyar [25] and later Bohr and Mottelson [26]. The quadrupole transition rates were higher than the single-particle model predictions and as a result the collective model was suggested.

The rotational energy spectrum for a coupled particle motion and axially symmetric deformed core, in the region of multiple particles outside of a closed shell, can be described as

$$E_I = \frac{h^2}{2\mathcal{I}} I(I+1), I = 0, 2, 4, ... \tag{2.21}$$

where E_I is the level energy with angular momentum I and $\mathcal{I}$ is the moment of inertia, which is proportional to the square of the deformation parameter [26, 27].

Even more detailed models to describe the collective rotation of the nucleus have been developed. Rotation can be described by variable moments of inertia [28] and Harris formalism [29], for example. These models can also be used to extrapolate the level energies for unperturbed states of interest. In this study, variable moments of inertia were used and are further discussed in the Section 2.3.

Multiple shape coexistence is a common feature in the neutron-deficient Pb region. Different shapes are associated with different configurations and configuration mixing is typical for these nuclei. Configuration mixing affect the level energies, thus the Equation 2.21 may not have a good predictive power.

2.2.2 Transition probabilities for deformed nuclei

The $B(E2)$ values can be used to infer the information of structural changes between the initial and final states. The reduced $E2$ transition probability within deformed (axially symmetric nucleus) band can be described by the following formula [2]

$$B(E2; KI_i \rightarrow KI_f) = \frac{5}{16\pi} e^2 Q_t^2 \left\langle I_f K 20 \middle| I_i K \right\rangle, \tag{2.22}$$

where Q_t is the transitional quadrupole moment, I_i (I_f) is the spin of the initial (final) state, $\left\langle I_f K 20 \middle| I_i K \right\rangle$ is the Clebsh-Gordan coefficient of a transition within the collective band with $\Delta I = 0$ and $\Delta K = 0$. For a pure rotor, the transitional quadrupole moment Q_t can be considered as an intrinsic quadrupole moment Q_0. The intrinsic quadrupole moment is then defined as

$$Q_0 = \sqrt{\frac{16\pi}{5}} \left\langle IK \middle| \hat{M}(E2) \middle| IK \right\rangle, \tag{2.23}$$

where $\left\langle IK \middle| \hat{M}(E2) \middle| IK \right\rangle$ is the corresponding transition matrix element.

The deformation parameter β_2 is connected to the intrinsic quadrupole moment, with the assumption of uniform charge distribution, as follows

$$Q_0 = \sqrt{\frac{16\pi}{5}}\frac{3}{4\pi}ZR^2\beta_2(1+0.16\beta_2)e, \tag{2.24}$$

where Z is the atomic number, A is the mass number, e is the electric charge, $R_0 \approx 1.2\,\text{fm}$ and $R = R_0A^{1/3}$ is the radius of the nucleus [12].

2.2.3 Shape coexistence and configuration mixing

Shape coexistence is a phenomenon in which the same nucleus can have different shapes. In the neutron-deficient Pb region, shape coexistence appears at low energies. The $E0$ transitions are considered to be spectroscopic fingerprints of shape coexistence [15].

Shape coexistence usually involves configuration mixing between different structures, as is the case with nuclei with $Z \sim 82$ near the $N = 104$ mid-shell. To evaluate this admixture of two different shapes, the monopole transition strength $\rho^2(E0)$ can be used. Two states that mix can be described by

$$|I_i\rangle = a\,|J_i\rangle + b\,|J_f\rangle \tag{2.25}$$

$$|I_f\rangle = -b\,|J_i\rangle + a\,|J_f\rangle\,, \tag{2.26}$$

where a and b are mixing amplitudes, subscript i (f) stands for initial (final), I is the perturbed state with the angular momentum $I = I_i = I_f$ and similarly for the unperturbed state J. The normalisation of mixing amplitudes is declared as follows

$$a^2 + b^2 = 1. \tag{2.27}$$

For a harmonic quadrupole vibrator, the monopole operator $\hat{M}(E0)$ can be written as [15]

$$\langle J_{i,f}|\hat{M}(E0)|J_{i,f}\rangle = \frac{3}{5}ZeR^2(\frac{5}{4\pi}\,\langle J_{i,f}|\sum_\mu \alpha_\mu|^2|J_{i,f}\rangle), \tag{2.28}$$

where R is the radius of nucleus, α_μ is the multipole parameter and $\mu = \pm2, \pm1, 0$. The multipole parameter can be written as

$$\langle J_{i,f}|\sum_\mu \alpha_\mu|^2|J_{i,f}\rangle = \beta_2^2. \tag{2.29}$$

For monopole operator it is possible to define

$$\begin{aligned}\langle I_f|\hat{M}(E0)|I_i\rangle = &\left(\frac{3}{5}ZeR^2\left(\frac{5}{4\pi}ab\,\langle J_i|\sum_\mu \alpha_\mu|^2 J_i\rangle - \langle J_f|\sum_\mu \alpha_\mu|^2|J_f\rangle\right)\right)\\ &- ab\,\langle J_f|\hat{M}(E0)|J_i\rangle\,,\end{aligned} \tag{2.30}$$

where $\langle J_f|\hat{M}(E0)|J_i\rangle \approx 0$ [†]. Using the definition of monopole strength, see Equation 2.7, Equation 2.30 can be written as

$$\rho^2(E0) = \left(\frac{3}{4\pi}Z\right)^2 a^2b^2\left(\beta_{2,i}^2 - \beta_{2,f}^2\right)^2. \tag{2.31}$$

The derivation of Equation 2.31 is shown in more details by Wood *et al.* in reference [15] and references therein. The connection between $E0$ transition and mean-square radii of coexisting structures was realised by Jan Blomqvist [31]. By taking into account the normalisation of mixing amplitudes, the following formula can be derived

$$\rho^2(E0) = \left(\frac{3}{4\pi}Z\right)^2 a^2(1-a^2)\left(\beta_{2,i}^2 - \beta_{2,f}^2\right)^2. \tag{2.32}$$

Equation 2.32 was used in this study to estimate the admixture of two different configurations. It is however important to remember that this model is only valid for two-level mixing. In ^{186}Pb, the prolate and oblate configurations are considered to mix, whereas excited states associated with spherical shape have not been observed.

The two-level mixing can also be assessed, for example, using the $B(E2)$ values. The reduced transition probability for transitions involving configuration mixing can be written as

$$B(E2; I_i \rightarrow\ I_f) = \left[\sum_{j,k} a_j^i b_k^f \langle j|\ E2\ |k\rangle\right]^2, \tag{2.33}$$

where j, k indicate pure states and a and b are the corresponding mixing amplitudes [30]. In a simple two-state mixing model, if the initial state is assumed to be unperturbed and the interband transitions between pure states are ruled, for axially symmetric rotating nucleus the final state can be expressed as a mixture of two different configurations as follows

$$|I_f\rangle = a\,|J_{f,1}\rangle + b\,|J_{f,2}\rangle\,, \tag{2.34}$$

where I_f is the perturbed state and $J_{f,(1,2)}$ represents unperturbed states. Using Equation 2.33, with a perturbed final state, gives

$$B(E2; J_{i,1} \rightarrow\ I_f) = \left[a\,\langle J_{f,1}|\ E2\,|J_{i,1}\rangle + b\,\langle J_{f,2}|\ E2\,|J_{i,1}\rangle\right]^2, \tag{2.35}$$

where $\langle J_{f,2}|\ E2\,|J_{i,1}\rangle = 0$. For the deformed nucleus, Equation 2.35 can be written as

$$B(E2; J_i \rightarrow\ I_f) = \left(a\sqrt{\frac{5}{16\pi}}Q_0^{def}\ \langle I_f K20|\ J_i K\rangle\right)^2 \tag{2.36}$$

The Equation 2.36 can be used to estimate the mixing amplitude a, if $B(E2; J_i \rightarrow\ I_f)$ and Q_0 are known [30].

[†]There has been discussion about the validity of this approximation, see the reference [30]

2.3 Searching bandheads through VMI-calculation

The Variable Moment of Inertia (VMI) [28] model can be used to estimate for the energy of the unperturbed states. The VMI model is a semi-classical model used to interpret rotational bands. The original VMI model was developed for yrast bands, but can also be applied, for example, for non-yrast band in ^{186}Pb. In addition to the rotational term, the VMI model also includes a potential term which depends on the difference between the moments of inertia of intial $\mathcal{I}_I$ and final $\mathcal{I}_\mathcal{F}$ states.

The yrast and non-yrast band level energies of ^{186}Pb were determined by using following formula in VMI calculations

$$E_I = \left(\frac{I(I+1)}{2\mathcal{I}_I}\right)\left(1+\left(\frac{I(I+1)}{4C\mathcal{I}_I^3}\right)\right) + E_x, \tag{2.37}$$

where E_I is the level energy with angular momentum of I, C is the "restoring force constant" [28] and E_x is the band-head energy. The parameter $\mathcal{I}_I$ can be determined from a cubic equation depending on the parameters $\mathcal{I}_0$ and C

$$\mathcal{I}_I^3 - \mathcal{I}_0\mathcal{I}_I^2 - \left(\frac{I(I+1)}{2C}\right) = 0, \tag{2.38}$$

which has one real root for any positive value of $\mathcal{I}_0$ and C parameters. The parameters $\mathcal{I}_0$, C and E_x were left as parameters which were solved using the non-linear *curve_fit*-method of the Scipy [32] Python library.

The values for $\mathcal{I}_0$, C and E_x were restricted to be positive and the band-head energy E_x lower in energy than the energy of the 2^+ state of the band. The code successfully reproduced the results obtained by Mariscotti [28].

3 EXPERIMENTAL METHODS

The experimental work of this thesis was carried out in the Accelerator Laboratory of the University of Jyväskylä (ACC-LAB) using the SAGE spectrometer [33] in conjunction with the RITU separator [34]. The beam from the K130 cyclotron [35] was transported to the target chamber of the SAGE spectrometer. The beam was focused on the target foil, in which the beam particles fused with the target nuclei. The process is called a fusion-evaporation reaction, which is regularly used to study structure of atomic nuclei in the ACC-LAB.

The fusion-evaporation residues, hereafter called recoils, were transported through the recoil separator to the focal plane. The recoils were identified using the Recoil-Decay-Tagging method (RDT) [36, 37] and the emitted γ-rays and conversion electrons were detected with SAGE at the target position. These detected events were recorded by the Total-Data-Readout (TDR) [38] data acquisition system (DAQ).

In this chapter, the instrumentation and methods used in the S12 experiment are explained in more details.

3.1 Prompt spectroscopy with the SAGE spectrometer

The SAGE spectrometer combines in-beam γ-ray and conversion electron spectroscopy. The main parts of SAGE were the target chamber surrounded by a germanium detector array, three solenoid magnets (main, upstream and downstream coils), high-voltage (HV) barrier and the SAGE silicon detector inside of the detector chamber. The SAGE spectrometer is shown in Figure 3.1.

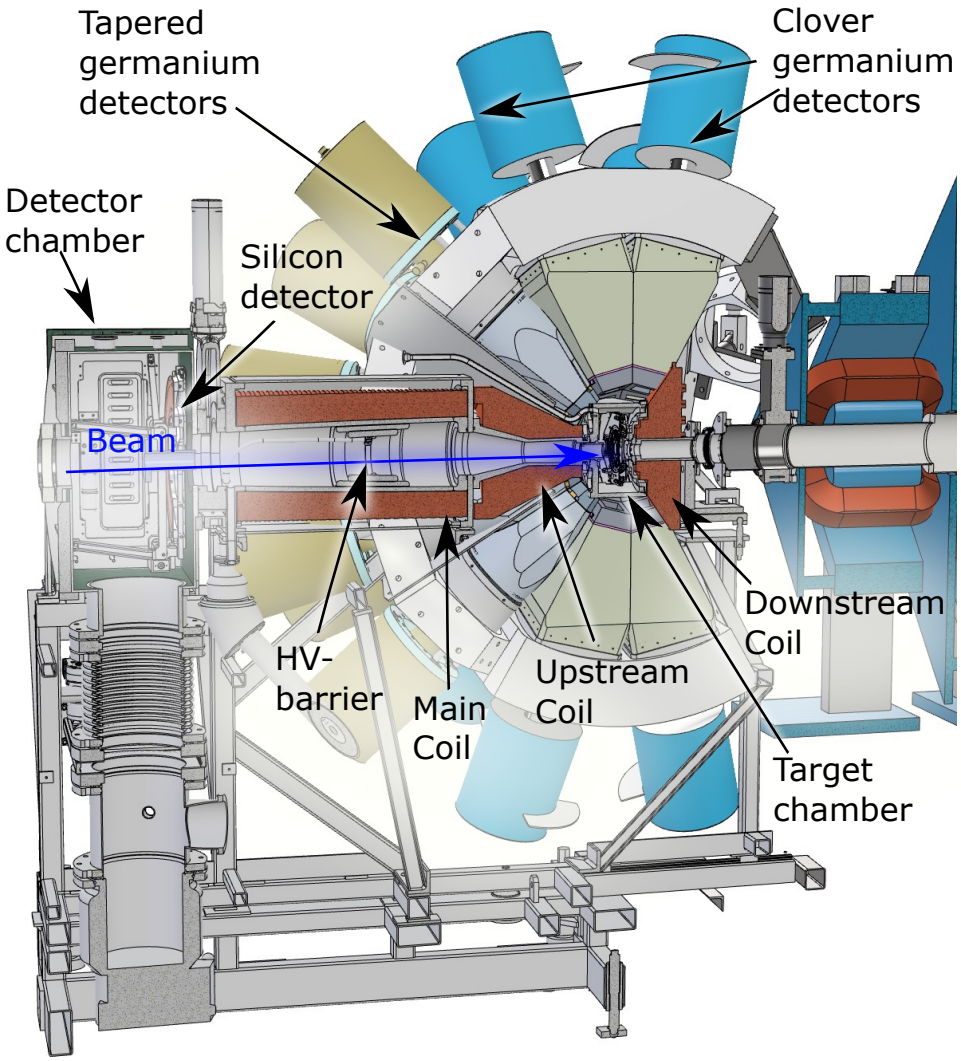

FIGURE 3.1 The SAGE spectrometer consists of a germanium array for γ-ray detection and a silicon detector which is located upstream from the target for detection of conversion electrons. Main coil and upstream coils were installed between the target and the silicon detector in order to transport conversion electrons to the silicon detector. Inside the main coil, a HV-barrier to reduce δ-electron flux into the detector is installed. The schematic drawing was provided by J. Tuunanen.

The prompt γ-rays were detected with the germanium detector array consisting of 10 tapered germanium detectors (Phase1 [39] or GASP [40]) at the angle of 133.6° with respect to the beam axis and 24 Clover detectors set up in two different rings at the angle of 104.5° and 75.5°, each consisting of 12 detectors. The germanium array is essentially the same as the JUROGAMII array without the ring of five tapered detectors at the angle of 157.6° [33]. The BGO shields next to the solenoid magnets were protected with iron shields against the magnetic field introduced by the solenoid magnets.

Conversion electrons were transported from the target chamber to the detector chamber by means of solenoid coils. The main solenoid is set in downstream with respect to the silicon detector chamber, while the second solenoid is located between the main coil and target chamber and the third solenoid is downstream with respect of the target chamber. The solenoids were typically operated at 800 A. Consequently, water cooling has been introduced. The coils were electrically insulated with epoxy.

The silicon detector is used to detect conversion electrons and is located upstream relative to the target. The silicon detector is 1 mm thick and has been segmented to 90 pixels. The centre of the detector has two semicircular pixels. Around the centre pixels, there were seven, 1 mm wide, inner rings each divided into eight sectors. Around these seven rings, there were eight, 2 mm wide, outer rings divided into four sectors. The designed segmentation aims to equalise the count rate distribution across the detector. The diameter of detector, including the guard rings and contact pads, is 53 mm.

The HV barrier is located inside the main solenoid coil. It is essential for lowering the flux of low-energy δ electrons into the silicon detector. The large flux of the δ-electrons can cause electron summing in electron energy spectrum. The usual operational voltage for the HV barrier is -30 kV.

3.2 Selecting nuclei of interest with the RITU separator

The gas-filled recoil separator RITU [34] was used to separate recoils from the primary beam. RITU is situated downstream of the target with an ion-optical configuration of QDQQ, where Q corresponds to a quadrupole and D to a dipole magnet. As the reaction products and beam come out of the target chamber, the first quadruple focuses the recoils vertically to match better with the dipole magnet acceptance. The dipole magnet then bends the recoils and beam according to their magnetic rigidity to achieve separation. The separated recoils were guided towards the focal plane and beam particles to the beam dump. The recoils were focused horizontally and vertically with the last two quadruples to the focal plane implantation detector.

RITU is operated in helium dilute gas. The recoils will obtain an average charge state as they interact with helium atoms. RITU is tuned to this charge state, which allowed smaller recoil image size in the GREAT spectrometer than obtained without tuning. These actions improved the transmission through the RITU separator.

3.3 Identifying the nuclei of interest with the GREAT spectrometer

The GREAT spectrometer [41] was located at the focal plane of RITU. GREAT consisted of a multi-wire proportional counter (MWPC), two double-sided silicon detectors (DSSDs), the PIN diode array, a planar double-sided germanium strip detector, two Clover type germanium detectors and one large-volume GREAT clover detector. The recoils flew through the MWPC before being implanted in the DSSDs which have 4800 pixels in total. The recoils and their subsequent α-decays were detected with the DSSDs. The DSSDs were surrounded by two Clover type germanium detectors and GREAT Clover detector to detect γ-rays emitted from recoils in DSSDs. After the DSSDs, the planar double-sided germanium strip detector is installed to detect low-energy γ rays and conversion electrons. The schematic drawing of GREAT is shown in Figure 3.2.

The recoil implantation depth on the DSSDs is shallow, thus the α particles from recoils could escape from the DSSDs. The array of 28 silicon PIN diodes were installed upstream of the DSSDs in box arrangement to detect the escaped α particles with geometrical efficiency of $\sim$30 % [41]. In this work, PIN-diodes were used to recover some of the statistics that was lost due to escaped α particles not depositing full energy in the DSSDs. Consequently, this also allowed for increasing the statistics of α-tagged prompt γ rays and conversion electrons detected with SAGE.

3.4 Recording data with the total-data readout data acquisition system

In the present work, the Total-Data Readout (TDR) [38] data acquisition system was employed. In TDR, data were recorded from each channel independently with a timestamp from 100 MHz clock (*i.e.* one tick every 10 ns). The benefit of using triggerless data acquisition is that the dead-time is virtually zero compared to data-acquisition system with a common hardware trigger. Instead of hardware/software trigger, the filter were used in order to reduce the amount of saved data.

The data acquisition system was divided into two sections, the digital part, which contains germanium detectors, the SAGE silicon detector and the PIN diodes channels, and the analogue part, which contains MWPC and DSSD strip channels. Signals from the digital part were first processed with the gain and offset cards (GO cards) to set signal amplitude and offset to match with the input range of the 14-bit 16-channel Lyrtech VHS-ADC digitiser cards in the region of interest. The signal amplitudes of in-beam detectors were determined using Moving Window

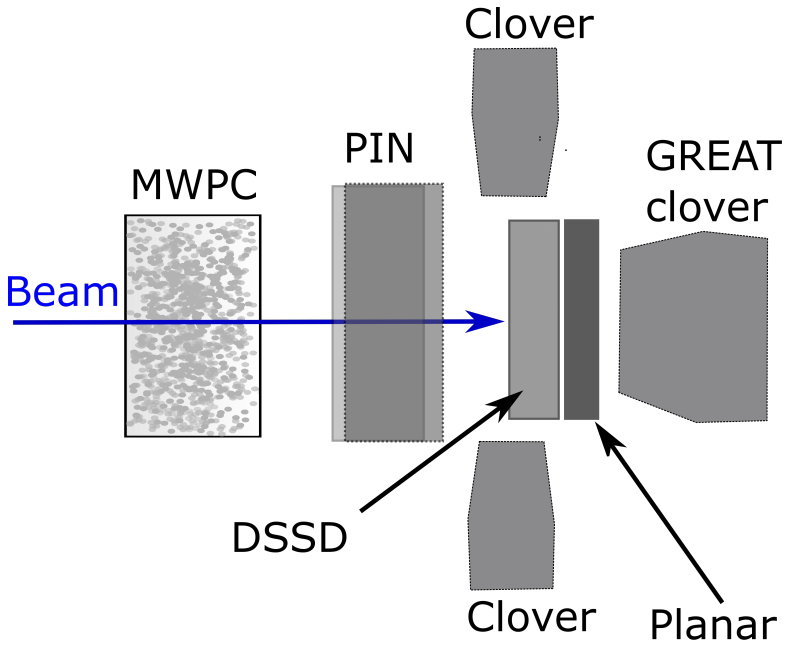

FIGURE 3.2 The schematic drawing of the GREAT spectrometer. The MWPC-detector is used to detect particles flying through it, the PIN diodes to detect decay particles emitted from recoils implanted into DSSDs and the DSSD detects both recoils and decay events. DSSD is surrounded by two clover type germanium detectors and the GREAT clover for detection of γ rays emitted from the implanted nuclei. The planar type germanium detector is installed downstream relative to DSSD to detect conversion electrons and γ rays.

Deconvolution (MWD) [42] algorithm in the FPGA of the VHS-ADC. In the analogue part, there were two signal types coming from the detectors, one for timing and the other for energy signals and both were fed in to VXI-ADC cards. The data from the ADC cards were then sent to a collator. Both sides, in-beam and focal plane, had a common clock signal produced by the metronome unit which was fed to the Lyrtech VHS-ADC and the VXI-ADC cards. With a common clock, it was possible to timestamp every event with the aforementioned 10 ns time accuracy.

Data from the VHS-ADC cards and ADC cards of analogue part were combined with a computer-based Merge program that first collected the data, time filter it and then sent it to an Event Builder program. The Event Builder filtered the data with a condition the user has chosen, for example in RDT method, the software trigger was set to a logical signal DSSD-OR which opened a user-defined time window in which data were saved and the rest were removed. The data could be read and sorted then using the GRAIN-software package [43].

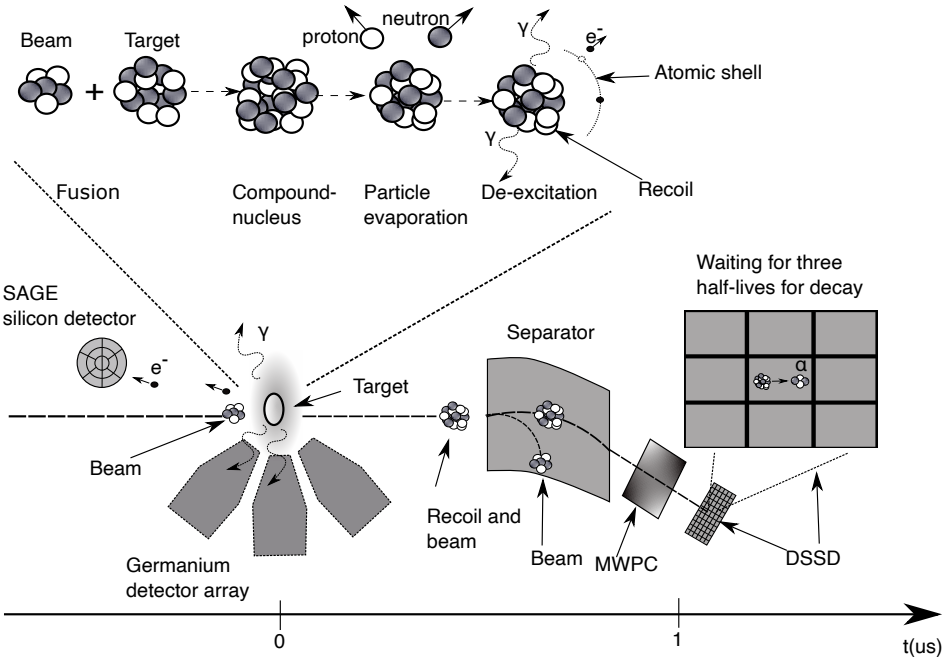

FIGURE 3.3 Schematic drawing of RDT method used to assign prompt γ rays and conversion electrons with nucleus of interest.

3.5 Assigning prompt events with the nuclei of interest employing the recoil-decay tagging technique

In the RDT method, recoils at the DSSDs were identified by their decay, in other words, the recoils were tagged with their corresponding decay properties. The identified recoil event can also be correlated with the prompt γ rays or conversion electrons. This method decreases substantially background and the amount of contaminants in the in-beam γ-ray and conversion electron energy spectrum. The RDT method is schematically shown in Figure 3.3.

In the analysis process, recoil and decay events were dissociated in the DSSDs by requiring a concurrent MWPC signal with the DSSDs event for recoils. Recoils could be distinguished from the scattered beam by setting a DSSD energy, time-of-flight, and MWPC energy conditions. All these recoil events are tagged. It was possible to use α decay as a tag to identify recoils of interest. In the following analysis, after the α decay has happened, the algorithm assumes that the previous recoil event implanted in the same pixel was the nucleus decaying in the DSSD pixel. False correlation may occur if the recoil implantation rate was larger than the pixelation and half-life of the nucleus of interest allows.

4 COMBINED ELECTRON AND γ-RAY SPECTROSCOPY OF ^{186}PB

Shape coexistence in the neutron mid-shell nucleus ^{186}Pb has been a vibrant topic for several decades. Nuclei with $Z \approx 82$ near mid-shell $N = 104$ has shown a strong manifesto of shape coexistence [7]. Several theoretical calculations [44, 45] predict mixing between 2p-2h and 4p-4h collective bands of ^{186}Pb, making this nucleus a prime candidate to investigate the shape coexistence phenomenon.

Evidence for different shapes in ^{186}Pb have been obtained in several studies. In in-beam γ-ray spectroscopic experiments, the rotational bands based on different shapes associated with different configurations have been observed in previous studies [10, 46, 47, 48]. With the Recoil Distance Doppler-Shift (RDDS) method, lifetimes up to the yrast 8^+ states were experimentally determined by Grahn *et al*. [49], which showed that the yrast band states possess only little admixtures from different configurations. The α-decay fine structure experiment of ^{190}Po, performed by Andreyev *et al*. [8], discovered an unique triplet of 0^+ states in ^{186}Pb that they associated with spherical, prolate and oblate shapes.

Even though γ-ray spectroscopic experiments provide information on excited nuclei, the $E0$ transitions remain undetected as they proceed via internal conversion or pair production. These type of de-excitations are typically present in the $I \rightarrow I$ interband transitions between $K = 0$ rotational bands. Combined conversion electron and γ-ray spectroscopic measurement provide means to study these converted transitions. Our in-beam experiment provided the first direct observation of the $0^+ \rightarrow 0^+$ transition energies, which were observed in the aforementioned α-decay fine structure experiment [8], and allowed for obtaining the $E0$ interband $I \rightarrow I$ transitions.

4.1 Experimental methods

Simultaneous conversion electron and γ-ray measurement of ^{186}Pb have been conducted using the SAGE+RITU+GREAT+TDR [33, 41, 34, 38] instrumentation. The experiment was performed in 2013 at the ACC-LAB and carries an experiment code of S12 [50].

The RDT method was employed for the ^{106}Pd(^{83}Kr,3n)^{186}Pb reaction with the beam energy 365 MeV. The thickness of ^{106}Pd target was 1 mg/cm^2 and the effective beam-on-target time was 4.5 days. The experiment was performed with the beam intensity varying between 4 pnA to 5 pnA. Recoils were transported through the RITU separator with transmission of $\approx$ 60% [51] and then implanted in to the DSSDs. The RDT method was used to identify ^{186}Pb recoils. During the experiment, 634000 ^{186}Pb α particles were collected in the DSSDs. All uncertainties given at 1 σ level in this thesis.

4.2 Energy and efficiency calibration

The SAGE germanium detector array energy and relative efficiency calibration was performed using ^{152}Eu and ^{133}Ba sources. The absolute efficiency was taken as 3.6% at 1332 keV for the SAGE germanium detector array [33]. The energy and relative efficiency calibration for the SAGE silicon detector was determined employing open ^{133}Ba and ^{207}Bi electron sources. The K-conversion electron and γ-ray intensity of transition $\frac{1}{2}^+ \rightarrow \frac{5}{2}^+$ with transition energy of 356 keV following the decay of ^{133}Ba were used to normalise the electron and γ-ray detection efficiencies. The γ-ray and conversion electron intensities for transitions in calibration source nuclei were taken from reference [52].

The efficiency curves of silicon and germanium detector arrays are plotted in Figure 4.1. The fitted function for γ-ray efficiency is the same as introduced in the RadWare software package [53]

$$\epsilon(E_\gamma) \times 1000 = e^{\left((A+BX)^{-G}+(D+EY+FY^2)^{-G}\right)^{(-1/G)}}, \tag{4.1}$$

where E_γ is energy in units of keV, $\epsilon(E_\gamma)$ is the absolute efficiency at the energy E_γ $X = log(E_\gamma/100)$ and $Y = log(E_\gamma/1000)$. A, B, D, E, F are the free fit parameters while $G = 35$ was fixed. The values for parameters are shown in Table 4.1 .

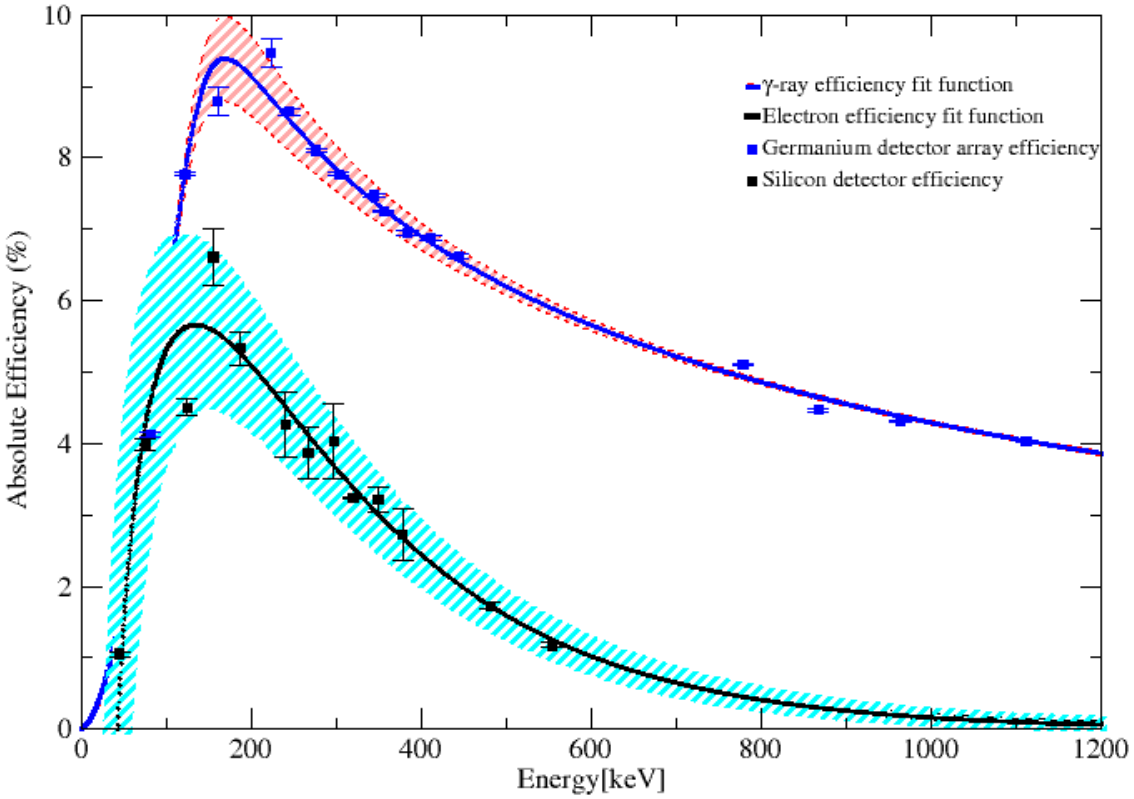

FIGURE 4.1 Measured efficiency of the SAGE germanium detector array and the silicon detector for S12. The γ-ray efficiency fit function is shown in blue and its error is marked with red band. The electron efficiency fit function is shown in black and its error is marked in cyan band.

TABLE 4.1 Values of parameters and corresponding uncertainties obtained for the γ-ray detection efficiency as declared in Equation 4.1

Parameter	Value	Uncertainty
A	8.669	0.025
B	1.709	0.122
D	8.354	0.008
E	-0.563	0.024
F	-0.050	0.022
G	35	0

The efficiency for electrons were determined using equation

$$\epsilon(E_e) = A(1 - \sqrt{B/E_e})e^{-CE_e}, \tag{4.2}$$

where, E_e is the kinetic energy of electron in units of keV, A, B and C are free parameters for the fit. The formula was introduced by Konki [54] and it is based on the equation formed by Butler *et al.* [55]. The parameter values obtained from fit are listed in Table 4.2.

TABLE 4.2 Values of parameters and corresponding uncertainties and covariance obtained for the electron detection efficiency declared in Equation 4.2

Parameter	Value	Error
A	24.731	2.861
B	42.770	4.634
C	-0.005	0.001
$\mathrm{Cov_{AB}}$	9.827	
$\mathrm{Cov_{AC}}$	-0.001	
$\mathrm{Cov_{BC}}$	-0.001	

Since γ rays and electrons following the de-excitation of the nucleus of interest are emitted in-flight, kinematic correction is needed. For γ rays, this can be done using the equation for Doppler correction as follows

$$E_\gamma = E_0(1 + \frac{v}{c}cos(\theta)) = E_0(1 + \beta cos(\theta)), \tag{4.3}$$

where E_γ is the Doppler corrected energy of the emitted γ ray, E_0 is the measured γ-ray energy, v is recoil velocity, c is the speed of light, θ is the emission angle of the γ-ray with with respect to the beam axis. The germanium detector angles are listed in section 3.1. Similarly, kinematic energy correction for the conversion electrons emitted from the moving nucleus is defined as

$$E_e = \frac{E_0 + m_e - \beta cos(\theta)\sqrt{E_0^2 + 2m_e E_0}}{\sqrt{1-\beta^2}} - m_e, \tag{4.4}$$

where E_e is kinematically corrected electron energy and m_e is the electron mass. The average electron emission angle θ was estimated to be 160°. The β-parameter value of 0.0378 for ^{186}Pb was determined experimentally using the γ rays of the $2_1^+ \rightarrow 0_1^+$ transition in ^{186}Pb. The same β-parameter value was used for conversion electrons.

The uncertainty of measurement can be divided in two categories: random and systematic errors. The random errors depend on statistics and errors related to fits. The systematic errors of γ-ray energies were evaluated comparing the measured γ-ray energies obtained from recoil-gated γ-ray energy spectrum to the literature values from Nuclear Data Sheets [56, 57, 58]. Using $\gamma\gamma$-coincidences for transitions in ^{187}Tl, ^{186}Tl, ^{186}Hg and ^{184}Hg, it was possible to obtain sufficient number of γ-ray transitions to evaluate the systematic error by fitting a linear function to the difference between measured and literature value as a function of γ-ray energy, see Figure 4.2.

The energy calibration of the DSSDs was made in two stages. Initial calibration was performed using an open calibrated α-source consisting of ^{239}Pu, ^{241}Am and

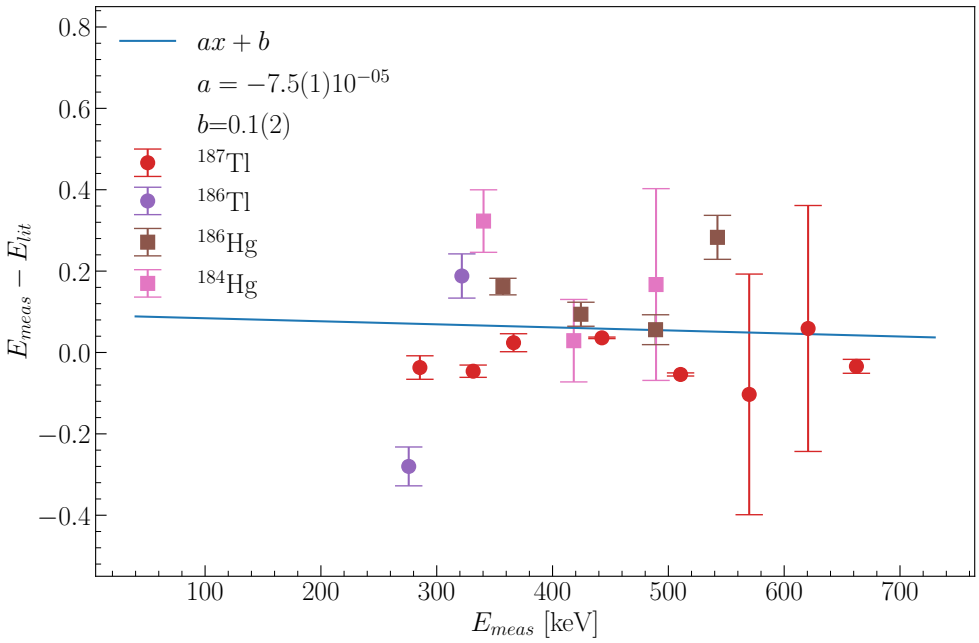

FIGURE 4.2 The difference between γ-ray energies from literature and measurement. The measured values obtained from recoil-gated $\gamma\gamma$-coincidence and literature values from Nuclear Data Sheets. The systematic error was obtained from the intercept parameter b. For validity, data from experiments conducted in Jyväskylä were not used.

^{244}Cm nuclei. The final energy calibration of DSSDs was done using known α decays from nuclei produced in the fusion evaporation reaction and implanted into the DSSD detector. This internal calibration, performed employing α peaks from the ^{186}Pb, ^{183}Hg and ^{185}Hg nuclei, removed effects arising from energy losses in the detector dead layer for α-particles from external α-source.

The PIN diodes were calibrated using the same α-particle source as used for the DSSDs calibration. As the PIN diodes were used for detecting the escaping α-particles from DSSDs, the internal calibration was not needed.

4.3 Recoil identification

The DSSD OR signal was used as an event trigger in the analysis. The event window width was chosen to be 500 ticks (5 μs) with delay of 400 ticks (4 μs). All events in DSSDs; decays, scattered beam or recoil events, opened the event window.

Several different conditions were applied to distinguish between recoil events from events arising from the scattered beam. Energy loss (ΔE) in MWPC and time-of-flight (ToF) for recoil events and scattered beam as a function of DSSD energy is shown in Figure 4.3. It can be seen in Figure 4.3 that all recoil events cause overflow in the DSSDs, in other words, all recoil events are recorded around the maximum channel number 16384. The ΔE of recoils and scattered beam in MWPC as a function of ToF is shown in Figure 4.4 which was also used to identify recoil events. The approximate two-dimensional gate used in analysis for recoil event condition are marked in Figs. 4.3 and 4.4. By gating on prompt γ rays (662 keV and 261 keV) assigned with ^{186}Pb, it was possible to optimise recoil-identification gates.

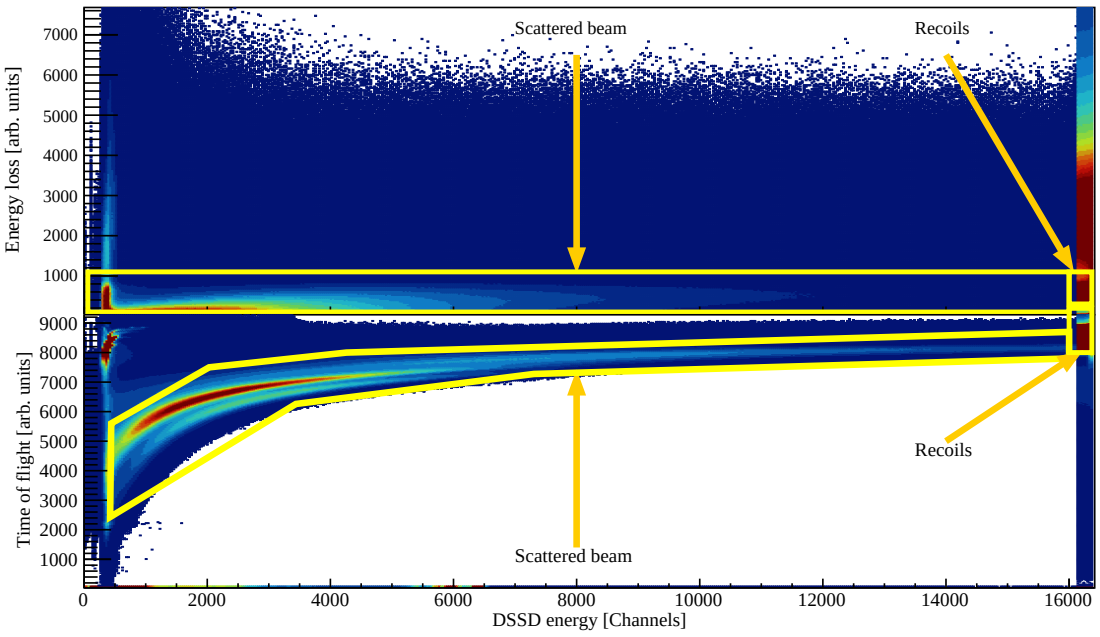

FIGURE 4.3 Top panel: ΔE in MWPC of the recoils and scattered particles as a function of their energy measured in the DSSDs. The fusion-evaporation residues and scattered beam are shown in the small box . All overflow events were considered as recoil events. Bottom panel: ToF of recoils and scattered beam as a function of energy measured in the DSSDs. The fusion-evaporation residues and scattered beam are shown in the small box.

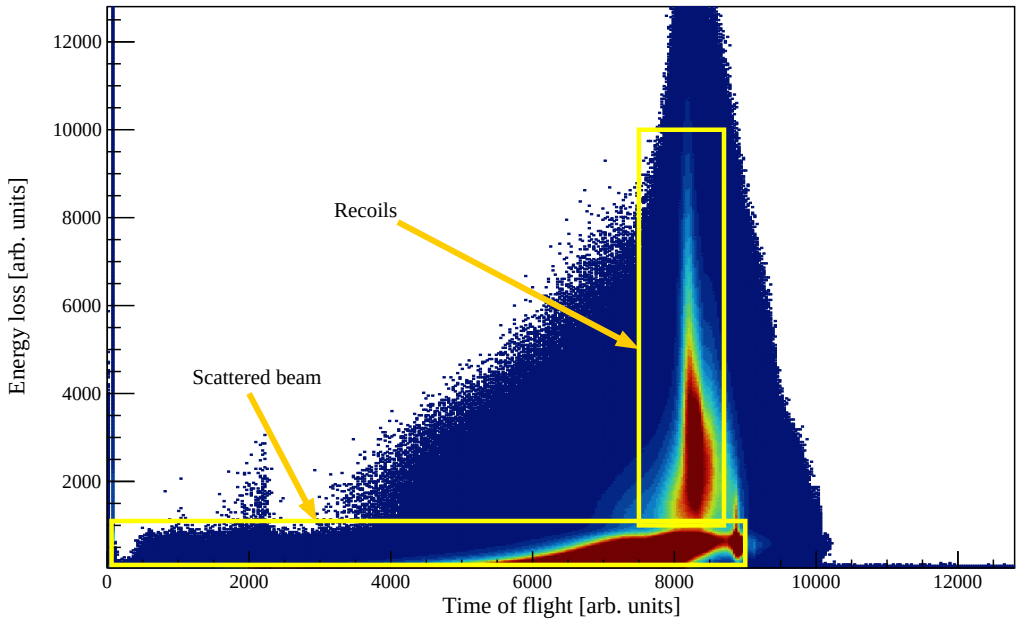

FIGURE 4.4 ΔE of the recoils in the MWPC as a function of ToF between the MWPC and the DSSDs. The fusion-evaporation residues are identified in Tof-ΔEmatrix.

4.4 Recoil-gated prompt γ ray and conversion electrons

The prompt γ rays and conversion electrons associated with recoils could be identified after applying two-dimensional gates on ToF vs. time-difference matrices. Here the time difference means the time elapsed between the event trigger and prompt γ rays (germanium time) or electrons (silicon time). The ToF vs. time-difference matrices can be seen in Figure 4.5 with approximate gates used in the analysis. The beam was delivered from the K130 cyclotron in bunches with time structure corresponding to the cyclotron frequency, causing the high intensity of γ rays and X-rays emitted from the different reactions between the target and beam. The cyclotron frequency is marked in the top panel of Figure 4.5 and it is is naturally same for conversion electrons.

Several open fusion-evaporation reaction channels introduced contaminants, *i.e.* all the other evaporation channels except 3n channel, in the data. On the basis of recoil-gated γ-ray energy spectra, the main fusion-evaporation reaction products were identified as ^{186}Pb, ^{185,186,187}Tl, ^{183,184,186}Hg and ^{183}Au nuclei as shown in Figure 4.6. The γ-ray peak from Coulomb excitation (Coulex) of ^{106}Pd target around 512 keV is broadened due to the Doppler effect.

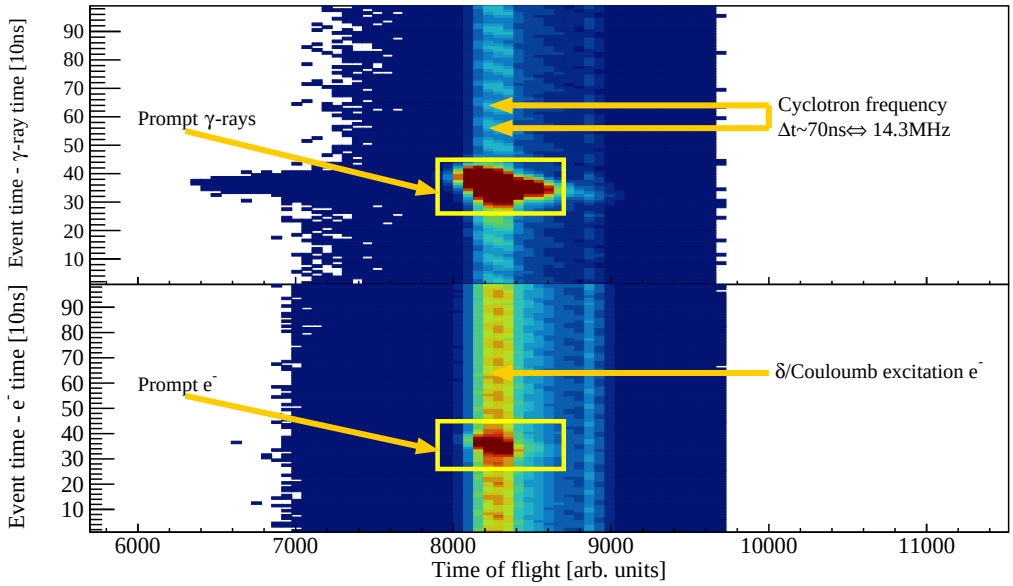

FIGURE 4.5 Top panel: ToF and germanium time matrix. Prompt γ rays from recoils are marked. Bottom panel:ToF and silicon time matrix. Prompt conversion electrons from recoils are marked in figure. The γ-ray blobs are originating from reactions arising from particles in different beam pulses of the cyclotron beam and are labelled as a cyclotron frequency. Cyclotron frequency is marked in the top panel. Due to high delta-electron yield, the prompt electron blob is not as evident as in the case of γ rays.

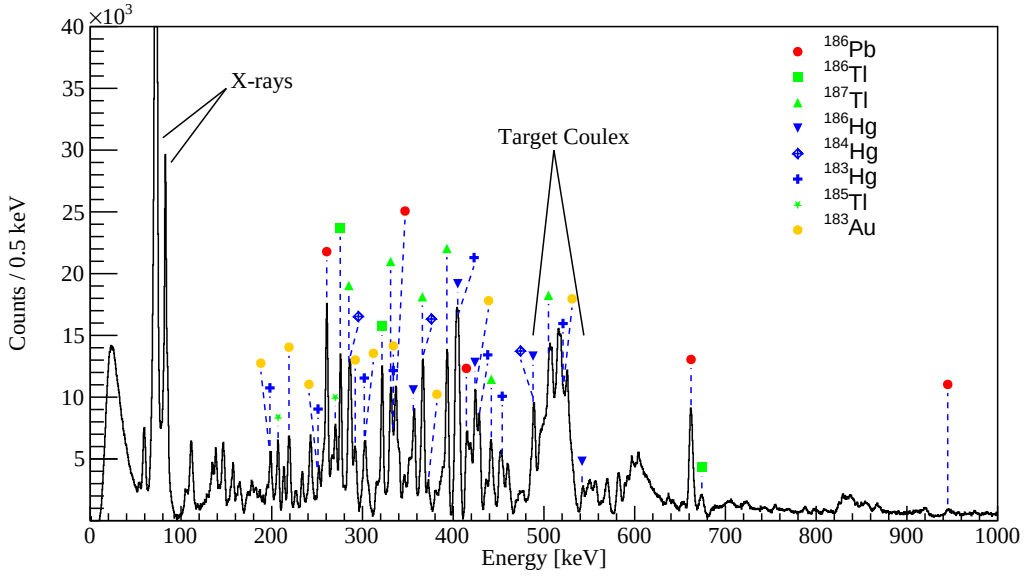

FIGURE 4.6 The recoil-gated, background-subtracted γ-ray energy spectrum obtained in the present work. The most prominent γ-ray peaks are marked and named with origin of nucleus.

The recoil-gated, background-subtracted conversion electron energy spectrum is shown in Figure 4.7. The most prominent electron peaks have been labelled with the nucleus of origin. The δ-electron background was dominating below 100 keV rendering spectroscopy impossible at low energies. The strongest peaks are at 130 keV from the $2^+ \rightarrow 2^+$ transition in ^{186}Hg and at 190 keV from the $11^- \rightarrow 10^-$ transition in ^{186}Tl.

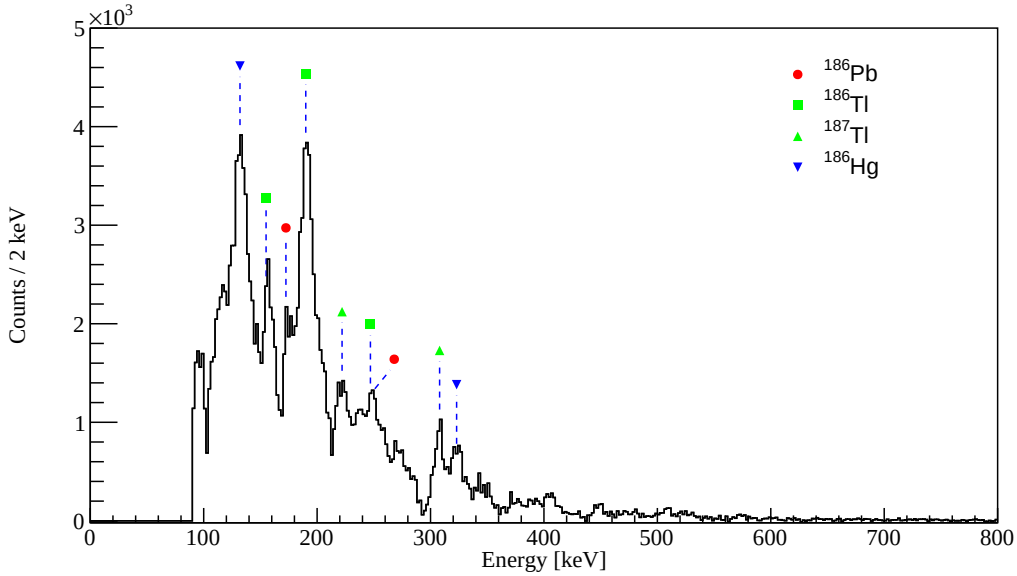

FIGURE 4.7 The recoil-gated, background-subtracted electron energy spectrum obtained in the present work. The most prominent electron peaks are marked in the spectrum and named with origin of nucleus.

4.5 Recoil-α-particle correlation

The gas-vetoed and correlated α-particle energy spectrum is presented in Figure 4.8. The gas-vetoed DSSD energy spectrum includes y-strip events in anti-coincidence with the MWPC, consequently only decay events are present. In the correlated α-particle energy spectrum, it was required that the previous event in a pixel, where the decay event occurred, was a recoil during defined search time. The search time was set to 15 s, which is about three times the half-life of ^{186}Pb $T_{1/2} = 4.83$ s [59]. The α-particle events were also identified and peaks are marked with parent nuclei in Figure 4.8. Most of the α-particle events are decays from recoils, for example ^{183}Hg, ^{183}Au, ^{187}Pb and ^{186}Pb, whereas some can be assigned as second or third generation events in the decay chain, for example ^{182}Hg (arising from α-decay of ^{186}Pb).

Around $\sim$ 80% of observed α-decay events of ^{186}Pb were correlated. Due to

the long search time of 15 s, random correlations with other fusion evaporation products took place. Shorter search time decreases the number of random correlations but naturally also results in fewer statistics, 15 s search time was found to be optimal. α-α-correlation was not possible due to long half-life of the ^{182}Hg ($T_{1/2} = 10.83(6)$ s [60]). Luckily, some of the random correlations are also from ^{186}Pb as 60% of ^{186}Pb recoils decay through β-decay [57]. In Figure 4.8, the α-particle energy gate is marked as a blue-region at the peak assigned with α-decay from ^{186}Pb at $E_\alpha = 6335$ keV [59].

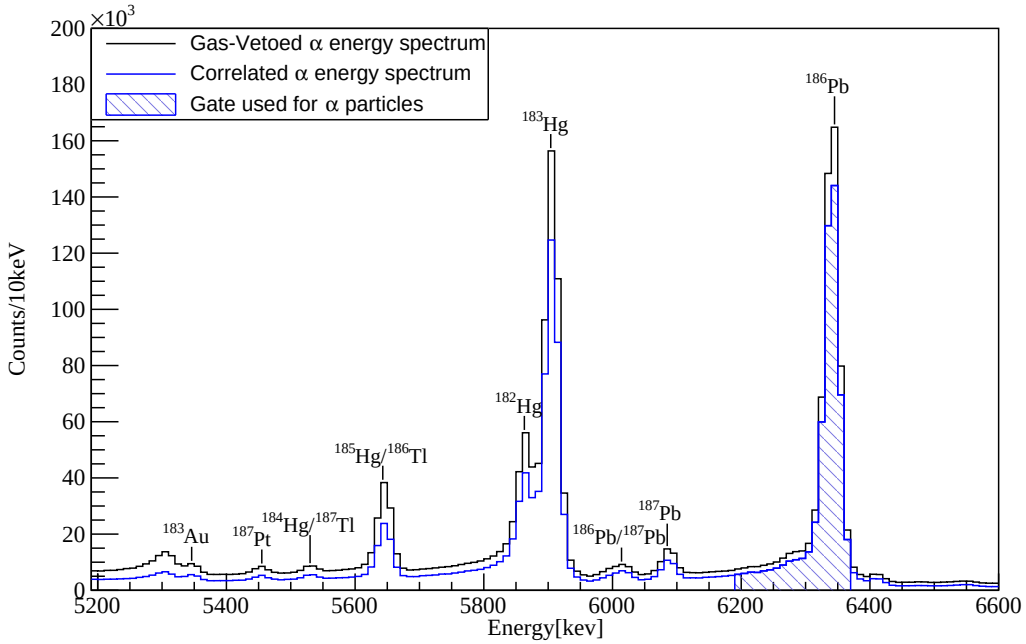

FIGURE 4.8 Gas-vetoed α-particle energy spectrum is marked with the black line. The blue line corresponds the correlated α-particle energy spectrum. The used gate for α-tagging is indicated with blue stripes. The most prominent peaks are labelled [59, 61, 62, 63, 64]

.

4.6 Escaped α particles detection with PIN-diodes

As the α decay occurs near the surface of the DSSDs, the α particle has nearly 50% chance to escape from the DSSDs. Some of the escaped α particles, can be detected with PIN-diodes installed upstream with respect to the DSSDs. As an α-particle escapes from the DSSD, it leaves a fraction of its kinetic energy in the DSSD. This fraction depends on the recoil implantation depth and the decay emission angle. The rest of the α-particle energy is absorbed by the PIN-Diodes. Escaping α particle also loses some energy when it goes through the dead layers of the DSSDs and PIN diodes and, therefore, the sum energy of PIN-diodes and the DSSDs for the ^{186}Pb differs from the literature value and is a function of incident angle in the PIN diodes. Figure 4.9 shows the escaped α-particle energy deposited in the DSSDs and PIN-diodes. An approximate two-dimensional gate is marked in Figure 4.9 with a red ellipse.

The escaped RDT γ-ray energy spectrum together with the RDT γ-ray energy spectrum is shown in Figure 4.10. The escaped RDT tagged γ-ray energy spectrum was produced using the 2D-gate to identify the recoil implanted in the DSSDs. The spectral quality of the escaped RDT γ-ray energy spectrum is similar to that of the RDT γ-ray energy spectrum.

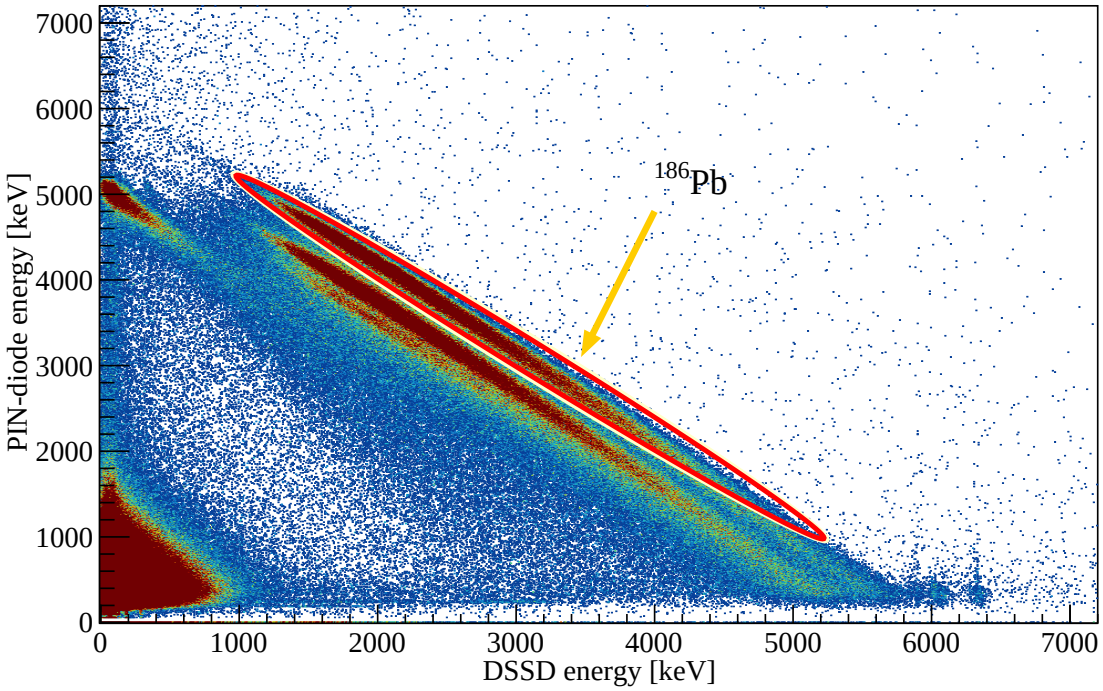

FIGURE 4.9 Correlated PIN-diode energy vs. DSSD energy matrix. The different escaped α-particles from different decaying parent nuclei are mainly from ^{186}Pb and ^{183}Hg. The approximate energy gate for ^{186}Pb is shown as a red ellipse.

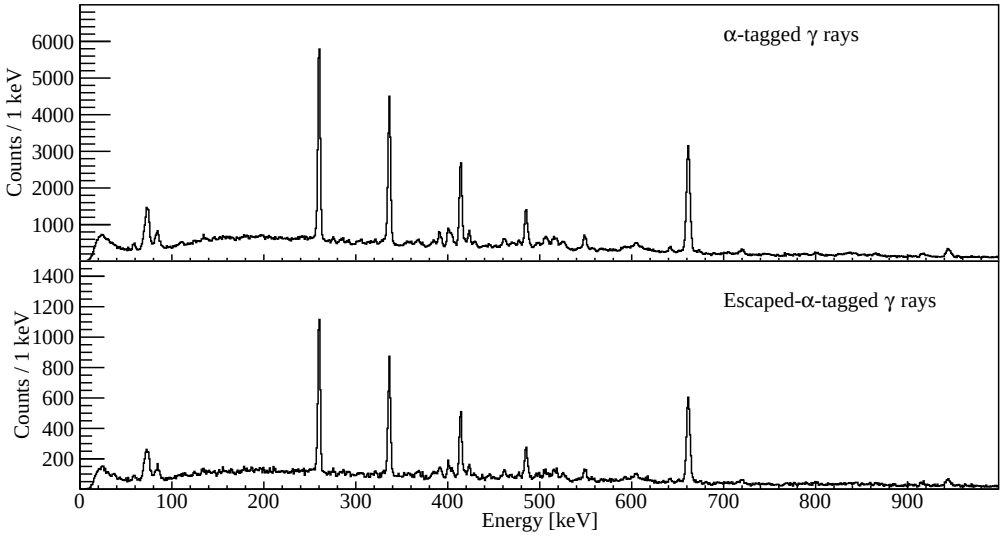

FIGURE 4.10 Recoil-gated, escaped RDT γ-ray and RDT γ-ray energy spectra obtained for ^{186}Pb.

4.7 Estimated production cross-section

The production cross-section of ^{186}Pb was estimated using equation

$$\sigma = \frac{N_\alpha}{I_b t_b \epsilon_{tr} \epsilon_\alpha b_\alpha} \frac{M}{N_A d} \tag{4.5}$$

where N_α is the number of measured full-energy α-particle events of ^{186}Pb recorded in the DSSDs, I_b is intensity of the beam in units of particles/second, t_b is the beam on target time in units of seconds, $\epsilon_{tr} \approx 60\%$ is the transmission of RITU (based on a similar reaction [51]), $\epsilon_\alpha \approx 55\%$ is the efficiency to detect full-energy α particle. $b_\alpha = 40\%$ is the α-decay branching ratio of ^{186}Pb [57], M the molar mass of the target material in units of mg/mol, N_A is the Avogadro constant and d is the target thickness in units of mg/cm^2.

The estimated cross sections for ^{184,186}Hg, ^{185,186,187}Tl were determined from the recoil-gated γ-ray energy spectrum by comparing intensities of transitions listed in Table 4.3, to the intensity of $2_1^+ \rightarrow 0_1^+$ transition in ^{186}Pb. ^{186}Pb, ^{183}Hg and ^{183}Au cross-sections were estimated from α-particle energy spectrum, see Figure 4.8. The estimated cross-sections are listed in Table 4.3. These contaminants are also visible in the RDT γ-ray energy spectrum. The contribution of contaminants were taken into account in analysis. The most problematic contaminant transition was a highly converted $M1$ $11^- \rightarrow 10^-$ transition at 275.6 keV $11^- \rightarrow 10^-$ in ^{186}Tl as it overlaps with the $2_2^+ \rightarrow 2_1^+$ electron peak in ^{186}Pb. See more detailed

discussion in section 4.8.2.

TABLE 4.3 Estimated production cross sections for nuclei produced in the present work. The γ-ray transitions used for estimating cross-sections are listed. If empty, the estimated cross-sections were obtained from α-particle energy spectrum.

Nuclide	Cross-section (μb)	Transition
^{186}Pb	75	
^{186}Tl	70	$(12^-) \rightarrow (11^-)$ [48]
^{187}Tl	82	$(13/2^-) \rightarrow (11/2^-)$ [65, 66]
^{186}Hg	102	$2_1^+ \rightarrow 0_1^+$ [57]
^{183}Hg	114	
^{184}Hg	23	$2_1^+ \rightarrow 0_1^+$ [58]
^{185}Tl	18	$(17/2^-) \rightarrow (13/2^-)$ [66]
^{183}Au	58	

4.8 Results

4.8.1 Properties of transitions in ^{186}Pb obtained with combined γ-ray and electron spectroscopy

The RDT, background-subtracted γ-ray energy spectrum is shown in Figure 4.11. In Figure 4.11, transitions belonging to the yrast and non-yrast band in ^{186}Pb are marked and the 350-510 keV energy range is magnified in the inset. Random correlations were observed due to the relatively long search time.

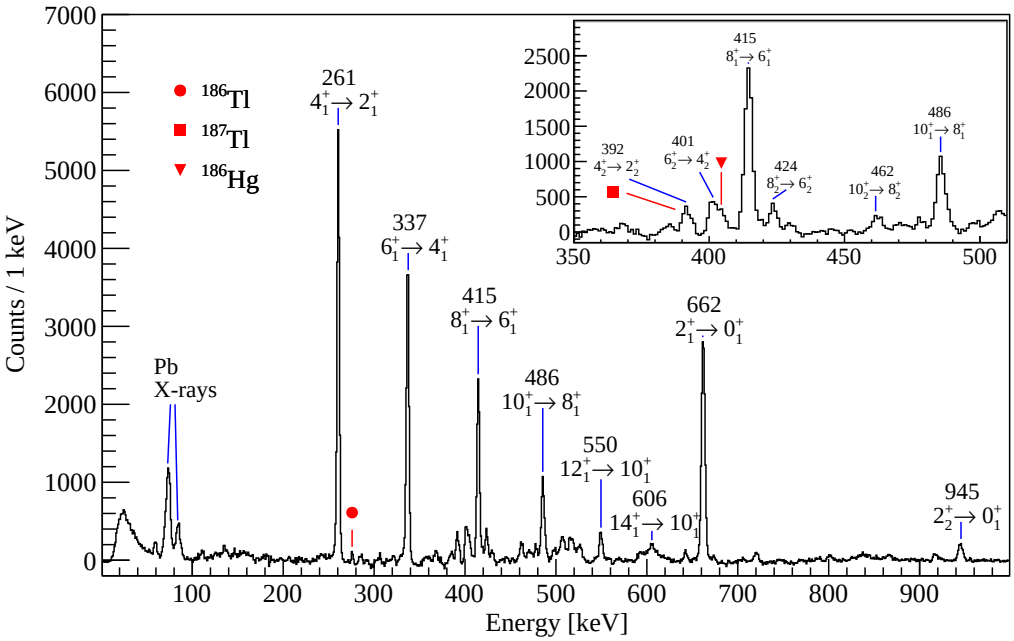

FIGURE 4.11 RDT, background-subtracted γ-ray energy spectrum. The γ-ray peaks assigned with ^{186}Pb are marked with the spins and parities of the initial and final states and transition energies. The most intense contaminants are marked in red. Figure adapted from Ojala *et al.* [67] (CC BY 4.0).

The power of recoil-decay tagging technique, to clean electron energy spectrum from target and beam Coulex and transitions originating from other fusion-evaporation reaction channels, is shown in Fig 4.12. Transitions assigned to ^{186}Pb are barely visible in the recoil-gated electron energy spectrum while employing RDT they become prominent.

The RDT background-subtracted electron energy spectrum is shown in Figure 4.13. The most prominent electron lines are labelled with transition energies and the K-, L- and M-components have been marked. It is noteworthy, that some of these peaks are combinations of different transitions which can be seen in Figure 4.13.

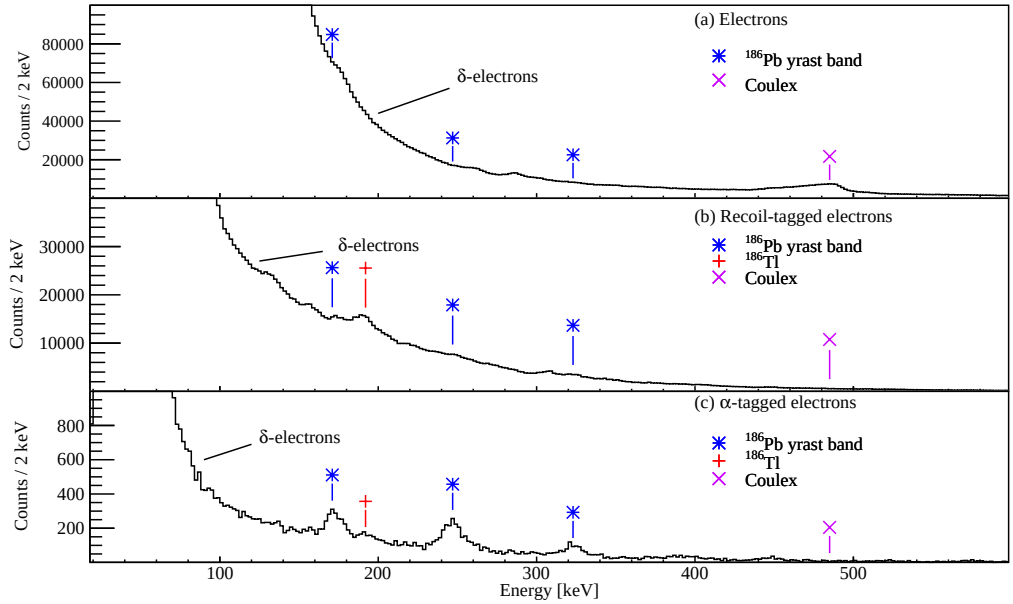

FIGURE 4.12 In panel (a) the total electron energy spectrum, (b) electron energy spectrum gated by recoils and (c) electron energy spectrum gated with recoils which were tagged with α decays of ^{186}Pb

.

The K, $L_{I\text{-}III}$ and $M_{I\text{-}V}$ conversion electron components of the $E2$ and $M1$ transitions are shown in Figure 4.13 as Gaussians with blue colour. The width parameter for these Gaussians were obtained from the 261 keV K-conversion electron peak. The excess electrons, shown as Gaussians with red colour, were obtained from fits which are explained in detail in forthcoming sections. The sum of K, $L_{I\text{-}III}$, $M_{I\text{-}V}$ components and excess electrons is represented with a green colour.

The intensities of γ rays and conversion electrons obtained for transitions in ^{186}Pb are listed in Table 4.4. They were extracted from RDT γ-ray and electron singles, RDT γ-γ and RDT γ-electron coincidence data. For yrast transitions above the 6_1^+ state and non-yrast in-band transitions, the electron intensities could not be extracted due to overlapping electron lines and insufficient γ-electron statistics. Additionally, several transitions from neighbouring nuclei ^{186}Tl, ^{187}Tl and ^{186}Hg had similar transitions energies as ^{186}Pb and therefore needed to be taken into account. The partial level scheme of ^{186}Pb extracted in the present work is shown in Figure 4.14.

The electron line at 173 keV in the RDT electron energy spectrum originates solely from the K-conversion electron component of the $4_1^+ \rightarrow 2_1^+$ transition in ^{186}Pb. Consequently, it was used to extract the width parameter for Gaussian fits. The intensities of the $4_1^+ \rightarrow 2_1^+$ L-electrons and the $6_1^+ \rightarrow 4_1^+$ K-conversion electrons were determined by fitting two Gaussians to the peak at 244 keV.

Using RDT electron singles, γ-ray singles and γ-electron coincidences it was

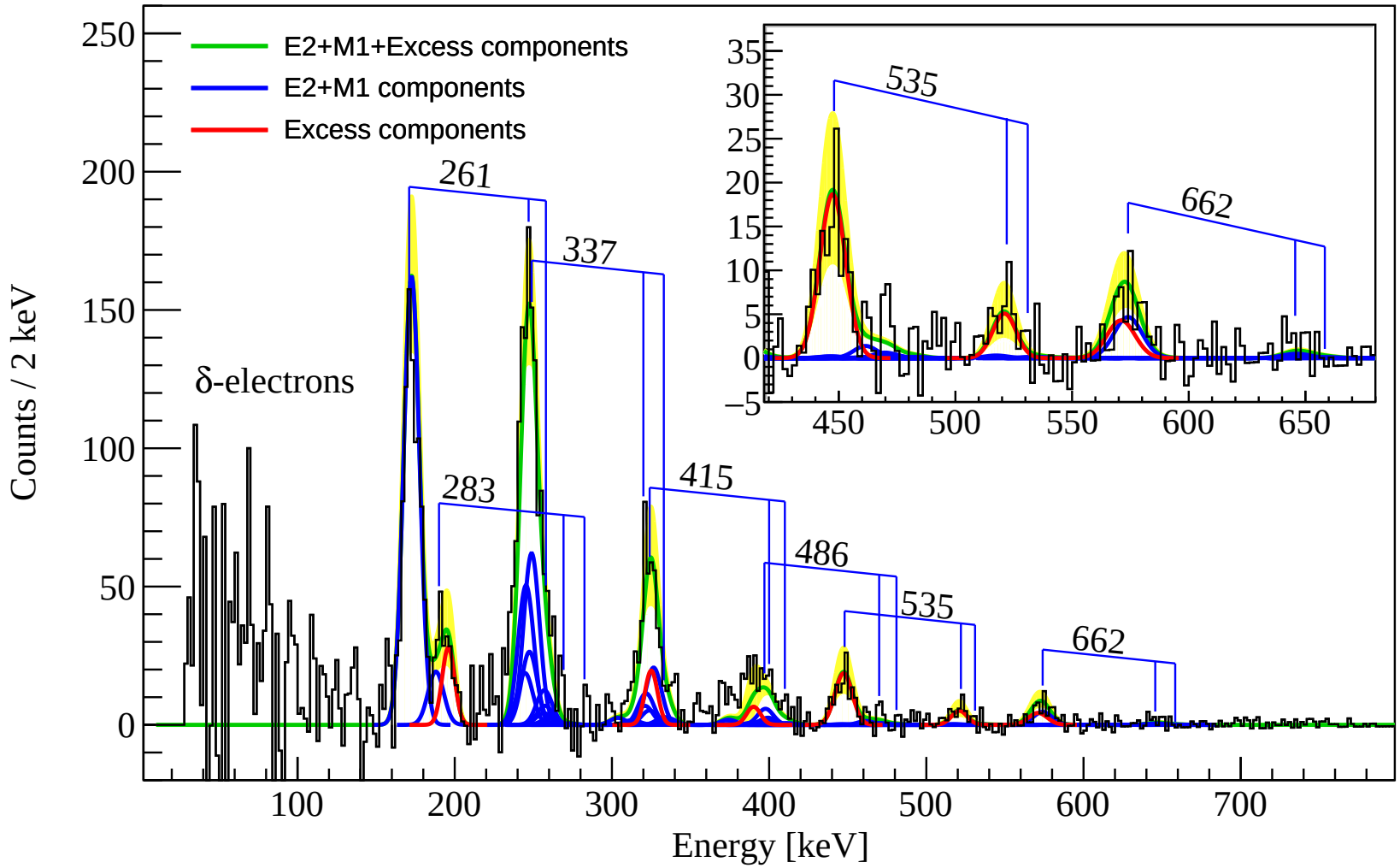

FIGURE 4.13 RDT background-subtracted electron energy spectrum. The K, $L_{I\text{-}III}$, $M_{I\text{-}V}$ -components of the most prominent transitions are marked and labelled with transition energies. The sum of these component is shown with the green line. The blue lines indicate the calculated K, $L_{I\text{-}III}$, $M_{I\text{-}V}$-electron components extracted from the corresponding γ-ray intensities, respectively. The excess electrons are marked with the red line. The δ-electron flux dominates below 150 keV. The inset shows a close-up of high-energy transitions. Figure adapted from Ojala *et al.* [67] (CC BY 4.0).

TABLE 4.4 Energies and intensities of transitions in ^{186}Pb measured in the present work. Unless otherwise noted, intensities are extracted from the measured RDT γ-ray or electron singles energy spectra. Intensities are normalized to the γ-ray intensity of the $2_1^+ \rightarrow 0_1^+$ transition. Table adapted from Ojala *et al.* [67] (CC BY 4.0).

$I_i^\pi \rightarrow I_f^\pi$	$E_{I_i^\pi \rightarrow I_f^\pi}$	I_γ	E_K	I_K	E_L	I_L
Yrast-band transitions						
$2_1^+ \rightarrow 0_1^+$	662.1(2)	1000				
$4_1^+ \rightarrow 2_1^+$	260.6(2)	790(30)	173(1)	60(13)	244(3)	50(15)
$6_1^+ \rightarrow 4_1^+$	337.0(2)	680(22)	248(2)	43(12)		
$8_1^+ \rightarrow 6_1^+$	414.6(2)	445(31)				
$10_1^+ \rightarrow 8_1^+$	485.8(2)	255(9)				
$12_1^+ \rightarrow 10_1^+$	549.6(2)	103(6)				
$14_1^+ \rightarrow 12_1^+$	605.6(4)	34(9)				
Non-yrast band transitions						
$2_2^+ \rightarrow 0_1^+$	945.1(2)	115(4)				
$4_2^+ \rightarrow 2_2^+$	391.9(2)	71(17)				
$6_2^+ \rightarrow 4_2^+$	401.0(2)	66(17)				
$(8_2^+) \rightarrow 6_2^+$	423.8(2)	61(18)				
$(10_2^+) \rightarrow (8_2^+)$	462.2(2)	66(11)				
Interband transitions						
$0_2^+ \rightarrow 0_1^+$	535(2)		447(2)	22(5)	522(2)	8(6)
$0_3^+ \rightarrow 0_1^+$	659(4)		571(4)	11(7)[a]		
$2_1^+ \rightarrow 0_2^+$	127(2)[b]	9(3)[c]	39(1)	4(2)[c]	113(1)	13(4)[b]
$2_2^+ \rightarrow 2_1^+$	283.0(3)[b]	$<$20[d]	196(2)[e]	10(5)[e]		
$4_2^+ \rightarrow 4_1^+$	413.9(4)[f]	38(28)[f]	324(2)[a]	12(8)[a]		
$6_2^+ \rightarrow 6_1^+$	479.0(3)[f]	27(22)[f]				

[a] based on the deconvolution of the corresponding electron peak
[b] extracted from the level energy difference
[c] from RDT $0_2^+ \rightarrow 0_1^+$ K electrons with a gate on the $4_1^+ \rightarrow 2_1^+$ γ-ray transition
[d] from RDT γ rays in coincidence with the $2_1^+ \rightarrow 0_1^+$ γ-ray transition
[e] weighted average, see text for more details
[f] from γ-γ coincidence data

possible to obtain new information of the interband transitions and the band-head states. These are described in more details in the following sections.

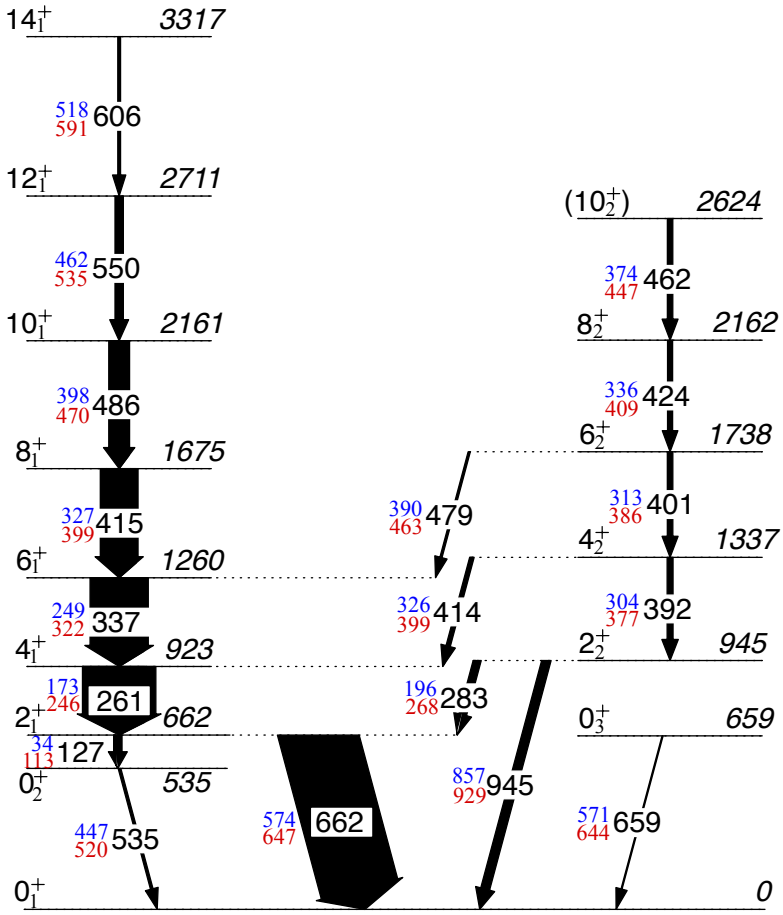

FIGURE 4.14 Partial level scheme of ^{186}Pb. The line width of arrows corresponds to the total intensity. K- and L-conversion electron energies are marked with blue and red next to transition energy, respectively. Figure adapted from Ojala *et al.* [67] (CC BY 4.0).

4.8.2 Quest for the $2_2^+ \rightarrow 2_1^+$ transition: 196 keV electron peak and the non-observation of the corresponding γ-ray transition

The strong electron peak at 196 keV, which corresponds to the K-conversion electron component of the 283 keV transition, is present in the RDT electron energy spectrum. The 196 keV electron peak is associated with the $2_2^+ \rightarrow 2_1^+$ transition by the following arguments. Firstly, the 196 keV electron peak is in coincidence with the 662 keV γ-ray as shown in Figure 4.15. Secondly, the K-conversion electron energy matches well with the K-conversion electron energy for the $2_2^+ \rightarrow 2_1^+$ transition. Thirdly, if the 196 keV electron peak a would be from L-electrons of a non-observed 210 keV transition, the K-conversion electron component at 123 keV

should also be visible in Figure 4.15, which is not the case. The extracted K-conversion electron component intensity at 196 keV energy is a weighted average of intensities resolved from the RDT electron energy spectrum with a gate on the 662 keV γ-ray.

By gating on the 662 keV γ-ray, it was possible to clean the electron energy spectrum from contaminants. The K-conversion electron component intensity of the $2_2^+ \rightarrow 2_1^+$ transition was obtained by normalising to the K-conversion electron component peak of the $4_1^+ \rightarrow 2_1^+$ transition at 173 keV

$$I_{e,K}(196) = \frac{N_e(196)\epsilon(173)}{N_e(173)\epsilon(196)} I_{e,K}(173) = 17(10), \tag{4.6}$$

where $I_{e,K}(196)$ corresponds to the intensity obtained from singles data, $N_e(E)$ is the number of events at energy E and $\epsilon(E)$ is the electron detection efficiency at energy E and $I_{e,K}(173)$ is the measured intensity of the K-conversion electrons of the $4_1^+ \rightarrow 2_1^+$ transition intensity in the RDT singles electron energy spectrum.

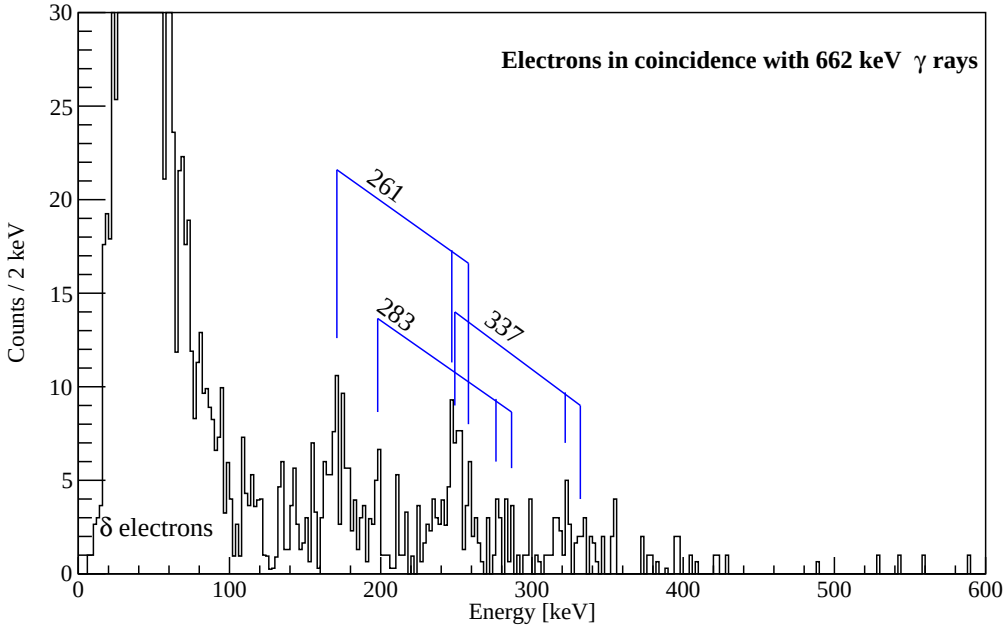

FIGURE 4.15 RDT, electron energy spectrum in coincidence with the 662 keV γ rays. The 283 keV transition is marked together with the two most prominent yrast-band transitions. Figure adapted from Ojala *et al.* [67] (CC BY 4.0).

Unfortunately, the 196 keV peak has a large contribution from different contaminants in RDT singles electron energy spectrum, mainly ^{186}Tl, but it was possible to fit multiple Gaussians and determine the amount of excess electrons, see Figure 4.16. The excess electrons were associated with the $2_2^+ \rightarrow 2_1^+$ transition. The excess electron intensity was determined by integrating counts in the electron

peak at 196 keV and accounting for electrons from ^{186}Tl and ^{187}Tl. The conversion coefficient of the 276 keV transition in ^{186}Tl and the 285 keV transition in ^{187}Tl were obtained from recoil-gated γ-γ and γ-electron coincidence spectrum. Based on deconvolution, the K-conversion intensity of the $2_2^+ \rightarrow 2_1^+$ transition was determined to be $I_{e,K}(196) = 8.2(51)$.

The intense 276 keV transition in ^{186}Tl, assigned as dipole $(11^-) \rightarrow (10^-)$ transition [48], was one the main contaminants in the K-conversion electron line of the $2_2^+ \rightarrow 2_1^+$ transition in ^{186}Pb. Based on the recoil-gated γ-ray and electron coincidence data, $\alpha_K = 0.33(7)$ value was obtained. This is well in line with the calculated value of $\alpha_{K,Calc} = 0.40(1)$ for the $M1$ transition. This conversion coefficient supports the multipolarity presented by Reviol *et al.* [48].

The contaminant nucleus ^{187}Tl has a 285 keV transition but contradicting information regarding its multipolarity exists [65, 66]. In the present work, the K-conversion coefficient of $\alpha_K = 0.08(4)$ was determined by gating on the 392 keV and 394 γ-ray transitions. Due to the small conversion coefficient, the contribution of ^{187}Tl in the 196 keV electron line in the RDT electron energy spectrum is insignificant.

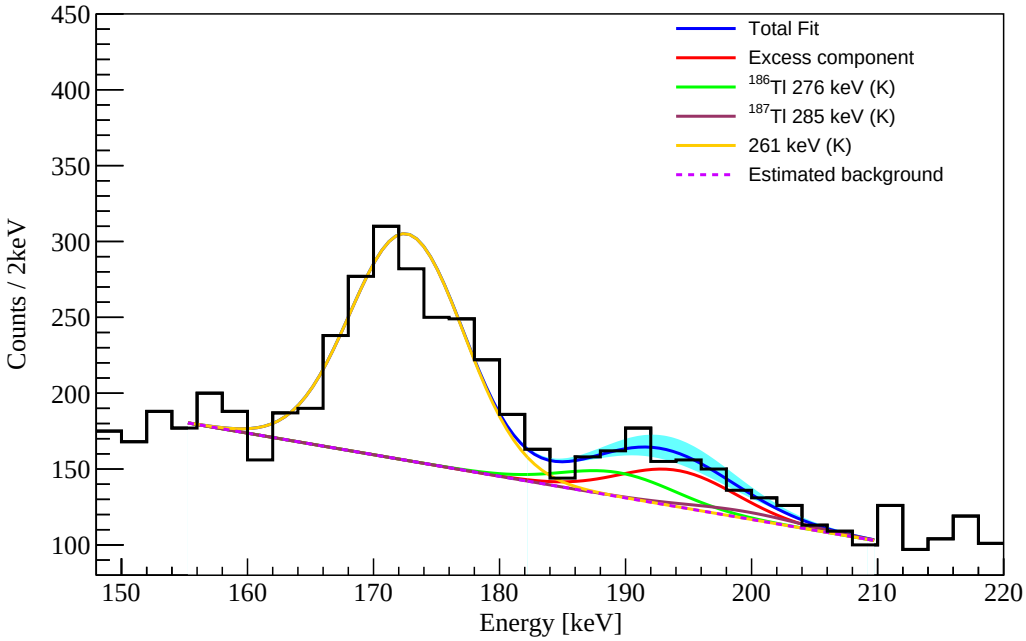

FIGURE 4.16 Close-up of RDT singles electron energy spectrum around 196 keV. The total fit (blue) consists of components determined from the measured γ-ray intensities and the excess electrons are associated with the $2_2^+ \rightarrow 2_1^+$ transition. Components extracted from the observed γ rays are labelled with their transition energies and electron shells of origin. The uncertainty of the total fit is shown with a cyan band and the purple dashed line illustrates the extracted background.

Finally, the intensity was obtained by calculating the weighted average from the intensities which were deduced from the RDT electron energy spectrum and the RDT, 662 keV γ-gated electron energy spectrum. The electron intensity of 196 keV electron was determined to be $I_{e,K}(196) = 10(5)$.

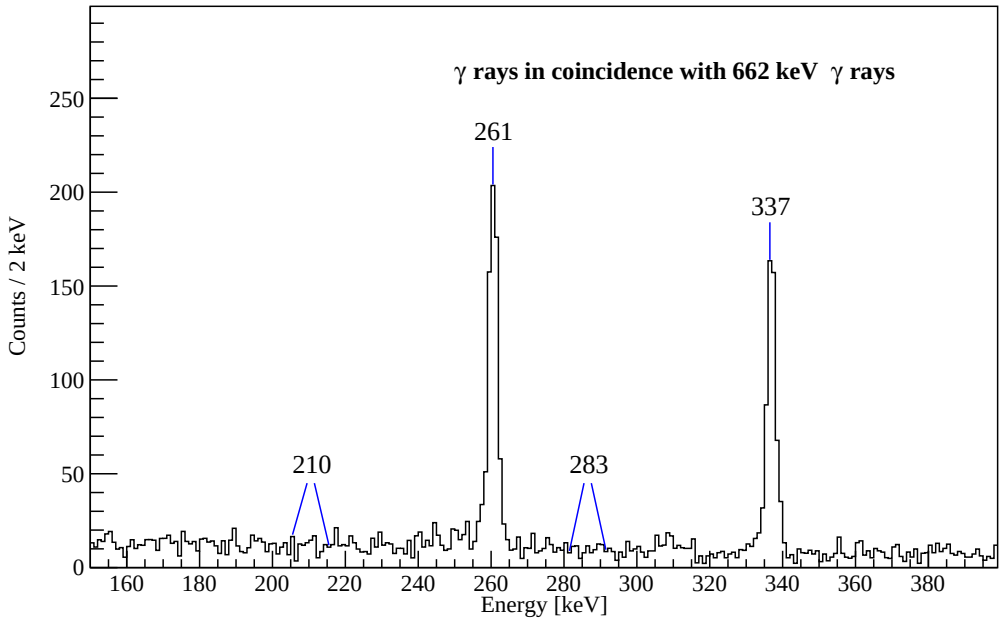

FIGURE 4.17 Close-up from 150 keV to 400 keV of RDT γ-ray energy spectrum requiring coincidence with 662 keV γ rays. The yrast γ rays and the location of 210 keV and 283 keV γ rays are labelled. The absence of 210 keV and 283 keV γ rays would indicate 196 keV electrons are from highly converted transition.

There was no indication of the 286 keV γ-ray transition in ^{186}Pb, which transition would have K-conversion electron line at 196 keV transition. All γ rays in coincidence with the 283 keV peak seen in the RDT γ-ray energy spectrum can be assigned with transitions in ^{187}Tl. The upper limit for the γ-ray intensity of the 283 keV transition was determined from RDT γ-ray energy spectrum gated on the $2_1^+ \rightarrow 0_1^+$ 662 keV transition, shown in Figure 4.17, and employing the critical level L_c defined by Currie [68].

$$I_\gamma(283) < \frac{L_c(283)\epsilon_\gamma(261)}{N_\gamma(261)\epsilon_\gamma(261)} I_\gamma(261) = \frac{2.33\sqrt{B_\gamma}\epsilon_\gamma(261)}{N_\gamma(261)\epsilon_\gamma(261)} I_\gamma(261) = 20, \qquad (4.7)$$

where B_γ is the background counts between 281–286 keV, $N_\gamma(261)$ is the number of 261 keV γ rays and $I_\gamma(261)$ of the $4_1^+ \rightarrow 2_1^+$ transition at 261 keV.

4.8.3 The conversion electron component of the $4_2^+ \rightarrow 4_1^+$ transition: The excess electrons in the 324 keV electron peak

The 324 keV electron peak in the RDT electron energy spectrum is a combination of K-conversion electrons from the $8_1^+ \rightarrow 6_1^+$ and $4_2^+ \rightarrow 4_1^+$ transitions and L-electrons from the $6_1^+ \rightarrow 4_1^+$ transition. Unlike the $8_1^+ \rightarrow 6_1^+$ and $6_1^+ \rightarrow 4_1^+$ $E2$ transitions, the $4_2^+ \rightarrow 4_1^+$ transition can possess $E2$, $M1$ and $E0$ multipolarities. It was observed that the 324 keV electron peak had some excess electrons if the $8_1^+ \rightarrow 6_1^+$, $4_2^+ \rightarrow 4_1^+$ and $6_1^+ \rightarrow 4_1^+$ transitions were assumed to be pure $E2$ transitions. The excess electrons are associated with the $E0$ and possible $M1$ component of the $4_2^+ \rightarrow 4_1^+$ transition. The Gaussian fits of the 324 keV peak are shown in Figure 4.18. The fit, shown in Figure 4.18, was performed by setting fixed parameter for Gaussians of the 337 keV, 415 keV, 392 keV, 401 keV and 414 keV conversion electron peaks. The excess electron component was set as a Gaussian with free parameters except the width parameter. The width parameter was evaluated from the 173 keV electron peak in RDT electron energy spectrum. For the Gaussians with fixed parameters, the peak area parameters were calculated based on the corresponding the γ-ray intensities. The intensity of excess electron component was extracted by subtracting intensities assigned to the $E2$ transitions declared above from the integral of the fit.

The excess electrons energy 324 keV obtained from the fit corresponds to the K-conversion electrons from the 414 keV transition or the L-conversion electrons from the 337 keV transition. The $6_1^+ \rightarrow 4_1^+$ 337 keV transition is a known stretched $E2$ transition [10, 48] and the corresponding L-conversion electron intensity can be calculated with high precision. The L-conversion electron intensity is insufficient to explain the electron excess in the peak, thus the excess is assigned to the $E0$ $4_2^+ \rightarrow 4_1^+$ transition.

γ rays from the $4_2^+ \rightarrow 4_1^+$ transition have been previously observed [9]. In the present work, the γ-ray intensity is determined by normalising the 414 keV γ-ray intensity to the 391 keV γ-ray, which is obtained from RDT γ-ray energy spectrum with a gate on the 401 keV transition shown in Figure 4.19. This normalisation can be written in an equation form as follows. The α_K conversion coefficient value of 0.0312(5) was obtained for the $4_2^+ \rightarrow 4_1^+$ transition, see Table 4.5.

$$I_\gamma(414) = \frac{N_\gamma(414)\epsilon(391)}{N_\gamma(391)\epsilon(414)} I_\gamma(391) = 38(28), \tag{4.8}$$

where $I_\gamma(414)$ and $I_\gamma(391)$ corresponds to the 414 keV and 391 keV γ-ray intensity, $N_\gamma(E)$ is the number of 401 keV γ rays in coincidence with γ rays at energy of E. The γ-ray intensity ratio between the 391 keV and 414 keV transitions, $I_\gamma(391)/I_\gamma(414) = 0.54(37)$, is well in line with the previously obtained value of $I_\gamma(391)/I_\gamma(414) = 0.53(20)$ [10].

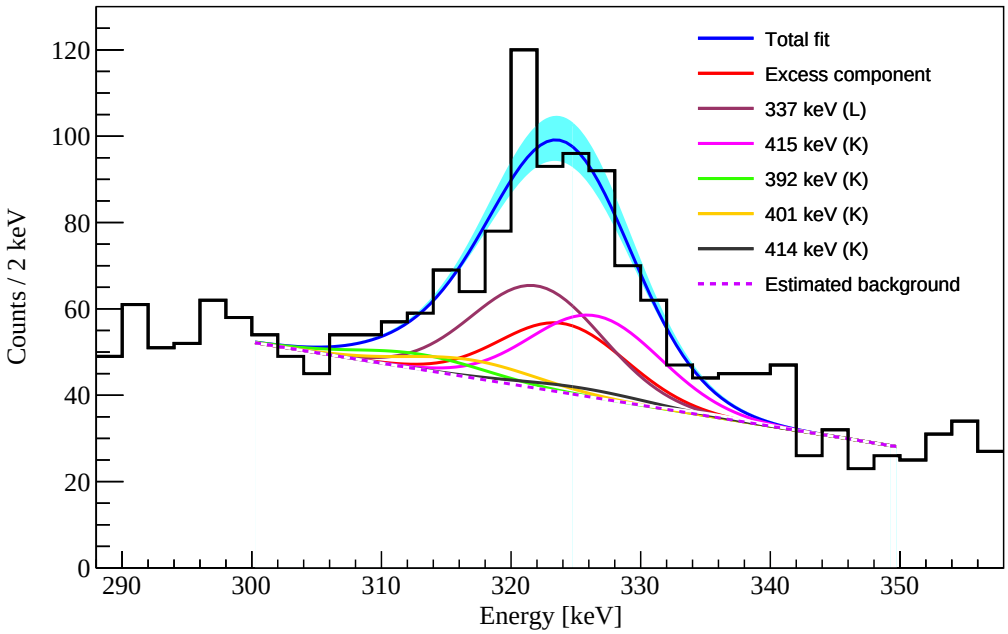

FIGURE 4.18 Close-up of the RDT electron energy spectrum around 325 keV. The total fit (blue) consists of components determined from the measured γ-ray intensities and the excess electrons are associated with the $4_2^+ \rightarrow 4_1^+$ transition. Components extracted from the observed γ rays are labelled according to transition energies and electron shells of origin. The uncertainty of the total fit is shown with a cyan band and the purple dashed line illustrates the extracted background. Figure adapted from Ojala *et al.* [67] (CC BY 4.0).

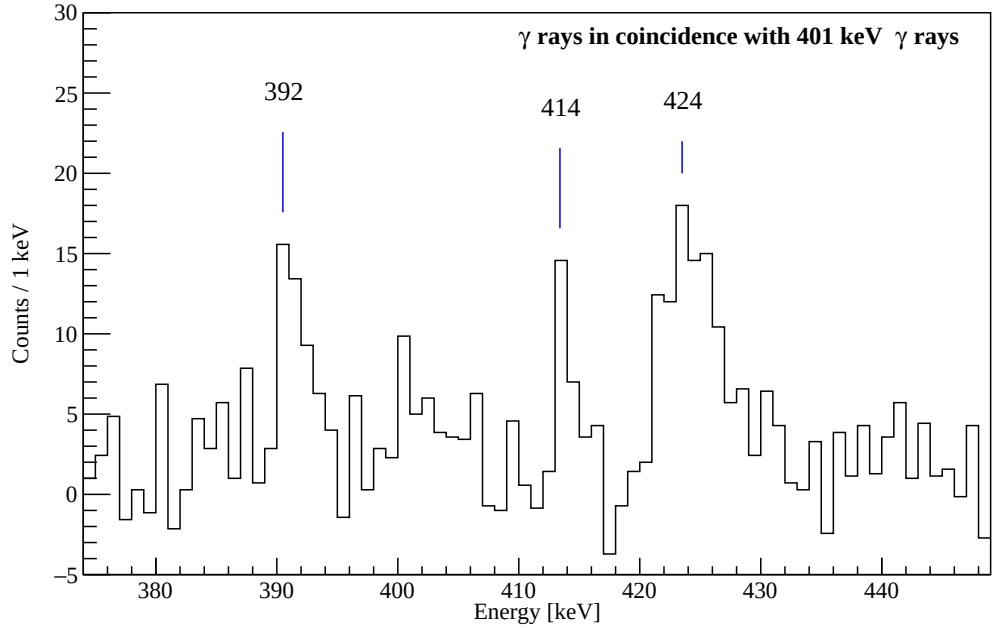

FIGURE 4.19 Close-up of energy range from 375 keV to 450 keV of RDT γ-ray energy spectrum requiring a coincidence with 401 keV γ rays. The non-yrast transitions are labelled and the 414 keV transition corresponds to the $4_2^+ \rightarrow 4_1^+$ γ-ray transition.

4.8.4 The first observation of the $0_2^+ \rightarrow 0_1^+$ transition in-beam: electron peaks at 447 keV and 519 keV

In the RDT electron energy spectrum, the 447 keV peak stands out clearly, as shown in Figure 4.13. The electron peak at 447 keV is assigned as the $0_2^+ \rightarrow 0_1^+$ transition based on the following arguments. Firstly, the 535 keV γ-ray was not observed. Secondly, the L-electron of 535 keV transition was observed, which can be seen in Figure 4.13 and thirdly, the energy agrees well with the 0_2^+ state at energy 530(21) keV [69] which was observed by Andreyev *et al.* [8] in an α-decay spectroscopy of ^{190}Po. Finally, the γ-electron coincidences show that the $0_2^+ \rightarrow 0_1^+$ 535 keV transition is in coincidence with the yrast band and with the 127 keV transition feeding the 0_2^+ state, see Figure 4.20. The 127 keV transition, was observed for the first time in this experiment. Additionally, the 447 keV electrons are not in coincidence with the $2_1^+ \rightarrow 0_1^+$ 662 keV transition (see Figure 4.15) which fit well in this picture. If the 447 keV electron peak originated from the L-conversion electrons of 462 keV transition, an intensive K-conversion electron component peak at 374 keV would be expected, which clearly is not the case.

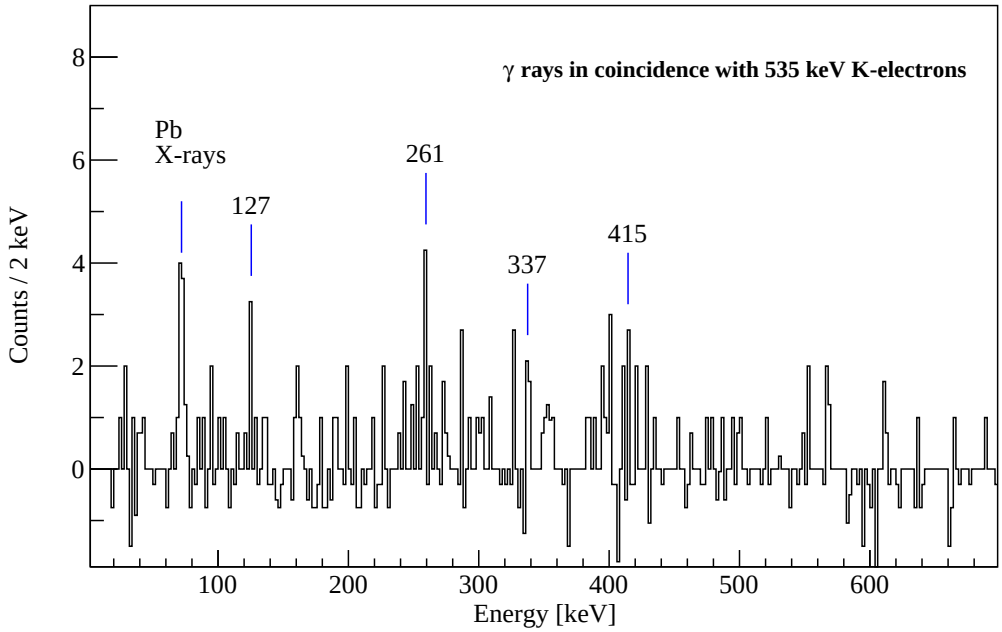

FIGURE 4.20 The RDT γ-ray energy spectrum in coincidence with 447 keV electrons. The yrast band transitions and the 127 keV transition feeding to the 0_2^+ state are labelled. Figure adapted from Ojala *et al.* [67] (CC BY 4.0).

The K-electron intensity of the 535 keV transition $I_K(535) = 22(5)$ was determined from the RDT electron energy spectrum by taking into account the L-electron of the $10_1^+ \rightarrow 8_1^+$ and the K-electrons of the $12_1^+ \rightarrow 8_1^+$ transition. In a similar manner,

the L-electrons of the 535 keV transition with an intensity of $I_L(535) = 8(6)$ was determined. The K/L intensity ratio $K/L = 3(2)$ was calculated. Due to the small statistics in the L-electron peak, the uncertainty of the K/L ratio is large. Still the best argument for an $E0$ multipolarity for the 535 keV transition is the non-observation of a corresponding γ-ray.

The feeding of the 0_2^+ state from the 2_1^+ state with a transition energy of 127 keV has not been observed before this work. This is most likely due to the large conversion coefficient $\alpha_{tot}(E2) = 2.35$ of the 127 keV transition and insufficient γ-γ statistics. Using γ-electron coincidences, the 127 keV transition can be observed. The total intensity was extracted from the electrons associated with the 535 keV transition in coincidence with the 261 keV $4_1^+ \rightarrow 2_1^+$ γ-ray transition (see Figure 4.21) by normalising to the weighted average of intensities associated with K-electrons from the 337 keV, 414 keV and 662 keV transitions. Normalised γ-ray intensity for the 127 keV transition were obtained in the same manner as described in section 4.8.3 for the $4_2^+ \rightarrow 4_1^+$ transition.

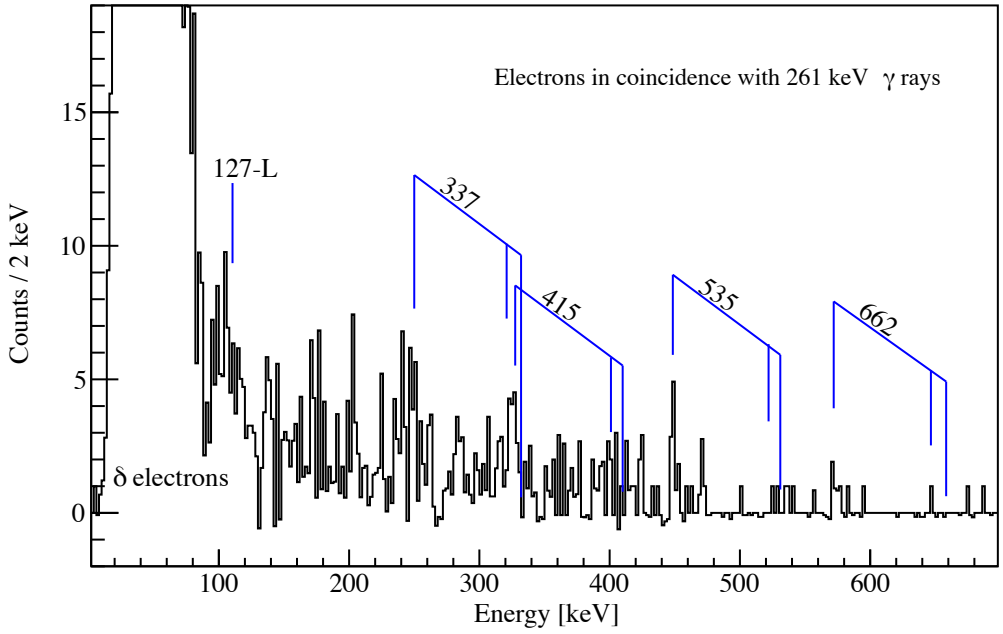

FIGURE 4.21 The RDT electron energy spectrum in coincidence with 261 keV γ rays. The locations of yrast transitions and the feeding 127 keV transition to the 0_2^+ state are labelled. Figure adapted from Ojala *et al.* [67] (CC BY 4.0).

Based on the obtained total intensities of $I_{tot}(127) = 31(10)$ and $I_{tot}(535) = 26(6)$ for the 127 keV and 535 keV transitions, respectively, the majority of the 0_2^+ state feeding comes from the yrast band. Feeding from the non-yrast states was not observed.

4.8.5 The $0_3^+ \rightarrow 0_1^+$ transition: excess electrons in the 574 keV electron peak

Based on the γ-ray intensity, the intensity of the 574 keV electron peak is much larger than expected solely for the 662 keV $2_1^+ \rightarrow 0_1^+$ K-conversion transition, which is shown in figure Figure 4.13. If the excess was due to some L-conversion electron component, there would be a larger electron peak at 500 keV from the K-conversion electron component compared to the 574 keV excess electrons, but clearly this is not the case. Consequently, the excess electrons have to originate from the K-conversion electron component. The energy of the excess electron peak matches well with the 649(21) keV [69] energy of the 0_3^+ state observed by Andreyev *et al.* [8]. Since the corresponding γ-ray transition was not observed, the excess electrons were assigned as the K-conversion electron component of the $0_3^+ \rightarrow 0_1^+$ transition.

The energy of this transition was determined by fitting two Gaussians to the 574 keV peak in a similar manner as in sections 4.8.2 and 4.8.3. The 662 keV K-conversion electron component peak parameters were fixed based on typical peaks in the RDT γ-ray energy spectrum. Based on the fit, the K-conversion electron energy 571(4) keV and the $0_3^+ \rightarrow 0_1^+$ transition intensity of 11(7) were obtained.

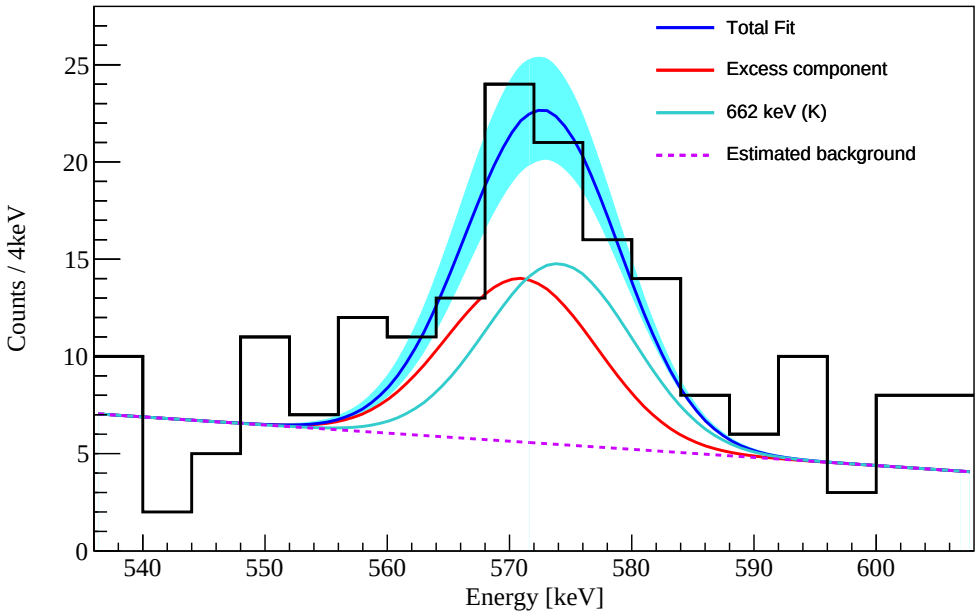

FIGURE 4.22 Close up of the RDT electron energy spectrum. The total fit (blue) consists of K-conversion electron component of the $2_1^+ \rightarrow 0_1^+$ transition at 662 keV (light blue) and an excess component (red). The uncertainty of the total fit is shown with a cyan band and the purple dashed line illustrates the extracted background. Figure adapted from Ojala *et al.* [67] (CC BY 4.0).

4.8.6 The potential K-conversion electron components from the $6_2^+ \rightarrow 6_1^+$ transition: deconvolution of the electron peak at 400 keV

The electron peak at 400 keV in the RDT electron spectrum consists of the following components: K-conversion electron components of the 486 keV, 479 keV, 462 keV and 487 keV transitions and L-electrons of the 415 keV, 391 keV, 401 keV and 424 keV transitions. While accounting for all of these components, there is still some excess electrons as shown in Figure 4.23.

The intensity of the excess component of the 400 keV electron peak , $I_e(390) = 6(7)$, is obtained in a similar manner as the intensity of the $4_2^+ \rightarrow 4_1^+$ transition (see section 4.8.3) and is associated with the $6_2^+ \rightarrow 6_1^+$ transition. The electron intensity has a large uncertainty due to low statistics and a complex fit function model. Also, one would need to take into account the intensity corresponding to the L-electron component of the $E0$ and $M1$ $4_2^+ \rightarrow 4_1^+$ transition which would increase the uncertainty of intensity of the $E0$ $6_2^+ \rightarrow 6_1^+$ transition even more. Also, a possible $8_2^+ \rightarrow 8_1^+$ transition would have transition energy of 487 keV and the corresponding K-conversion electron component energy of 399 keV, would further increase the uncertainty of the excess intensity of the $6_2^+ \rightarrow 6_1^+$ transition. Consequently, it was not possible to unambiguously determine of the origin of the excess electron intensity of the 400 keV peak.

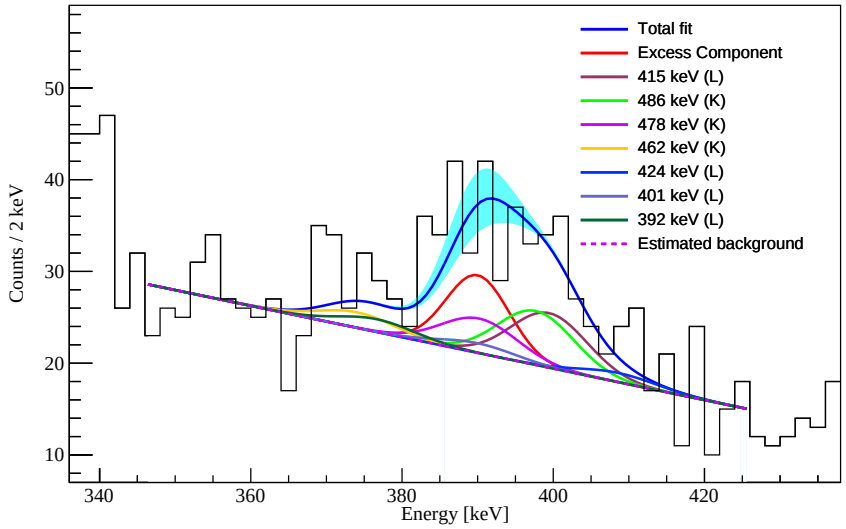

FIGURE 4.23 Close-up of energy range from 330 keV to 440 keV of the RDT electron-energy spectrum. The total fit (blue) consists of components determined from the measured γ-ray intensities and the excess electrons are associated with the $6_2^+ \rightarrow 6_1^+$ transition. Components extracted from the observed γ rays are labelled according to transition energies and the electron shells of origin. The uncertainty of the total fit is shown with a cyan band and the purple dashed line illustrates the extracted background.

4.8.7 Internal conversion coefficients

Conversion coefficients obtained in this work are presented and compared with calculated values in Table 4.4. In case of the $4_2^+ \rightarrow 4_1^+$transition, α_K was extracted assuming that all other components in the peak were $E2$ transitions, for more detailed discussion see Section 4.8.3. The lower limit of the K-conversion coefficient for the $2_2^+ \rightarrow 2_1^+$ transition was obtained. γ-electron coincidence relations allowed for distinguishing the K-conversion electrons of $6_1^+ \rightarrow 4_1^+$ transitions at 244 keV from the L-conversion electrons $4_1^+ \rightarrow 2_1^+$ at 248 keV.

TABLE 4.5 Conversion coefficients obtained for transitions in ^{186}Pb. For comparison, calculated values for pure $E2$ and $M1$ transitions are also given [14].

Transition	E_γ(keV)	$\alpha_K(Exp)$	$\alpha_K(E2)$	$\alpha_K(M1)$	$\alpha_L(Exp)$	$\alpha_L(E2)$	$\alpha_L(M1)$
$4_1^+ \rightarrow 2_1^+$	260.6	0.076(16)	0.091(2)	0.513(8)	0.064(16)	0.065(1)	0.088(1)
$6_1^+ \rightarrow 4_1^+$	337.0	0.063(17)	0.050(1)	0.254(4)			
$2_2^+ \rightarrow 2_1^+$	283.0	>0.5	0.075(2)	0.409(6)			
$4_2^+ \rightarrow 4_1^+$	413.9	0.323(303)	0.031(1)	0.146(3)			

4.9 Discussion

4.9.1 The band-head 0_2^+ and 0_3^+ states

The band-heads of the yrast and non-yrast bands have not been observed before in an in-beam experiment. The feeding to the band-head states is rather weak as it has to compete against higher energy transitions (662 keV and 945 keV) to the 0_1^+ state. The 0_2^+ and 0_3^+ states have been observed in the ^{190}Po α-decay experiment performed by Andreyev *et al.* [8].

As the lifetime [23] and the branching ratio of transitions from the 2_1^+ state is known, the reduced transition probability can be determined as

$$B(E2; 2_1 \rightarrow 0_2^+) = \frac{I_\gamma(127)}{(5.940 \times 10^{-2} A^{4/3})(1.223 \times 10^9 E_\gamma^5)(I_{tot}(2_1^+))} \frac{1}{\tau(2_1^+)} \quad (4.9)$$

$$= 190(80)\,\text{W.u.}, \quad (4.10)$$

where $I_\gamma(127)$ is the γ-ray intensity of the $2_1^+ \rightarrow 0_2^+$ 127 keV transition, A is the mass number of ^{186}Pb, E_γ is the γ-ray energy in MeV, $I_{tot}(2_1^+) = I_\gamma(662)(1 + \alpha_{tot}(662)) + I_\gamma(127)(1 + \alpha_{tot}(662))$ is the sum of transition intensities for transitions de-exciting the 2_1^+ state and $\tau(2_1^+)$ =18(5) ps is the mean lifetime of the 2_1^+ state [23].

Using the obtained value of $B(E2; 2_1^+ \rightarrow 0_2^+) = 190(80)$ W.u. and Equation 2.22, it was possible to extract the transitional quadrupole moment $|Q_t| = 7.7(33)$ for the $2_1^+ \rightarrow 0_2^+$ transition. As shown in Figure 4.24, the transitional quadrupole moment is well in line with the one obtained for the other members of the prolate band transitions. As for comparison, the 4_1^+ state in ^{188}Pb is substantially mixed. The $|Q_t|$ values for ^{194}Po represent those for an oblate band, which are typically lower than in prolate ones [49].

The mixing amplitude for the 0_1^+ state was obtained by using the pure prolate quadrupole moment and $B(E2; 2_1 \rightarrow 0_2^+) = 190(80)$ W.u. in Equation 2.36, which gives $a^2 = 0.75$. In this calculations, the 2_1^+ state was assumed to be a pure member of the yrast band. The prolate quadrupole moment was obtained by taking the weighted average of quadrupole moments for transitions above the 4^+ yrast state in ^{186}Pb and above the 6^+ yrast state in ^{188}Pb which gives $|Q_{t,prolate}| = 9.0(5)eb$. The extracted $Q_{t,prolate}$ and mixing amplitude suggest the 0_2^+ state is predominantly prolate and the band-head of the yrast band. Further evidence to assign the 0_2^+ state as the yrast-band member comes from extracted total intensity of the 127 keV transition as $I_{tot}(127) = 31(10)$ covers the total intensity of the $0_2^+ \rightarrow 0_1^+$ 535 keV transition $I_{tot}(535) = 26(6)$ completely which leaves little room for side feeding, *i.e.* feeding from the 2_2^+ state.

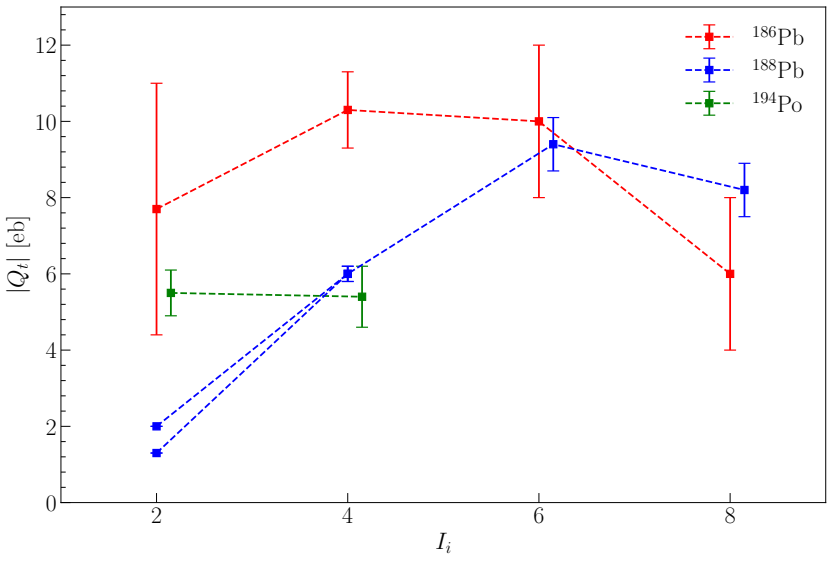

FIGURE 4.24 The transitional quadrupole moments Q_t plotted as a function of angular momentum of the initial state. The Q_t values are taken from reference [23], except for the Q_t of the $2_1^+ \rightarrow 0_2^+$ transition in ^{186}Pb, which is obtained in this work. The drop of Q_t value for tthe $2_1^+ \rightarrow 0_1^+$ transition in ^{188}Pb is mainly caused by change of shape from prolate to spherical ground state. The 4_1^+ states in ^{188}Pb and ^{194}Po are examples of mixed configurations and an oblate deformed band, respectively.

Alternatively, one could assume the 0_2^+ state being part of the non-yrast band. If the transition probabilities $B(E2; 2_2 \rightarrow 0_2^+) = 50$ W.u. and $B(E2; 2_2 \rightarrow 0_1^+) = 5$ W.u. are assumed, the intensity of the $2_2^+ \rightarrow 0_2^+$ transition can be estimated to be

$$I_\gamma(410) = \frac{410\,\mathrm{keV}^5 B(E2; 2_2 \rightarrow 0_2^+)}{945\,\mathrm{keV}^5 B(E2; 2_2 \rightarrow 0_1^+)} 115 = 19(2). \tag{4.11}$$

While the 410 keV transition was beyond the observational limit, the value extracted above does not agree with the intensity balances obtained for in- ($I_{tot}(2_1^+ \rightarrow 0_2^+) = 30(10)$) and out-transitions ($I_{tot}(0_2^+ \rightarrow 0_1^+) = 25(6)$) of the 0_2^+ state. This would indicate that there is no strong feeding from the non-yrast states to the 0_2^+ state.

Configuration mixing between the 0_3^+ and 0_2^+ states can be estimated using Equation 2.32. Applying typical prolate and oblate quadrupole deformation values of β_2=0.29(5) and β_2=0.17(3) [23], one can obtain $\rho^2(0_3^+ \rightarrow 0_2^+) = 290 \times 10^{-3}$ assuming maximal prolate-oblate mixing (a^2=b^2=0.5). With the obtained $\rho^2(0_3^+ \rightarrow 0_2^+)$ value and the total intensity of $I_{total}(0_3^+ \rightarrow 0_1^+) = I_K(0_3^+ \rightarrow 0_1^+)\mathrm{K/Tot} = 13(8)$ (The ratio of emitted K and total electrons K/Tot is obtained with BrIcc [14]), the total intensity for the $0_3^+ \rightarrow 0_2^+$ transition can be calculated to be $I_{total}(0_3^+ \rightarrow 0_2^+) = 170(100)$. Consequently, an L-electron peak at 108 keV with an intensity of $29(17)$ should be observed in the RDT electron energy spectrum but clearly that is not the case. This result points out that there would be a fairly low configuration mixing between the 0_2^+ and 0_3^+states.

Based on the $B(E2; 2_1 \rightarrow 0_2^+)$ and $Q_t(2_1 \rightarrow 0_2^+)$ values, the 0_2^+ state is considered to be a member of the yrast band rather than the non-yrast band. Results also show that the 0_2^+ state is predominantly prolate and configuration mixing is low. The level energy systematics of neutron-deficient Pb nuclei, with the newly assigned configuration for the 0^+ states is shown in Figure 4.25. Moreover, the kinematic moments of inertia plot shown in Figure 4.26 shows that the 0_2^+ state follows curves for typical prolate bands and the 0_3^+ state fits well with an oblate configuration.

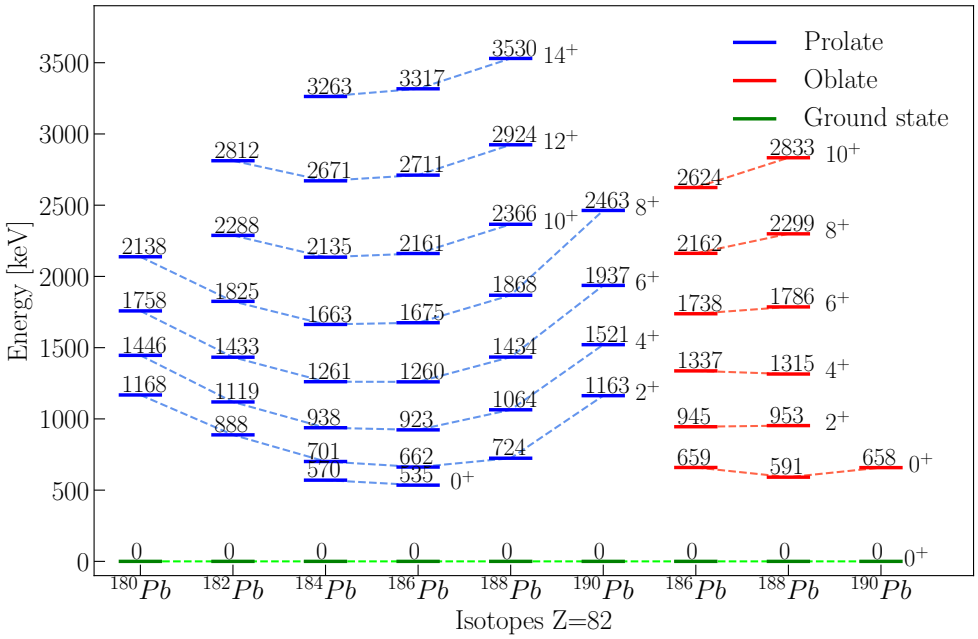

FIGURE 4.25 Level energy systematics for Pb nuclei [58, 70, 60, 71, 72, 73]. The states assigned with prolate shape are coloured with blue, oblate shape are coloured with red and spherical shape are coloured with green. The energy of states is written on top of states. The states with the same shape and angular momentum are connected with a dashed line.

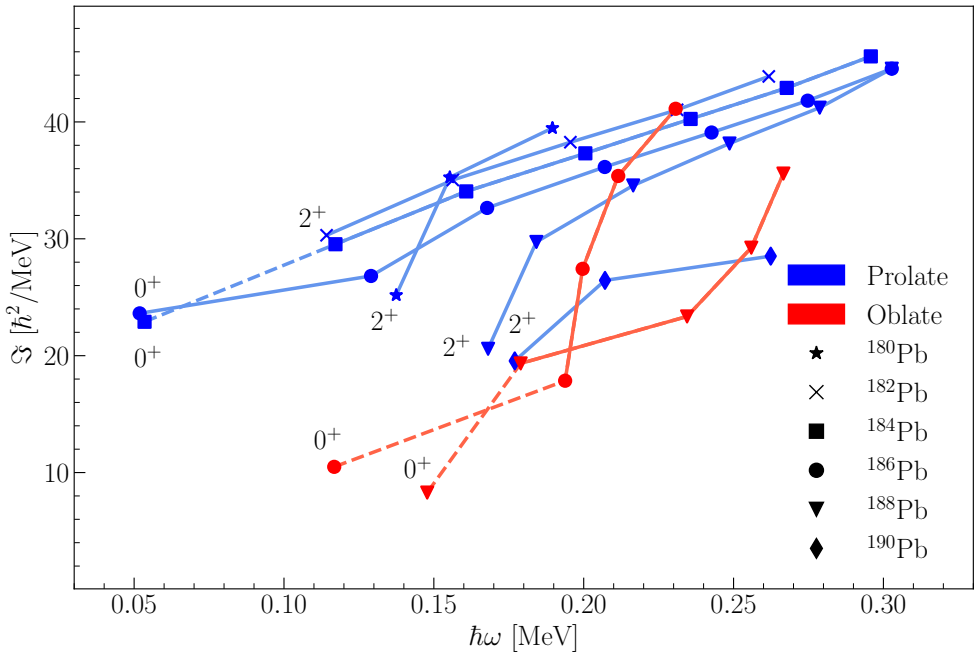

FIGURE 4.26 Kinematic moment of inertia for $^{180-190}$Pb nuclei [58, 70, 60, 71, 72, 73]. The states assigned with prolate shape are coloured with blue and the oblate shape are coloured with red. The final state is marked for different configurations. The states used in this plot are same as shown in Figure 4.25. Note that the $2^+ \rightarrow 0^+$ transitions are not observed for the prolate band in ^{184}Pb and the oblate band in ^{186}Pb and ^{188}Pb.

The unperturbed band-head state energies can be estimated using the variable moment of inertia (VMI) fits (see Section 2.3). The VMI fits for ^{186}Pb are shown in Figure 4.27. The states from 8^+ to 16^+ for the prolate band members and 8^+ to 14^+ for the oblate band members were assumed to represent pure states. The fit parameters are shown in Table 4.6. If it is assumed that the VMI fits produce pure states, it can be observed that the both prolate and oblate the 4^+, 2^+ and 0^+ states are pushed down in energy. This suggests a third set of excited 0^+, 2^+ and 4^+ lying slightly higher in energy, which could mix with both prolate and oblate configurations and cause perturbations in their level energies. Indeed, this is predicted *e.g.* by Duguet *et al.* [74]. Alternatively, this could show the limitation of the VMI fitting procedure. To solve this conundrum, further investigations of the other possible structures in ^{186}Pb are needed. The VMI fit gives 602 keV for the prolate 0^+ state, which is as close to 535 keV 0^+_2 state as it is for the 659 keV 0^+_3 state. Regardless of the selection of band member states, the VMI fit resulted is the oblate 0^+ state having higher energy than the prolate 0^+ state.

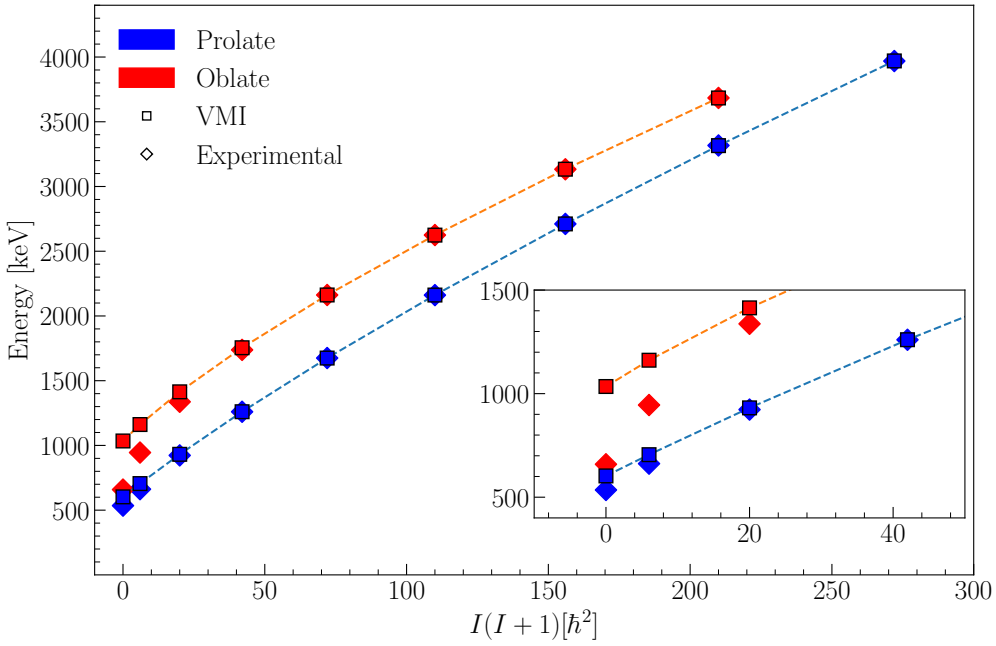

FIGURE 4.27 The VMI fits for ^{186}Pb prolate and oblate bands. The values and parameters are shown in Table 4.6. The inset shows a close-up of the low-spin states.

TABLE 4.6 Results of the VMI fits and the fit parameters J_0 and C for the prolate and oblate bands in ^{186}Pb.

	Prolate $J_0 = 0.028(1)\,(\mathrm{keV}^{-1})$ $C = 2.85(8) \times 10^6\,(\mathrm{keV}^3)$		Oblate $J_0 = 0.021(1)\,(\mathrm{keV}^{-1})$ $C = 1.38(6) \times 10^6\,(\mathrm{keV}^3)$	
State	Exp (keV)	VMI (keV)	Exp (keV)	VMI (keV)
0^+	535	602	659	1034
2^+	662	705	945	1161
4^+	923	931	1337	1414
6^+	1260	1260	1738	1754
8^+	1675*	1675	2162*	2625
10^+	2161*	2161	2624*	1034
12^+	2711*	2711	3133*[1]	3133
14^+	3317*	3316	3684*[1]	3683
16^+	3969*[1]	3970		

* used for fit

[1] taken from reference [9].

The assignments for the 0_2^+ and 0_3^+ states are reversed compared to the assignments proposed by Andreyev *et al.* [8]. Their conclusions were based on the following arguments: firstly, the level energy systematics of the 0^+ states associated with oblate shape, secondly, the extrapolation of the 0^+ level energy from high-spin states of yrast band and thirdly, the reduced α-decay widths obtained in the decay of ^{190}Po. The shape staggering between different isotopes [75] and the configuration mixing [76] in the neutron-deficient Pb ($N \approx 104$) region raises a question of validity using the level energy systematics as an argument for associating the 0_2^+ state with oblate shape. The extrapolation from high-spin states of yrast band does not provide stringent evidence to associate the 0_3^+ state with yrast band as it is seen with VMI fits in Figure 4.27. Based on the VMI fits, it could as well be part of the non-yrast band which was not observed when the reference [8] was published. The third argument was related to α-decay widths extracted in the decay of ^{190}Po but the ground state shape of ^{190}Po is not known. The theoretical predictions also conflicting, while beyond mean field calculations [77] predict the grounds state being predominantly oblate, the particle-core model calculation proposes a predominantly prolate shape [78, 79].

The new shape assignment in this work is supported by several theoretical calculations conducted for ^{186}Pb [3, 44, 74, 77, 80, 81, 82, 83, 84, 85]. Even though numerous theoretical calculations support this shape assignment, few theoretical calculation support the assignment by Andreyev *et al.* [8, 86, 87]. Further theoretical modelling and experimental studies are needed to understand the shape assignments of the excited 0^+ states in neutron-deficient Pb nuclei close to

mid-shell.

4.9.2 The $2_2^+ \rightarrow 2_1^+$ and $4_2^+ \rightarrow 4_1^+$ interband transitions

Based on the triangular rule (Equation 2.1), the interband transition multipolarities can be $E2$, $M1$ or $E0$. The conversion coefficients obtained for the interband transitions are larger than those for the $M1$ or $E2$ transitions, see Table 4.5, implying the presence of $E0$ transitions in the $2_2^+ \rightarrow 2_1^+$ and $4_2^+ \rightarrow 4_1^+$ interband transitions. The $E0$ transitions can only take place between initial and final state having the same spin and parity. As the yrast band is a $K = 0$ band and there are $E0$ transitions between the non-yrast and yrast band, the non-yrast band is also $K = 0$ band. Moreover, γ-ray angular distribution information supports the assignments of the non-yrast states having spin and parity assignments of 2_2^+, 4_2^+, 6_2^+ and 8_2^+ [10]. As the interband transitions take place between two $K = 0$ bands, the branch for $M1$ multipolarity is considered negligible.

The monopole strength $\rho^2(E0)$ holds interesting nuclear structure information. Even if the lifetime of the 2_2^+ state and the multipole mixing ratio $\delta^2(E2/M1)$ information for the $2_2^+ \rightarrow 2_1^+$ transition are lacking, the monopole transition strength can still be estimated. The reduced transition probability of $B(E2; 2_1^+ \rightarrow 0_1^+) = 6$ W.u. obtained in the ^{186}Pb lifetime measurement [23] and the reduced transition probability $B(E2; 2_2^+ \rightarrow 0_1^+) = 3.9$ W.u. measured in the ^{184}Hg Coulex experiment [24]. The aforementioned transitions are expected to take place between different configurations (shapes), which is reflected in a relatively low$B(E2)$ value and therefore they can be used as rough estimate for the $B(E2; 2_2^+ \rightarrow 0_1^+)$ value. Consequently, using an estimated reduced transition probability of $B(E2; 2_2^+ \rightarrow 0_1^+) = 5$ W. u., assuming that the $M1$ transition intensity is negligible and using Equations 2.11 and 2.12 , one obtains the monopole strength value of $\rho^2(2_2^+ \rightarrow 2_1^+) = 100(60) \times 10^{-3}$.

With the two-level mixing model, it is possible to determine the amount of mixing needed to explain the monopole strength value. The two-level mixing model is described by the equation

$$\rho^2(E0) = \left(\frac{3}{4\pi}Z\right)^2 a^2(1-a^2)^2(\beta_{2,1}^2 - \beta_{2,2}^2)^2, \tag{4.12}$$

where Z is the atomic number, a are the mixing amplitudes and $\beta_{2,i}$ is the quadrupole deformation parameter for $i = 1$ yrast and $i = 2$ non-yrast states*. The average quadrupole deformation parameter β for the yrast band states, based on the life time measurement of ^{186}Pb and ^{188}Pb [23], was determined to be $|\beta_{2,1}| = 0.29$. Concerning the non-yrast band, that has been associated with an oblate shape, a

*The derivation of equation is shown in Section 2.2.3

$|\beta_{2,2}|$ value of 0.17 represent typical quadrupole deformation in this region [23]. Using these values, the mixing amplitude of $a^2 = 0.9$ was extracted.

In Figure 4.28, monopole strength values for the $2_2^+ \rightarrow 2_1^+$ transition are shown with different assumptions of $B(E2; 2_2^+ \rightarrow 0_1^+)$ and $\delta^2(E2/M1)$ values. The monopole strength varies from 2×10^{-3} to 190×10^{-3}. The monopole strength $\rho^2(E0)$ is directly proportional to the reduced transition strength $B(E2)$ values as seen in the Figure 4.28 and Equation 2.11. From the largest to the lowest $\rho^2(2_2^+ \rightarrow 2_1^+)$ values, the mixing amplitude a^2 between from $0.8 - 0.99$ as extracted using Equation 4.12. This indicates weak mixing between the 2_2^+ and 2_1^+ states.

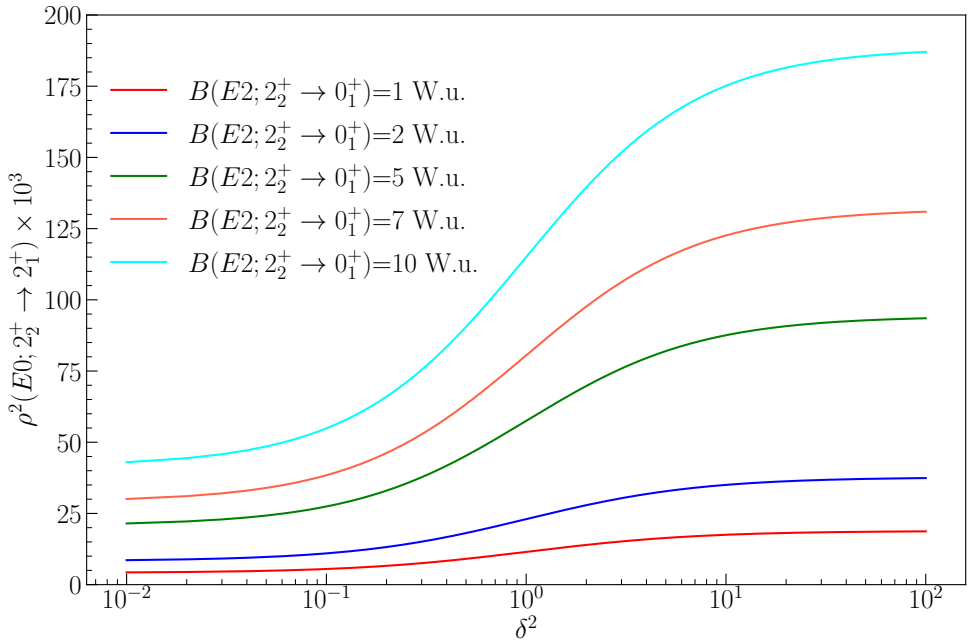

FIGURE 4.28 The lower limit of the monopole strength $\rho^2(2_2^+ \rightarrow 2_1^+)$ as a function of multipole mixing $\delta^2(E2/M1)$ for the $2_2^+ \rightarrow 2_1^+$ transition. The monopole strength was calculated using equations 2.11 and 2.12 with different estimates for the reduced transition probability $B(E2; 2_2 \rightarrow 0_1^+)$. Since the γ-ray intensity of the $2_2^+ \rightarrow 2_1^+$ transition could not be determined, the calculated values of $\rho^2(2_2^+ \rightarrow 2_1^+)$ represent lower limits.

The lower limit for the total conversion coefficient α_{tot} is plotted in Figure 4.29 for the $2_2^+ \rightarrow 2_1^+$ transition with different $\delta^2(E2/M1)$ multipole mixing ratios. The α_{tot} values was calculated using Equation 2.17. These values varies from 1.04 to 1.07 depending on the multipole mixing ratio $\delta^2(E2/M1)$ as demonstrated in Figure 4.29.

Similarly to the $2_2^+ \rightarrow 2_1^+$ transition, the monopole strength for the $4_2^+ \rightarrow 4_1^+$ transition can be estimated. By assuming $B(E2; 4_2^+ \rightarrow 2_2^+) = 100$ W.u., which

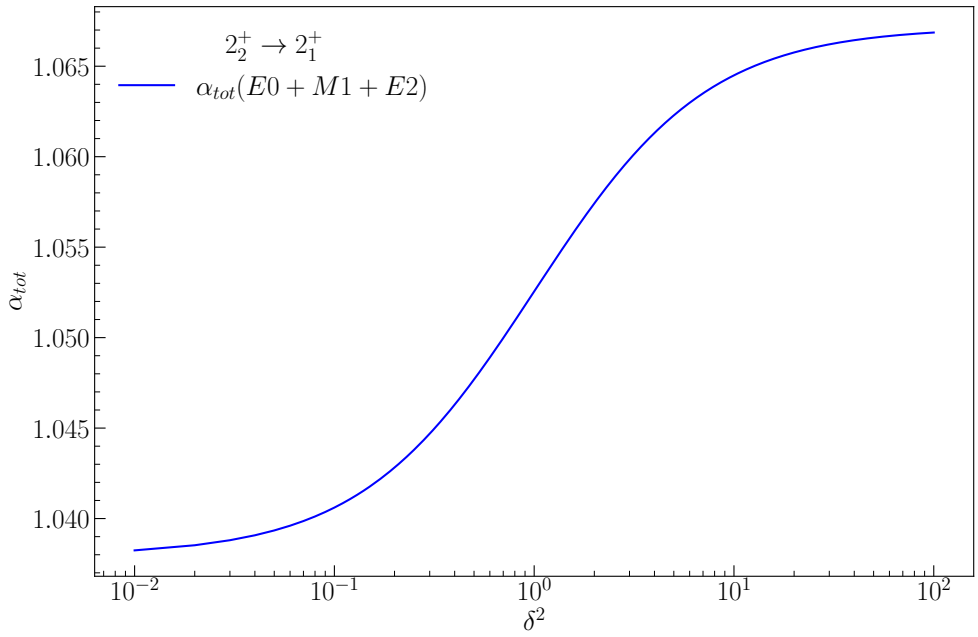

FIGURE 4.29 Total conversion coefficient for the $2_2^+ \rightarrow 2_1^+$ transition as a function of multipole mixing ratio $\delta^2(E2/M1)$.

is a typical value for an oblate in-band transitions (see *e.g.* reference [23]), and neglible $M1$ transition intensity, Equations 2.11 and 2.12 were used to calculate the monopole strength $\rho^2(E0)$ for the $4_2^+ \rightarrow 4_1^+$ transition. Accordingly, a value of $\rho^2(4_2^+ \rightarrow 4_1^+) = 40(30) \times 10^{-3}$ for the monopole strength was obtained. The dependence of the $4_2^+ \rightarrow 4_1^+$ transition monopole strength to the $\delta(E2/M1)$ multipole mixing ratio and with different $B(E2; 4_2^+ \rightarrow 2_2^+)$ values is shown in Figure 4.30. Based on the two level mixing model and the same assumption as in the $2_2^+ \rightarrow 2_1^+$ transition for quadrupole deformation parameters β, and assuming $B(E2; 4_2^+ \rightarrow 2_2^+) = 100$ W.u, the mixing amplitude a^2 gets a value of 0.96. Again, $\rho^2(4_2^+ \rightarrow 4_1^+)$ values plotted in Figure 4.30 produces small mixing amplitude a^2, which varies between 0.92–0.99. The small mixing between the 4_2^+ and 4_1^+states of yrast and non-yrast state has also been derived from the results of the lifetime measurements by Grahn *et al.* [23], where the 4_1^+ state showed to be rather pure member of yrast band.

The total conversion coefficient α_{tot} was also evaluated for the $4_2^+ \rightarrow 4_1^+$ transition with different multipole mixing ratio values $\delta^2(E2/M1)$, see Figure 4.31. The total conversion coefficient does not depend significantly on the $\delta(E2/M1)$ multipole mixing ratio.

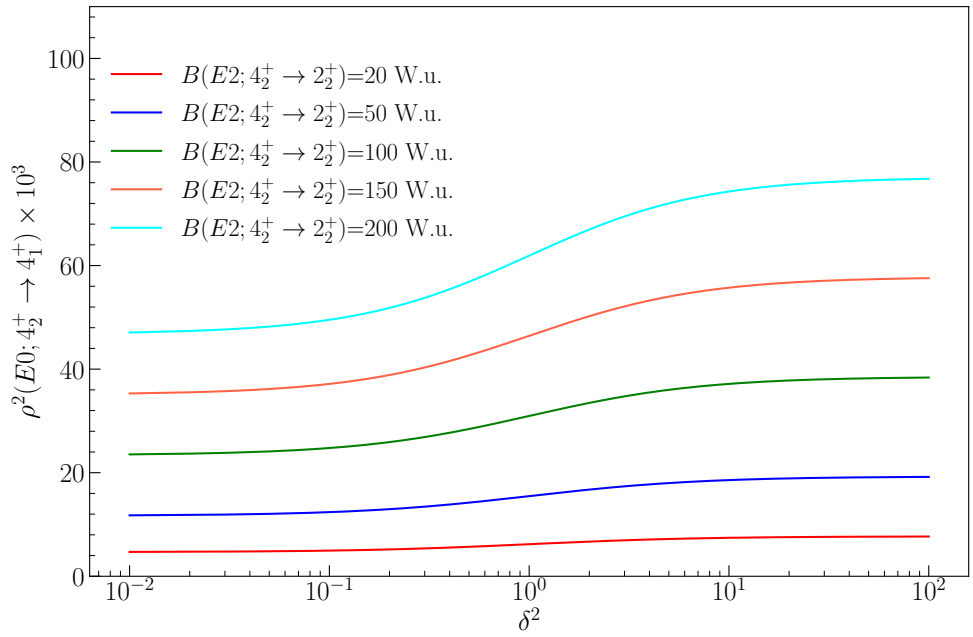

FIGURE 4.30 The monopole strength $\rho^2(4_2^+ \to 4_1^+)$ as a function of multipole mixing $\delta^2(E2/M1)$ for the $4_2^+ \to 4_1^+$ transition. The monopole strength was calculated using equations 2.11 and 2.12 with different estimates for the reduced transition probability $B(E2;4_2^+ \to 2_2^+)$.

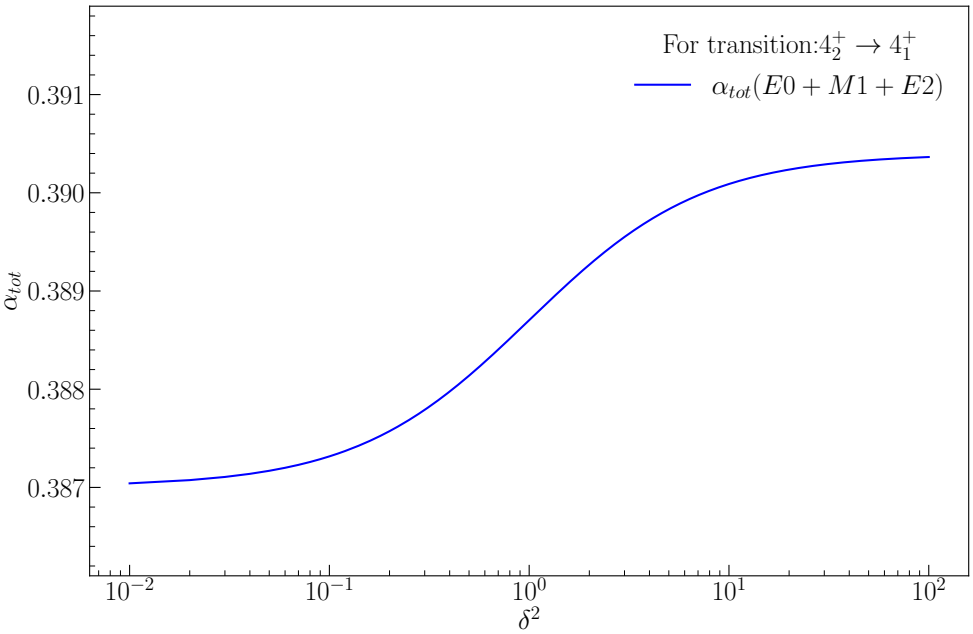

FIGURE 4.31 Total conversion coefficient for $4_2^+ \to 4_1^+$ as a function of multipole mixing $\delta^2(E2/M1)$ ratio according to Equation 2.17.

4.10 Outlook

The study of neutron-deficient ^{186}Pb employing combined in-beam γ-ray and conversion electron spectroscopy increased the knowledge about the low-lying structures in this nucleus. Even though the results are valuable for the nuclear structure community, there are still unanswered questions waiting for experimental input, such as:

- Experimental confirmation for small $\delta^2(E2/M1)$ multipole mixing ratios of the $2_2^+ \rightarrow 2_1^+$ and the $4_2^+ \rightarrow 4_1^+$ interband transitions.
- Gather lifetime information for the excited 0^+ states.
- Obtain lifetime information for the non-yrast states.
- Inspect $B(E2)$ values of interband transitions to confirm the small configuration mixing between prolate and oblate configuration.
- Observe the feeding of the 0_3^+ state and confirm that it is belonging to the non-yrast band.

The complementary experimental data is required to answer these questions.

Coulex experiment might allow us to measure the $B(E2)$ values for interband transitions, determine the $E2/M1$ multipole mixing ratio and infer the feeding of the 0_3^+ state. For example, the Coulex experiments can be performed with the SPEDE spectrometer [88] in conjuction with MINIBALL spectrometer [89] to probe both γ rays and conversion electrons at the HIE-ISOLDE. Lifetimes of the excited 0^+ states could be measured by using the recoil-shadow method [90].

Several in-beam experiments on ^{182}Pb [91], ^{184}Pb [92], ^{188}Pb [93, 94] and ^{190}Pb [95] nuclei have been performed to shed light on the level energy systematics. The current level energy systematics is missing information on oblate structure beyond the neutron $N = 104$ midshell and the 0^+ state of prolate bands for ^{188}Pb and ^{190}Pb. Several attempts to measure the non-yrast states of ^{184}Pb have been made, albeit without great success. A germanium detector array with much higher efficiency or much longer beam times, would be needed in order to gain sensitivity to probe the non-yrast structures of ^{184}Pb. Regarding ^{188}Pb and ^{190}Pb, detailed γ-spectroscopic studies have been published in Ref. [93, 94, 95]. More recently, new data from combined in-beam γ-ray and electron spectroscopy with the SAGE spectrometer have been obtained. Systematic information on the feeding of the excited 0^+ states and the $E0$ $I^+ \rightarrow I^+$ interband transitions are needed to improve our understanding of underlying forces striving interesting phenomena in this region.

5 INSTRUMENTATION DEVELOPMENT AND CHARACTERISATION

5.1 JUROGAM 3 spectrometer

The JUROGAM 3 spectrometer [11] is a germanium-detector array located in the ACC-LAB. The JUROGAM 3 array is used to detect the emitted γ-rays from the excited nuclei produced mainly via fusion-evaporation reaction. Important properties for in-beam spectrometers are good energy resolution, high granularity and good timing. JUROGAM 3 has the same detector configuration as its predecessor JUROGAM II. The difference between these two spectrometers is that the JUROGAM 3 germanium-detector array can be moved between the MARA and the RITU separator without switching off the bias voltages from detectors. The RITU separator was originally designed to perform in the heavy ($Z \geq 82$) region utilising asymmetric reactions while the MARA separator is intended to be more sensitive for lighter nuclei utilising the symmetric or inverse reactions [34, 96, 97]. Using the germanium array in conjunction with the MARA and RITU separator allows for in-beam spectroscopy of a wider range of nuclei than before. During 2019-2022, more than 5400 hours of beam time was used for experiments employing JUROGAM 3.

The benefit of a movable germanium detector array is the possibility to continue experiments without breaks of several months while transporting the array between separators. In fusion-evaporation reaction, germanium detectors are exposed to neutrons emitted in reactions. These neutrons dislocate atoms in the germanium crystal lattice which is manifested as a low-energy tail for full-energy peaks after unbiasing the detector [98]. The damaged crystal structure can be restored by annealing the detector, which takes several days for one detector. Unbiasing the whole array would mean several months of annealing work. If one needs

to move array, it should be done without switching off biases. The array, liquid nitrogen control system, HV-power supplies, preamplifier power supplies and Single-ended to Differential cards (SoD) are all attached to a movable gantry. The gantry and whole setup are shown in Figure 5.1.

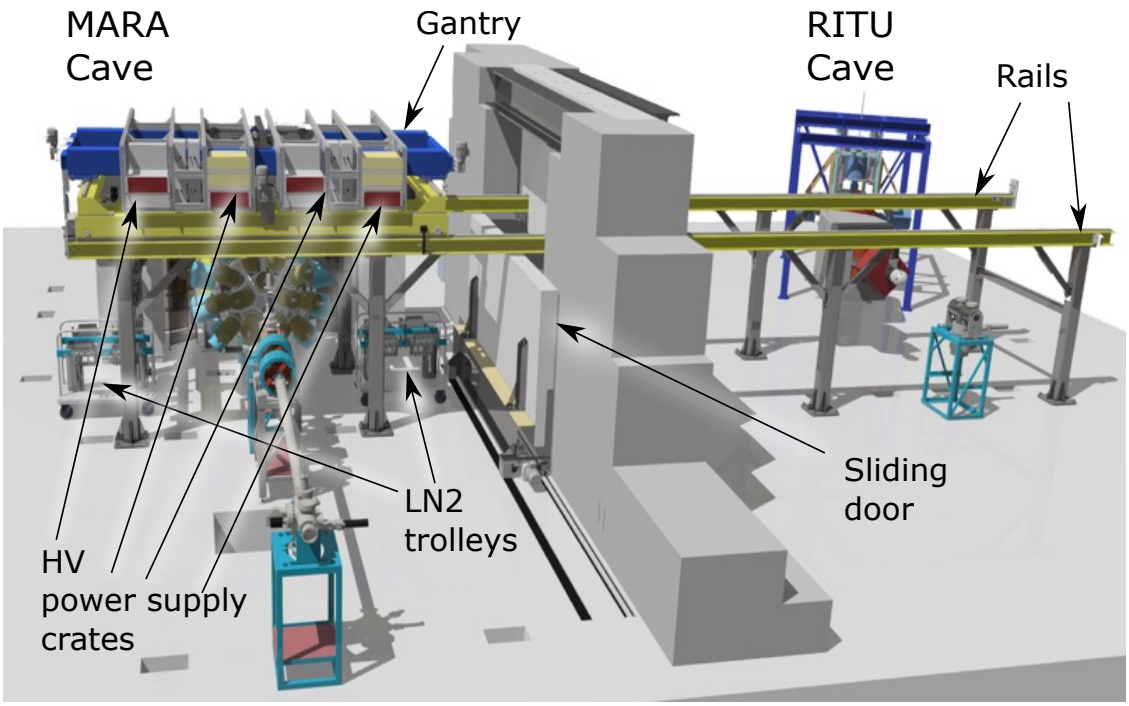

FIGURE 5.1 Schematic drawing of the JUROGAM 3 spectrometer and its transportation system between MARA and RITU cave. JUROGAM 3 is situated in the MARA cave in the drawing. The sliding door between MARA and RITU caves allows for working in one of the caves while running an experiment in the other. Essential parts of JUROGAM 3 are labelled.

The JUROGAM 3 array consists of 24 composite Clover detectors [99] and 15 tapered single-crystal Phase 1 [39] or GASP [40] detectors, summing up to 111 crystals in the whole array. Detectors are installed in four rings so that five tapered detectors are at 157.6° (Ring 1) and ten at 133.6° (Ring2) angle with respect to the beam axis. The last two rings are equipped with Clover detectors at 104.5° (Ring3) and at 75.5° (Ring 4) angle with respect to beam axis. The schematic drawing of one hemisphere of the JUROGAM 3 array is shown in Figure 5.2.

Each detector is covered with bismuth germanate (BGO) shields to veto γ rays that did not deposit full energy in the germanium crystal. Heavy-metal collimators are installed between the target and the BGO shields to reduce direct hits of γ rays in the BGO shields. In studies of nuclei with high atomic numbers, it is advisable to use Cu and Sn absorbers reduce low-energy X-ray yield arising from different reactions inside the target. Average thicknesses for a Sn absorbers on Clover and

tapered detectors are 0.26 mm and 0.24 mm, respectively, while for Cu absorbers these numbers are 0.63 mm and 0.5 mm, respectively.

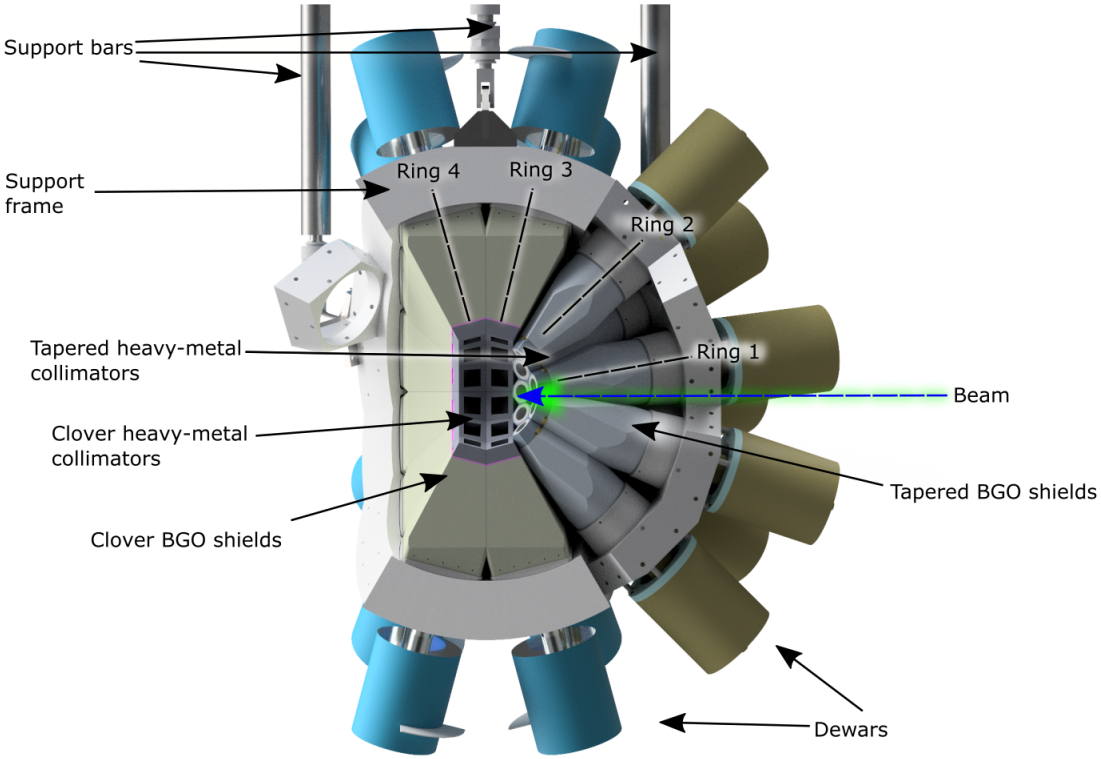

FIGURE 5.2 Schematic drawing of one hemisphere of the JUROGAM 3 array. The essential parts of the array are labelled. Each ring is labelled and illustrated with a dashed line. The heavy-ion beam direction from the K-130 accelerator is shown with a blue arrow. The target chamber would be situated at the centre of the array.

The signals from the preamplifiers of the germanium detectors are fed to the SoD cards, which convert them to differential signals. Differential signals are sent through a 30-m-long twisted pair ribbon cables to the Differential to Single-ended cards (DoS), which convert the differential signal back to single-ended signals. Differential signals are less prone for pick-up noise when transporting signals over long distances. From the DoS cards, the single-ended signals are then fed to LYRTECH/NUTAQ digitiser cards with 14-bit accuracy and assigned with time-stamps from 100-MHz clock. The block diagram of the JUROGAM 3 signal chain is shown in Figure 5.3. A similar signal chain was developed for the MARA focal plane setup.

Four CAEN SY5527 HV power supplies are used for applying the HV for both the germanium detectors and the BGO shields. The GECO2020 control interface allows to set different high voltage values, leakage current limits, the ramp-up/down

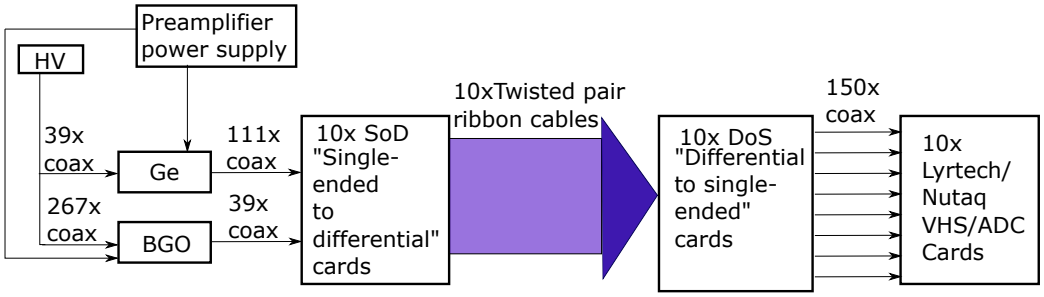

FIGURE 5.3 Block diagram of the signal chain of the JUROGAM 3 germanium detectors and BGO shields.

rates, and HV limits to each detector. The bias shutdown signals are also monitored ensuring powering off detectors in case of accidental warm up.

The energy and efficiency calibration of the JUROGAM 3 array are typically performed using ^{133}Ba and ^{152}Eu radioactive sources to guarantee a broad energy range from 81 keV to 1408 keV [52]. The absolute efficiency can be determined using a ^{60}Co source [100].

5.1.1 Add-back factor

The Clover detectors can be used in the add-back mode, where a γ-ray detected in one crystal opens an event window to sum all γ-ray energies that occurred in neighbouring crystals together within the time limit set by the user. In this thesis, the add-back mode was applied, and the event window width was selected to be 200 ns. The add-back mode is beneficial as it allows to retrieve the Compton scattered γ-rays between two, three or four crystals in the same Clover detector improving the detection efficiency.

The add-back factor is quantity to describe the effect of add-back mode to detection efficiency

$$\text{Add-back factor} = \frac{N_{AB}}{N_{Sum}}, \tag{5.1}$$

where N_{AB} is the number of counts in full-energy peak detected in add-back mode and N_{Sum} is the sum of counts from each individual crystals for same the full-energy peak. The add-back factor has been originally reported by Duchêne *et al.* [99]. The average add-back factor was determined to be 1.49(2) at 1332 keV in this work and reported in reference [11]. The add-back factor in energy region 81 keV to 1408 keV was determined with the ^{133}Ba and ^{152}Eu sources, as it is shown in Figure 5.4.

The add-back mode improves the photopeak detection efficiency and peak-to-total values, but has a minor negative effect on the full-width at half maximum

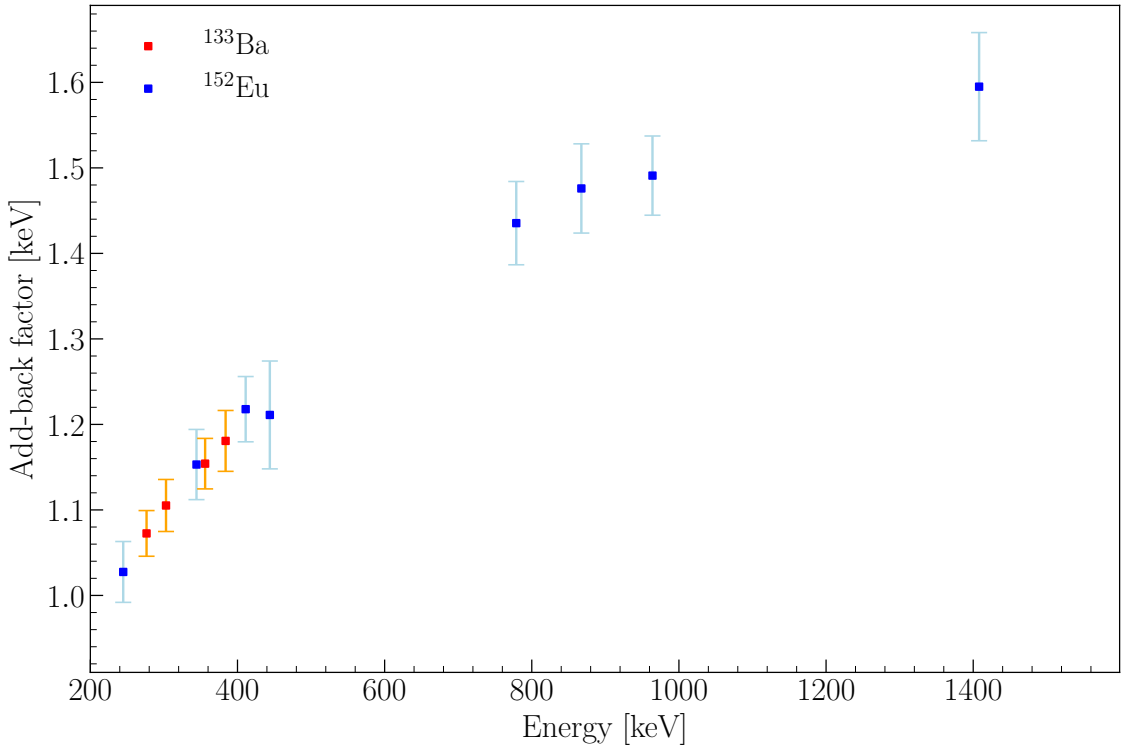

FIGURE 5.4 The average add-back factor of Clover detectors. The origins of full-energy peaks from ^{133}Ba (red) and ^{152}Eu (blue) are shown in figure.

(FWHM) values, see table 5.1. Benefits of add-back mode is demonstrated in Figure 5.5 which shows reduction of background up to 400 keV and more counts in full-energy peaks from 300 keV to higher energies.

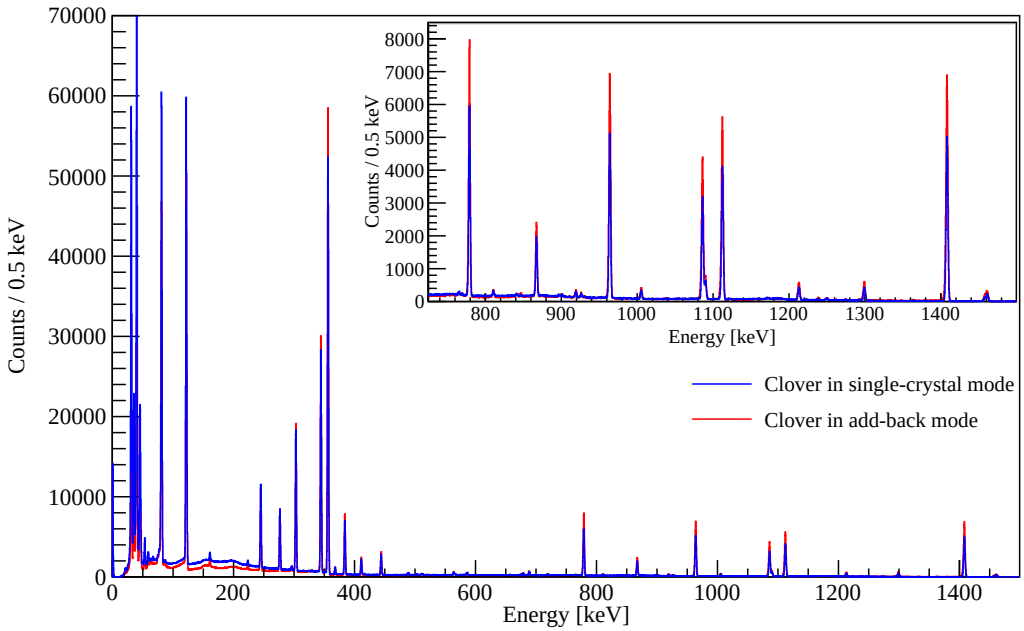

FIGURE 5.5 γ-ray energy spectrum of Clover detectors in add-back mode (red) and single-crystal mode (blue). Inset shows a close-up of higher energies.

5.1.2 The energy resolution of the JUROGAM 3 array and germanium detectors

The average FWHM values were determined for single Clover crystal, Clover detectors in add-back mode and tapered germanium detectors using Eu and Ba sources. The detectors were mounted in the JUROGAM 3 array and the BGO veto was used. The obtained FWHM values are listed in Table 5.1 for 81 keV, 356 keV, 779 keV and 1408 keV, and plotted in Figure 5.6. The energy resolutions of Clover crystals has deteriorated from their original values reported in Ref. [99]. This can be explained by defects in crystal structure arising *e.g.* from neutron damages.

Similarly, the FWHM values of the JUROGAM 3 array were determined using the same aforementioned Clover and tapered detectors in a single-crystal mode and add-back mode.

TABLE 5.1 Average FWHM energy resolution values of JUROGAM 3 detectors in add-back and single-crystal mode.

	FWHM resolution at			
	81 keV	356 keV	779 keV	1408 keV
Tapered detectors	2.28(47)	2.25(42)	2.56(41)	3.07(43)
Clover detectors[1]	1.83(19)	1.92(17)	2.26(18)	2.76(21)
Clover detectors[2]	1.90(13)	2.14(18)	2.60(19)	3.17(23)
Full array[1]	1.98(26)	2.05(24)	2.39(30)	2.87(21)
Full array[2]	1.98(17)	2.18(26)	2.78(26)	3.37(30)

[1] Individual Clover crystals

[2] Employing the add-back mode for the Clover detectors

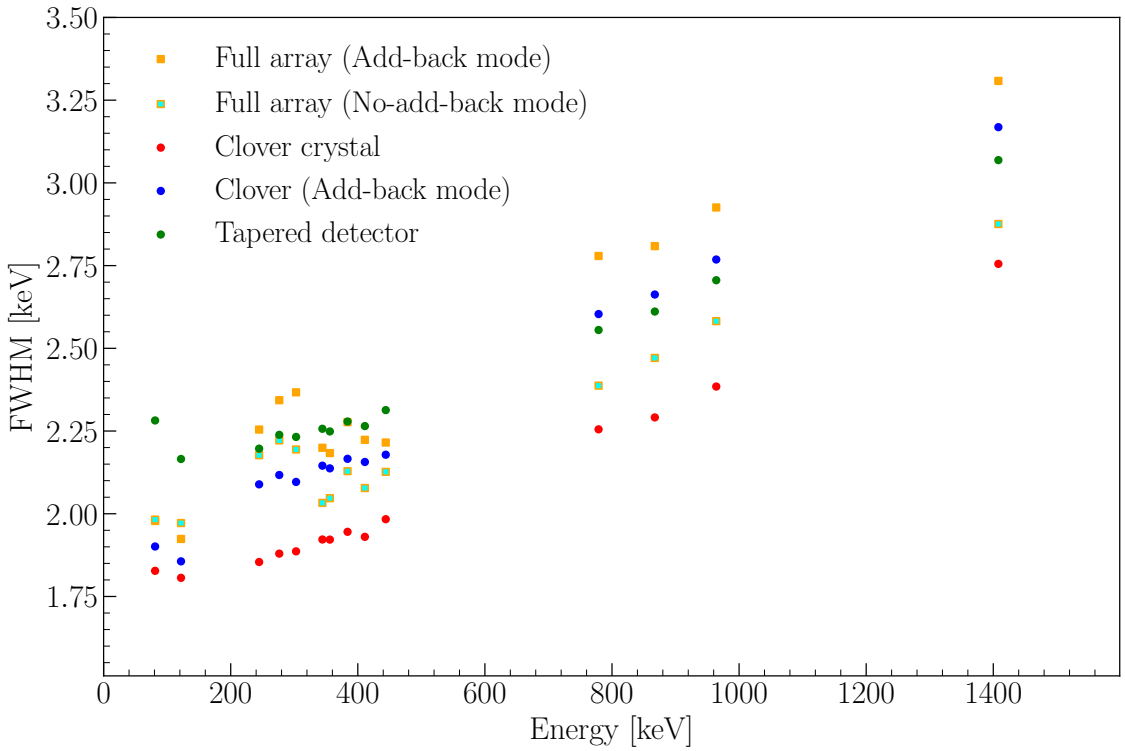

FIGURE 5.6 The average FWHM energy resolution values of the JUROGAM 3 detectors measured in-situ using the ^{133}Ba and ^{152}Eu calibration sources. Red circles are for Clover single crystal, blue circles for Clover in add-back mode, the green circles for tapered, solid yellow squares for the JUROGAM 3 array with Clovers in add-back mode and yellow-green squares for the JUROGAM 3 array with Clovers in single-crystal mode.

5.1.3 Peak-to-total

In γ-ray energy spectra obtained with germanium detectors, a considerable fraction of background is induced by Compton scattered γ-rays which escape from the

crystal depositing only part of their energy. The peak-to-total value is a quantified way to express the detector performance. In this thesis, the peak-to-total values were obtained using ^{60}Co calibration source and equation

$$P/T = \frac{N_{1173} + N_{1332}}{B_{100-1350}}, \tag{5.2}$$

where N_{1173} and N_{1332} are the number of counts obtained for peaks at 1173 keV and 1332 keV and $B_{100-1350}$ is the counts between 100 keV and 1350 keV. The peak-to-total values, obtained without employing the BGO shields, are $P/T \approx 0.24$ for the tapered detectors , $P/T \approx 0.26$ for the Clover detectors in add-back mode and $P/T \approx 0.14$ for the Clover detectors in the single-crystal mode.

The Compton-suppression shields can be used to veto events of scattered γ rays in order to improve the peak-to-total value of the germanium detector. In the JUROGAM 3 array, the sensitive detection volume of the Compton-suppression shields consist of BGO material, which has a high γ-ray absorption efficiency. The benefits of the BGO veto are demonstrated in Table 5.2. The outputs of photomultipliers coupled to the BGO in the shield were daisy-chained and fed into the LYRTECH/NUTAQ cards.

TABLE 5.2 The peak-to-total values obtained for the JUROGAM 3 detectors with and without Compton suppression (BGO veto) together with previously reported values [39, 99]

	Peak-To-Total			
	BGO veto (*)	Without BGO veto(*)	BGO veto [39, 99]	Without BGO veto[39, 99]
Array	0.47(1)	0.23(1)		
Tapered	0.47(1)	0.24(1)	0.54-0.58	0.25
Clover (add-back)	0.47(1)	0.26(1)	0.55	0.30
Clover (single-crystal)	0.24(1)	0.14(1)		

* This work

The position information of the scattered γ rays in the BGO shields are lost due to the daisy-chaining. Position information would allow for better correlation of scattered γ rays between germanium-BGO material and consequently result in better P/T. The energy spectrum obtained with the daisy-chained BGO shield is shown in Figure 5.7. Veto events have been marked in the event data word. The width of the coincidence window between germanium and BGO shield signals was set to 600 ns.

The obtained peak-to-total values for Clovers and tapered detector are slightly lower than reported in Ref. [39, 99], see Table 5.2. The reason for poorer peak-

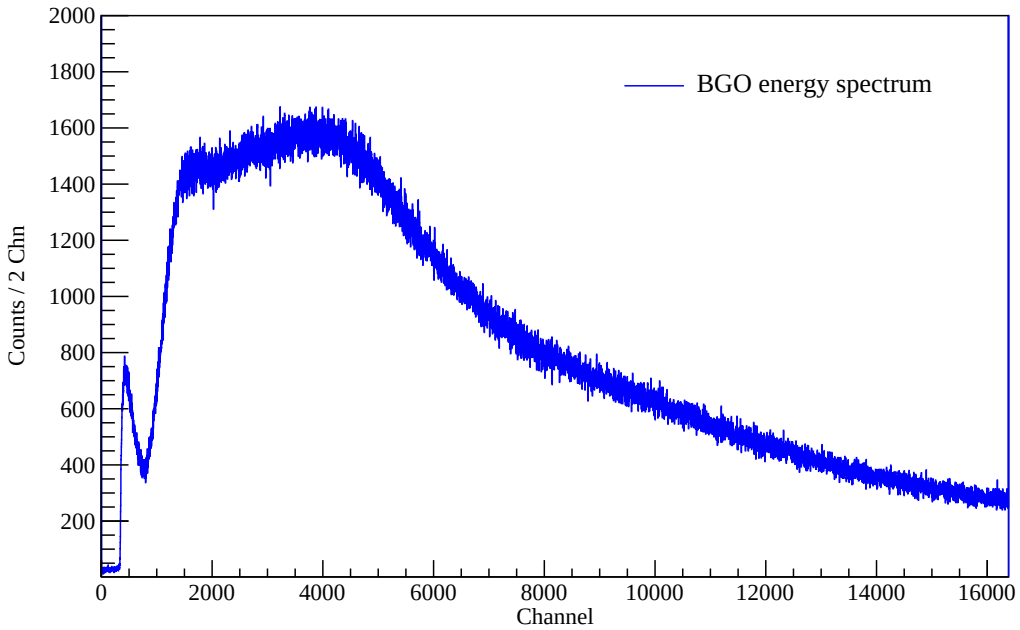

FIGURE 5.7 The daisy-chained BGO-shield energy spectrum. The spectrum shows mainly γ-ray events from ^{60}Co source at the target position that are Compton scattered in the germanium crystal.

to-total values can be related to the degradation of optical coupling between the scintillator and photomultiplier tube.

5.1.4 The photopeak detection efficiency

The photopeak detection efficiency of JUROGAM 3 was determined in two parts. First, the relative photopeak detection efficiency was measured with ^{152}Eu and ^{131}Ba sources that covers energy region from 81 keV to 1408 keV. Second, the absolute photopeak detection efficiency was determined using ^{60}Co source and the sum-peak method, see section 5.1.5. By combining these two results, the absolute detection efficiency covering energy region from 81 keV to 1408 keV could be determined independent of calibration source activities.

The relative efficiency can be determined by equations

$$\epsilon_{rel}(E) = \mathcal{N}\frac{N_{det}}{I_\gamma}, \tag{5.3}$$

where $\mathcal{N}$ is a normalisation factor for two different sources, N_{det} is the number of detected γ rays in the full-energy peak and I_γ is the γ-ray transition intensity. As the 356 keV γ rays from ^{133}Ba decay and 344 keV γ rays from ^{152}Eu decay have similar efficiency, these peaks were used to determine the normalisation factor $\mathcal{N} = \frac{N_{356}I_{344}}{I_{356}N_{344}} = 0.91$ for γ rays from the ^{133}Ba source.

Determination of the absolute efficiency of the γ-detector was performed by using ^{60}Co and sum-peak method

$$\epsilon_{abs}(E) = \mathcal{N}\epsilon_{rel}(E) = \frac{\epsilon_{abs}(1332)}{\epsilon_{rel}(1332)}\epsilon_{rel}(E). \tag{5.4}$$

The absolute efficiency curves extracted for JUROGAM 3 with and without the JYTube* charged-particle veto detector are shown in Figure 5.8. Additionally, the absolute efficiency of the partial JUROGAM 3 array used as a germanium array for the SAGE spectrometer during the 2021 experimental campaign is included in Figure 5.8.

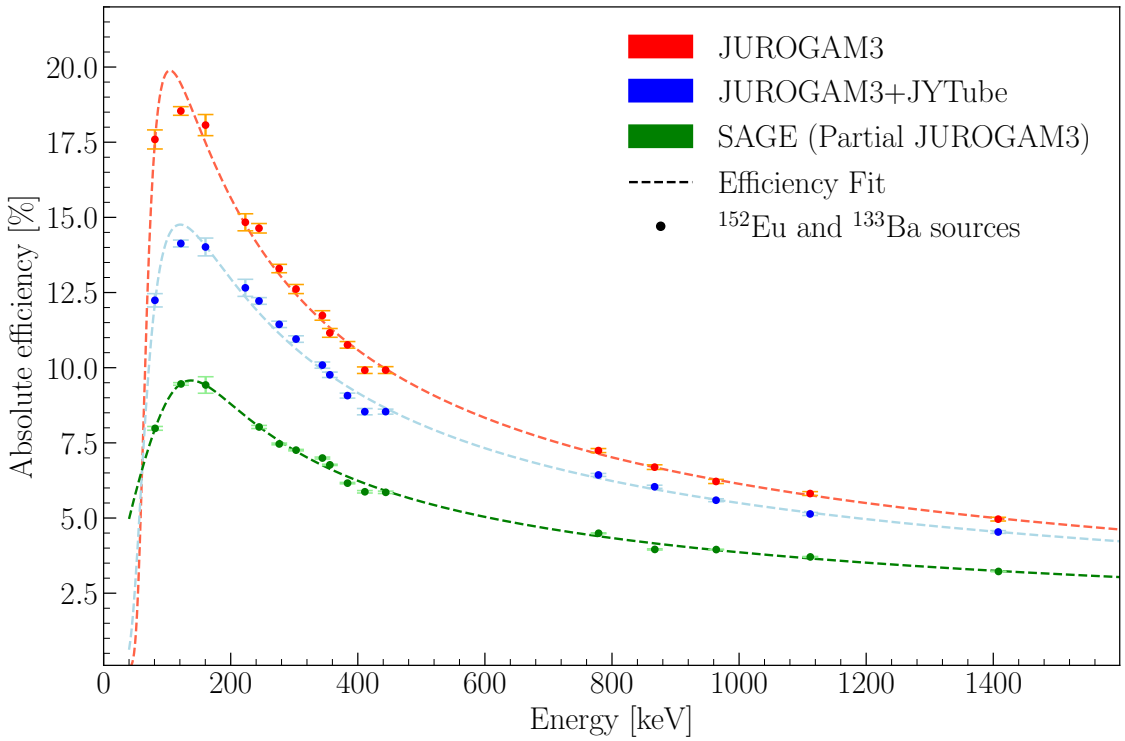

FIGURE 5.8 The absolute γ-ray photopeak detection efficiency of JUROGAM 3. The filled circles represents the absolute efficiency obtained with ^{133}Ba and ^{152}Eu calibration sources. The dashed lines represents absolute efficiency obtained with Equation 4.1. The efficiency of the JUROGAM 3 array is coloured with red, efficiency of JUROGAM 3 with JYTube is coloured with blue and efficiency of germanium detector array of SAGE is coloured with green.

*JYTube is a charge-particle veto detector surrounding the target position, allowing to probe of different neutron-evaporation channels.

5.1.5 Sum-peak method

The sum-peak method can be used for determination of the absolute detection efficiency without relying on the activity information of the source [100, 101]. This is possible with γ rays of cascading transitions when lifetime of the connecting state is so short that both γ rays are deposited in the germanium crystal within the event shaping time. Consequently, the signal registered by the detector corresponds to the sum of both γ-ray energies. For example, ^{60}Co calibration sources are suitable for this purpose and have been used in the present work. The ^{60}Co decays to ^{60}Ni feeding the 4^+ state with 99.88% branching ratio [102] to a state which de-excites via 1173 keV γ-ray transition to the 2^+ state, which subsequently de-excites to the ground state via the 1332 keV γ-ray transition [103].

The sum-peak method can be formulated as follows:

$$\epsilon(1173) = \frac{N_{1173}}{N_{decays}} \tag{5.5}$$

$$\epsilon(1332) = \frac{N_{1332}}{N_{decays}} \tag{5.6}$$

$$\epsilon(1173)\epsilon(1332) = \frac{N_{Sum}}{W(0)N_{decays}}, \tag{5.7}$$

where N_{1173} is the number of detected1173 keV γ rays, N_{1332} is the number of detected 1332 keV γ rays, $W(0)$ is the angular correlation at angle 0° of two γ rays from ^{60}Ni, N_{sum} is the number of coincidence events in one detector, $\epsilon(E)$ is the absolute detection efficiency at energy E and N_{decays} is the number of decays of the ^{60}Co source which are feeding the 4^+ state in ^{60}Ni. Other de-excitations paths from the 4^+ state to the ground state and ^{60}Co decays to the 2^+ state in ^{60}Ni can be considered negligible.

Angular correlation correction has to be taken into account when calculating the product of 1173 keV and 1332 keV efficiencies. The angular correlation can be described with the following equation

$$W(\theta) = 1 + A_2P_2(cos(\theta)) + A_4P_4(cos(\theta)), \tag{5.8}$$

where A_2 and A_4 are parameters depending on the transition multipolarity and P_n is the n-th Legendre polynomial. Due to the distance between the source and the detector and size of the detector itself, the value for $\theta \approx 0^\circ$ can be assumed. Since values for A_2 and A_4 in this case are 0.10204 and 0.00907, respectively [104], the coefficient for the angular correlation for emitted γ-rays after ^{60}Co decay becomes $W(0^\circ) \approx 1.111$.

The detection efficiency at 1332keV can be written as:

$$\epsilon(1332) = \frac{N_{Sum}}{1.111 \times N_{1173}}. \tag{5.9}$$

If the sum-peak method is used for Clovers in add-back mode, it is needed to sum all events from all four crystals.

As two consecutive γ rays hit the same detector, the data acquisition system may raise pile-up flag for these events. However, this is not the case for transitions following the ^{60}Co decay as the lifetime of the 2^+ state in ^{60}Ni is $\tau = 1.3\,\mathrm{ps}$ which is shorter than one clock tick (10 ns) of the data acquisition system. Indeed, less than 1% of the sum-peak events were found to be marked as pile-up events.

5.1.6 False pile-up events

The pile-up events occur when triggering signals are detected while the previous signal is under process. These types of events can be discarded or marked in the Lyrtech/NUTAQ digitiser cards. The pile-up rejection allows for discarding events which might cause low-energy tailing in the Gaussian shaped peaks. Normally, pile-up events are discarded from the data stream , but for some detectors, this is not advisable due to the false pile-up events occurring.

In some cases, false pile-up events can occur. A typical germanium detector signal has a fast risetime of around 200 ns that causes a trigger in the DAQ, and exponential decay with time constant of around 50 μs. If the decay of the signal is not smooth, but has under/overshoot or oscillations, they can cause additional trigger which causes a pile-up mark. As that is not a real pile-up event, but something arising from distorted signal shape, it is considered as a false pile-up event. Examples of signals producing false pile-up events are shown in Figure 5.9.

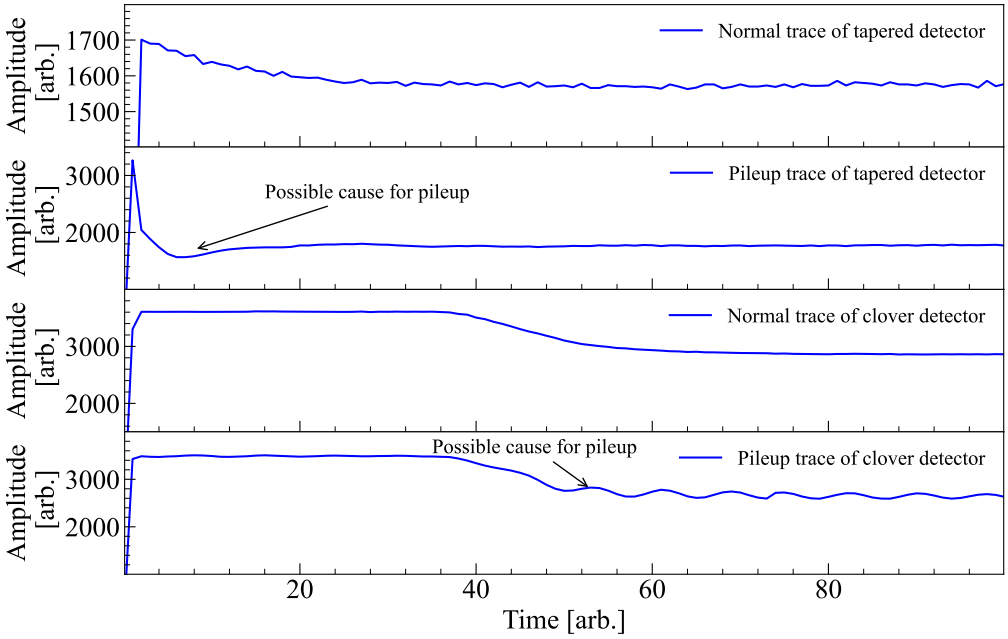

FIGURE 5.9 Few examples of signals from different germanium detector channels. First panel: Trace from a tapered detector. Second panel: Trace from tapered detector introducing false pile up. Third panel: Trace from a Clover detector signal. Fourth panel: Traces from a Clover detector introducing false pile up. Possible causes for false pile ups are labelled and indicated by arrows.

False pile-up events can substantially decrease the amount of "good" events, as demonstrated in Figure 5.10 and Figure 5.11. An energy spectrum obtained with

one Clover germanium detector channel is shown in Figure 5.10 (top), indicating negligible amount of pile-up events. In the same Clover detector, there is a channel which creates many false pile-up events in the high-energy region (700–1410 keV), as shown in Fig 5.11. Naturally, if pile-up rejection is applied in the latter case, considerable amount of data is lost.

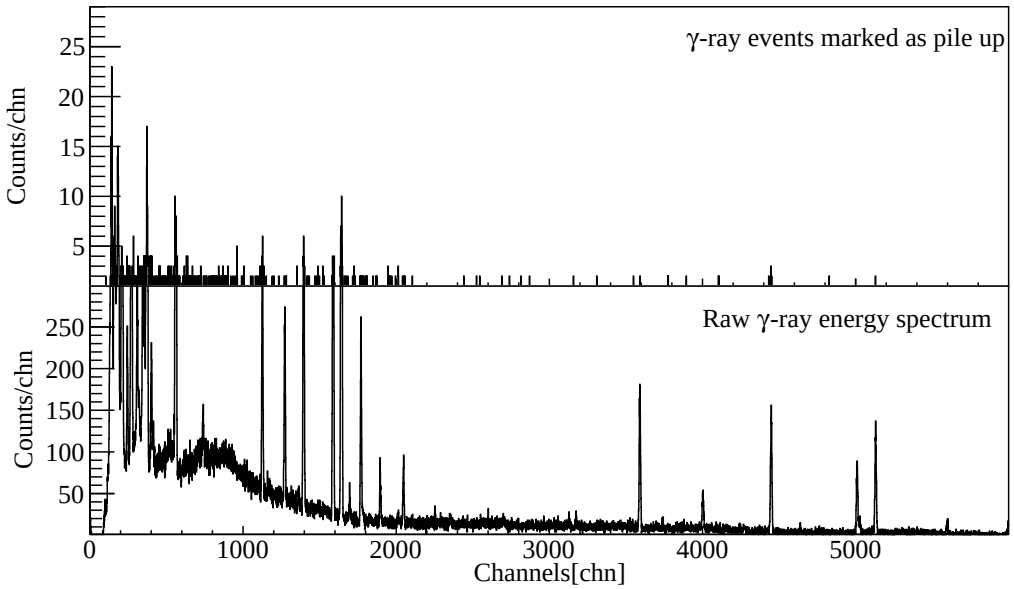

FIGURE 5.10 γ-ray energy spectrum demonstrating pile-up (top) and raw events (bottom).

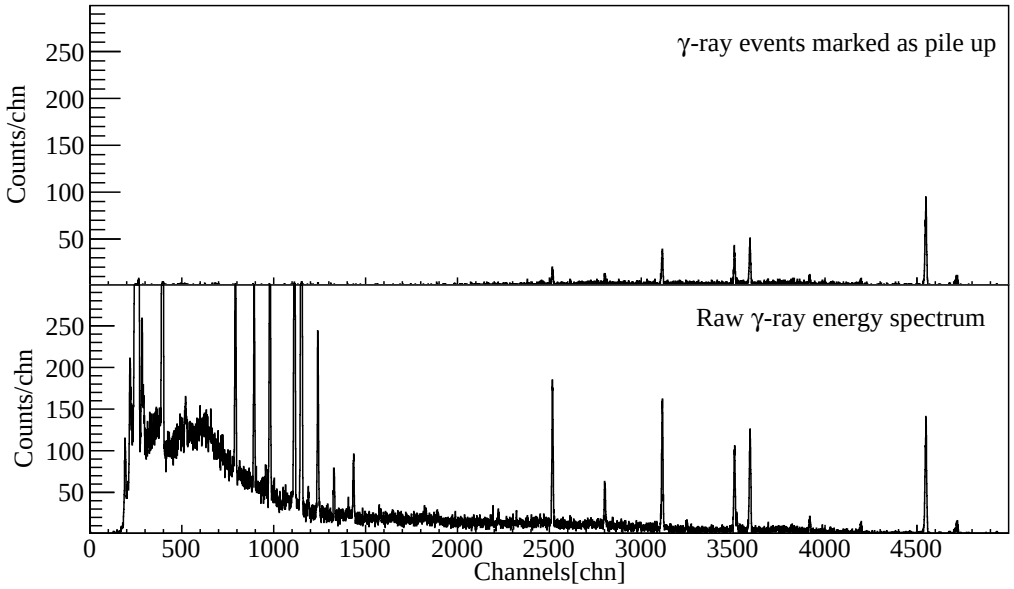

FIGURE 5.11 γ-ray energy spectrum demonstrating false pile-up (top) and raw events (bottom).

6 SUMMARY

In this work, the ^{186}Pb nucleus was studied employing combined in-beam electron and γ-ray spectroscopy with the SAGE+RITU+GREAT+TDR experimental setup. ^{186}Pb nuclei were produced via ^{106}Pd(^{83}Kr,3n)^{186}Pb reaction and the RDT method was used. Detailed analysis was based on γ-γ and γ-electron coincidence data.

The results obtained challenge the previous interpretation of the deformation of the band-head states. These results provide additional information for the theoretical calculations in the neutron-deficient Pb region. The estimated configuration mixing between the 4^+ and 2^+ non-yrast and yrast states is small based on the information obtained from the interband $4_2^+ \rightarrow 4_1^+$ and $2_2^+ \rightarrow 2_1^+$ transitions. In this work, the obtained small configuration mixing between yrast and non-yrast states is well in line with results obtained in the lifetime measurements by Grahn *et al.* [23]. The VMI-calculations suggest that the yrast and non-yrast 4^+, 2^+ and 0^+ states are pushed down in energy. This indicates a third structure interacting with these two states or the limitation of VMI-calculations in this region.

Further experiments are needed to obtain better understanding of competing structures in ^{186}Pb. The Coulex experiments at HIE-ISOLDE using the SPEDE spectrometer in conjunction with MINIBALL may be the way to solve this conundrum. Via Coulex, it is possible to excite the low-spin states rather than high-spin states which are more favourably fed in the fusion-evaporation reaction. However, while Coulex on ^{188}Pb has been performed, it is still a challenge to produce ^{186}Pb nuclei with large enough yields for post-acceleration to be studied *e.g.* at the MINIBALL spectrometer.

It is important to obtain the level-energy systematics for the neutron-deficient Pb nuclei to understand the underlying mechanisms in this region. Experiments employing the SAGE spectrometer have been performed for ^{188}Pb and ^{190}Pb to investigate the $I \rightarrow I$ interband transitions and to probe the 0^+ band-head

states. Moreover, in-beam γ-ray spectroscopic measurements for lighter Pb nuclei, ^{184}Pb, ^{182}Pb and ^{180}Pb have also been performed. Unfortunately, the cross-section of fusion-evaporation reaction to produce ^{184}Pb is so low that drastically more beam time or higher γ-ray detection efficiency would be needed in-order to get a sufficient data to further our understanding of these nuclei.

Since commissioning of the JUROGAM 3 germanium array in the Accelerator Laboratory of Jyväskylä, 26 experiments were performed by 2021. To date, the array was used in conjunction with the MARA separator, allowing to explore nuclei close to the proton drip-line and $N \approx Z$ nuclei.

This development also made it possible to use the SAGE spectrometer in conjunction with the MARA vacuum separator. This allowed for operating SAGE without the easily breaking carbon foil unit between the target and the silicon detector chamber. This was demonstrated in series of successful experiments studying nuclei in the neutron-deficient lead region in the summer of 2021.

REFERENCES

[1] M. G. Mayer. *Phys. Rev.*, **78**, 16 (1950). ISSN 0031899X. doi:10.1103/PhysRev.78.16.

[2] A. Bohr and B. R. Mottelson. *Nuclear Structure, Vol. II: Nuclear Deformations*, vol. 62. World Scientific Publishing Company (1977). ISBN 9810239807. doi:10.13182/nse77-a15221.

[3] M. Bender, P. Bonche, T. Duguet and P. H. Heenen. *Phys. Rev. C*, **69**, 064303 (2004). ISSN 05562813. doi:10.1103/PhysRevC.69.064303.

[4] V. Hellemans, R. Fossion, S. De Baerdemacker and K. Heyde. *Phys. Rev. C.*, **71**, 1 (2005). ISSN 1089490X. doi:10.1103/PhysRevC.71.034308.

[5] T. Otsuka, M. Honma, T. Mizusaki, N. Shimizu and Y. Utsuno. *Prog. Part. Nucl.*, **47**, 319 (2001). ISSN 01466410. doi:10.1016/S0146-6410(01)00157-0.

[6] J. Magill, R. Dreher and Z. Sóti. *Karlsruhe Nuclide Chart Online ,KNCO++* (2022).

[7] K. Heyde and J. L. Wood. *Rev. Mod. Phys.*, **83**, 1467 (2011). ISSN 00346861. doi:10.1103/RevModPhys.83.1467.

[8] A. N. Andreyev, M. Huyse, P. V. Duppen, L. Weissman, D. Ackermann, J. Gerl, F. P. Heûberger, S. Hofmann, A. Kleinbo, S. Reshitko, C. Schlegel, H. Schaffner, P. Cagarda and G. Mu. *Nature*, **405**, 186 (2000). doi:10.1038/35013012.

[9] J. Pakarinen, I. G. Darby, S. Eeckhaudt, T. Enqvist, T. Grahn, P. T. Greenlees, V. Hellemans, K. Heyde, F. Johnston-Theasby, P. Jones, R. Julin, S. Juutinen, H. Kettunen, M. Leino, A. P. Leppänen, P. Nieminen, M. Nyman, R. D. Page, P. M. Raddon, P. Rahkila, C. Scholey, J. Uusitalo and R. Wadsworth. *Phys. Rev. C*, **72**, 11304 (2005). doi:10.1103/PhysRevC.72.011304.

[10] J. Pakarinen, V. Hellemans, R. Julin, S. Juutinen, K. Heyde, P. H. Heenen, M. Bender, I. G. Darby, S. Eeckhaudt, T. Enqvist, T. Grahn, P. T. Greenlees, F. Johnston-Theasby, P. Jones, H. Kettunen, M. Leino, A. P. Leppänen, P. Nieminen, M. Nyman, R. D. Page, P. M. Raddon, P. Rahkila, C. Scholey, J. Uusitalo and R. Wadsworth. *Phys. Rev. C*, **75**, 1 (2007). ISSN 1089490X. doi:10.1103/PhysRevC.75.014302.

[11] J. Pakarinen, J. Ojala, P. Ruotsalainen, H. Tann, H. Badran, T. Calverley, J. Hilton, T. Grahn, P. T. Greenlees, M. Hytönen, A. Illana, A. Kauppinen, M. Luoma, P. Papadakis, J. Partanen, K. Porras, M. Puskala, P. Rahkila, K. Ranttila, J. Sarén, M. Sandzelius, S. Szwec, J. Tuunanen, J. Uusitalo and

G. Zimba. *Eur. Phys. J. A*, **56** (2020). ISSN 1434601X. doi:10.1140/epja/s10050-020-00144-6.

[12] K. Heyde. *Basic Ideas and Concepts in Nuclear Physics*. IOP Publishing Ltd 1994,1999 (1999). ISBN 0750405347.

[13] J. Suhonen. *From Nucleons to Nucleus*. Springer Berlin Heidelberg, New York (2007). ISBN 9783540488590.

[14] T. Kibédi, T. W. Burrows, M. B. Trzhaskovskaya, P. M. Davidson and C. W. Nestor. *Nucl. Instrum. Methods Phys. Res. A*, **589**, 202 (2008). ISSN 01689002. doi:10.1016/j.nima.2008.02.051.

[15] J. L. Wood, E. F. Zganjar, C. De Coster and K. Heyde. *Nucl. Phys. A*, **651**, 323 (1999). ISSN 03759474. doi:10.1016/S0375-9474(99)00143-8.

[16] T. Kibédi, A. B. Garnsworthy and J. L. Wood. *Prog. Part. Nucl.*, **123**, 103930 (2022). ISSN 01466410. doi:10.1016/j.ppnp.2021.103930.

[17] E. L. Church and J. Weneser. *Phys. Rev.*, **103**, 1035 (1956). ISSN 0031899X. doi:10.1103/PhysRev.103.1035.

[18] J. T. Dowie, T. Kibédi, T. K. Eriksen and A. E. Stuchbery. *At. Data Nucl. Data Tables*, **131**, 101283 (2020). ISSN 10902090. doi:10.1016/j.adt.2019.06.002.

[19] R. S. Hager and E. C. Seltzer. *Nucl. Data Sheets Section A*, **6**, 1 (1969). ISSN 0550306X. doi:10.1016/S0550-306X(69)80002-9.

[20] D. A. Bell, C. E. Aveledo, M. G. Davidson and J. P. Davidson. *Can. J. Phys.*, **48**, 2542 (1970). ISSN 0008-4204. doi:10.1139/p70-318.

[21] R. F. Casten. *Nuclear Structure from a Simple Perspective*. Oxford University Press, Inc., Oxford (1990). ISBN 0195045998.

[22] K. S. Krane. *Introductory Nuclear Physics*, vol. 2. John Wiley and Sons. (1988). ISBN 047180553X.

[23] T. Grahn, A. Dewald, O. Möller, R. Julin, C. W. Beausang, S. Christen, I. G. Darby, S. Eeckhaudt, P. T. Greenlees, A. Görgen, K. Helariutta, J. Jolie, P. Jones, S. Juutinen, H. Kettunen, T. Kröll, R. Krücken, Y. L. Coz, M. Leino, A. P. Leppänen, P. Maierbeck, D. A. Meyer, B. Melon, P. Nieminen, M. Nyman, R. D. Page, J. Pakarinen, P. Petkov, P. Rahkila, B. Saha, M. Sandzelius, J. Sarén, C. Scholey and J. Uusitalo. *Phys. Rev. Lett.*, **97**, 186 (2006). ISSN 00319007. doi:10.1103/PhysRevLett.97.062501.

[24] K. Wrzosek-Lipska, K. Rezynkina, N. Bree, M. Zielińska, L. P. Gaffney, A. Petts, A. Andreyev, B. Bastin, M. Bender, A. Blazhev, B. Bruyneel, P. A. Butler, M. P. Carpenter, J. Cederkäll, E. Clément, T. E. Cocolios, A. N. Deacon,

J. Diriken, A. Ekström, C. Fitzpatrick, L. M. Fraile, C. Fransen, S. J. Freeman, J. E. García-Ramos, K. Geibel, R. Gernhäuser, T. Grahn, M. Guttormsen, B. Hadinia, K. Hadyńska-Klek, M. Hass, P. H. Heenen, R. D. Herzberg, H. Hess, K. Heyde, M. Huyse, O. Ivanov, D. G. Jenkins, R. Julin, N. Kesteloot, T. Kröll, R. Krücken, A. C. Larsen, R. Lutter, P. Marley, P. J. Napiorkowski, R. Orlandi, R. D. Page, J. Pakarinen, N. Patronis, P. J. Peura, E. Piselli, L. Próchniak, P. Rahkila, E. Rapisarda, P. Reiter, A. P. Robinson, M. Scheck, S. Siem, K. Singh Chakkal, J. F. Smith, J. Srebrny, I. Stefanescu, G. M. Tveten, P. Van Duppen, J. Van de Walle, D. Voulot, N. Warr, A. Wiens and J. L. Wood. *Eur. Phys. J. A*, **55** (2019). ISSN 1434601X. doi:10.1140/epja/i2019-12815-2.

[25] M. Goldhaber and A. W. Sunyar. *Phys. Rev.*, **83**, 906 (1951). ISSN 0031899X. doi:10.1103/PhysRev.83.906.

[26] A. Bohr and B. R. Mottelson. *Phys. Rev.*, **89**, 316 (1953). ISSN 0031899X. doi:10.1103/PhysRev.89.316.

[27] A. Bohr and B. R. Mottelson. *Phys. Rev.*, **90**, 717 (1953). ISSN 0031899X. doi:10.1103/PhysRev.90.717.2.

[28] M. A. Mariscotti, G. Scharff-Goldhaber and B. Buck. *Phys. Rev.*, **178**, 1864 (1969). ISSN 0031899X. doi:10.1103/PhysRev.178.1864.

[29] S. M. Harris. *Phys. Rev.*, **138** (1965). ISSN 0031899X. doi:10.1103/PhysRev.138.B509.

[30] T. Kibédi, G. D. Dracoulis, A. P. Byrne and P. M. Davidson. *Nucl. Phys. A*, **567**, 183 (1994). ISSN 03759474. doi:10.1016/0375-9474(94)90733-1.

[31] K. Heyde and J. L. Wood. *Physica Scripta*, **91** (2016). ISSN 14024896. doi:10.1088/0031-8949/91/8/083008.

[32] P. Virtanen, R. Gommers, T. E. Oliphant, M. Haberland, T. Reddy, D. Cournapeau, E. Burovski, P. Peterson, W. Weckesser, J. Bright, S. J. van der Walt, M. Brett, J. Wilson, K. J. Millman, N. Mayorov, A. R. Nelson, E. Jones, R. Kern, E. Larson, C. J. Carey, I. Polat, Y. Feng, E. W. Moore, J. VanderPlas, D. Laxalde, J. Perktold, R. Cimrman, I. Henriksen, E. A. Quintero, C. R. Harris, A. M. Archibald, A. H. Ribeiro, F. Pedregosa, P. van Mulbregt, A. Vijaykumar, A. P. Bardelli, A. Rothberg, A. Hilboll, A. Kloeckner, A. Scopatz, A. Lee, A. Rokem, C. N. Woods, C. Fulton, C. Masson, C. Häggström, C. Fitzgerald, D. A. Nicholson, D. R. Hagen, D. V. Pasechnik, E. Olivetti, E. Martin, E. Wieser, F. Silva, F. Lenders, F. Wilhelm, G. Young, G. A. Price, G. L. Ingold, G. E. Allen, G. R. Lee, H. Audren, I. Probst, J. P. Dietrich, J. Silterra, J. T. Webber, J. Slavič, J. Nothman, J. Buchner, J. Kulick, J. L. Schönberger, J. V. de Miranda Cardoso, J. Reimer, J. Harrington, J. L. C. Rodríguez, J. Nunez-Iglesias, J. Kuczynski, K. Tritz, M. Thoma, M. Newville, M. Kümmerer,

M. Bolingbroke, M. Tartre, M. Pak, N. J. Smith, N. Nowaczyk, N. Shebanov, O. Pavlyk, P. A. Brodtkorb, P. Lee, R. T. McGibbon, R. Feldbauer, S. Lewis, S. Tygier, S. Sievert, S. Vigna, S. Peterson, S. More, T. Pudlik, T. Oshima, T. J. Pingel, T. P. Robitaille, T. Spura, T. R. Jones, T. Cera, T. Leslie, T. Zito, T. Krauss, U. Upadhyay, Y. O. Halchenko and Y. Vázquez-Baeza. *Nature Methods*, **17**, 261 (2020). ISSN 15487105. doi:10.1038/s41592-019-0686-2.

[33] J. Pakarinen, P. Papadakis, J. Sorri, R. D. Herzberg, P. T. Greenlees, P. A. Butler, P. J. Coleman-Smith, D. M. Cox, J. R. Cresswell, P. Jones, R. Julin, J. Konki, I. H. Lazarus, S. C. Letts, A. Mistry, R. D. Page, E. Parr, V. F. Pucknell, P. Rahkila, J. Sampson, M. Sandzelius, D. A. Seddon, J. Simpson, J. Thornhill and D. Wells. *Eur. Phys. J. A*, **50**, 1 (2014). ISSN 1434601X. doi:10.1140/epja/i2014-14053-6.

[34] M. Leino, J. Äystö, T. Enqvist, P. Heikkinen, A. Jokinen, M. Nurmia, A. Ostrowski, W. H. Trzaska, J. Uusitalo, K. Eskola, P. Armbruster and V. Ninov. *Nucl. Instrum. Methods Phys. Res. B*, **99**, 653 (1995). doi:10.1016/0168-583X(94)00573-7.

[35] E. Liukkonen. *Cyclotrons And Their Applications-Proceedings Of The13th International Conference, Vancouver, 1992*, page 22 (1993).

[36] R. S. Simon, K.-H. Schmidt, F. P. Hebberger, S. Hlavac, M. Honusek, G. Miinzenberg, H.-G. Clerc, U. Gollerthan and W. Schwab. *Z. Phys. A*, **325**, 197 (1986). doi:10.1007/BF01289651.

[37] E. S. Paul, P. J. Woods, T. Davinson, R. D. Page, P. J. Sellin, C. W. Beausang, R. M. Clark, R. A. Cunningham, S. A. Forbes, D. B. Fossan, A. Gizon, J. Gizon, K. Hauschild, I. M. Hibbert, A. N. James, D. R. Lafosse, I. Lazarus, H. Schnare, J. Simpson, R. Wadsworth and M. P. Waring. *Phys. Rev. C*, **51** (1995). doi:10.1103/PhysRevC.51.78.

[38] I. H. Lazarus, D. E. Appelbe, P. A. Butler, P. J. Coleman-Smith, J. R. Cresswell, S. J. Freeman, R. D. Herzberg, I. Hibbert, D. T. Joss, S. C. Letts, R. D. Page, V. F. Pucknell, P. H. Regan, J. Sampson, J. Simpson, J. Thornhill and R. Wadsworth. *IEEE Trans. Nucl. Sci*, **48**, 567 (2001). ISSN 00189499. doi:10.1109/23.940120.

[39] C. W. Beausang, S. A. Forbes, P. Fallon, P. J. Nolan, P. J. Twin, J. N. Mo, J. C. Lisle, M. A. Bentley, J. Simpson, F. A. Beck, D. Curien, G. DeFrance, G. Duchêne and D. Popescu. *Nucl. Instrum. Methods Phys. Res. A*, **313**, 37 (1992). ISSN 0168-9002. doi:10.1016/0168-9002(92)90084-H.

[40] C. Rossi-Alvarez. *Nucl. Phys. News*, **3** (1993). doi:0.1080/10506899308221154.

[41] R. D. Page, A. N. Andreyev, D. E. Appelbe, P. A. Butler, S. J. Freeman, P. T. Greenlees, R. D. Herzberg, D. G. Jenkins, G. D. Jones, P. Jones, D. T. Joss, R. Julin, H. Kettunen, M. Leino, P. Rahkila, P. H. Regan, J. Simpson,

J. Uusitalo, S. M. Vincent and R. Wadsworth. *Nucl. Instrum. Methods Phys. Res. B*, **204**, 634 (2003). ISSN 0168583X. doi:10.1016/S0168-583X(02)02143-2.

[42] A. Georgiev and W. Gast. *IEEE Trans. Nucl. Sci*, **40**, 770 (1993). ISSN 15581578. doi:10.1109/23.256659.

[43] P. Rahkila. *Nuclear Instruments and Methods in Physics Research, Section A: Accelerators, Spectrometers, Detectors and Associated Equipment*, **595**, 637 (2008). ISSN 01689002. doi:10.1016/j.nima.2008.08.039.

[44] R. Fossion, K. Heyde, G. Thiamova and P. Van Isacker. *Phys. Rev. C*, **67**, 7 (2003). ISSN 1089490X. doi:10.1103/PhysRevC.67.024306.

[45] V. Hellemans, S. De Baerdemacker and K. Heyde. *Phys. Rev. C*, **77**, 64324 (2008). doi:10.1103/PhysRevC.77.064324.

[46] A. M. Baxter, A. P. Byrne, G. D. Dracoulis, R. V. Janssens, I. G. Bearden, R. G. Henry, D. Nisius, C. N. Davids, T. L. Khoo, T. Lauritsen, H. Penttilä, D. J. Henderson and M. P. Carpenter. *Phys. Rev. C*, **48**, 2140 (1993). ISSN 05562813. doi:10.1103/PhysRevC.48.R2140.

[47] J. Heese, K. H. Maier, H. Grawe, J. Grebosz, H. Kluge, W. Meczynski, M. Schramm, R. Schubart, K. Spohr and J. Styczen. *Phys. Lett. B.*, **302**, 390 (1993). ISSN 03702693. doi:10.1016/0370-2693(93)90415-E.

[48] W. Reviol, C. J. Chiara, O. Pechenaya, D. G. Sarantites, P. Fallon and A. O. Macchiavelli. *Phys. Rev. C.*, **68**, 5 (2003). ISSN 1089490X. doi:10.1103/PhysRevC.68.054317.

[49] T. Grahn, A. Dewald, O. Möller, R. Julin, C. W. Beausang, S. Christen, I. G. Darby, S. Eeckhaudt, P. T. Greenlees, A. Görgen, K. Helariutta, J. Jolie, P. Jones, S. Juutinen, H. Kettunen, T. Kröll, R. Krücken, Y. L. Coz, M. Leino, A. P. Leppänen, P. Maierbeck, D. A. Meyer, B. Melon, P. Nieminen, M. Nyman, R. D. Page, J. Pakarinen, P. Petkov, P. Rahkila, B. Saha, M. Sandzelius, J. Sarén, C. Scholey, J. Uusitalo, M. Bender and P. H. Heenen. *Nucl. Phys. A*, **801**, 83 (2008). ISSN 03759474. doi:10.1016/j.nuclphysa.2008.01.002.

[50] J. Pakarinen, P. Greenlees, U. Jakobsson, M. Sandzelius, T. Grahn, A. Herzan, P. Ruotsalainen, K. Auranen, R. Julin, P. Papadakis and Others. *JYFL-ACCLAB-S12 Probing the E0 transitions in 186Pb using the SAGE spectrometer* (2022). doi:10.23729/a6444894-5fe7-4683-a9d5-a8ff1e28208b.

[51] J. Sarén, J. Uusitalo, M. Leino and J. Sorri. *Nucl. Instrum. Methods Phys. Res. A*, **654**, 508 (2011). ISSN 01689002. doi:10.1016/j.nima.2011.06.068.

[52] W. H. Trzaska. *Nucl. Instrum. Methods Phys. Res. A*, **297**, 223 (1990). ISSN 01689002. doi:10.1016/0168-9002(90)91370-Q.

[53] D. C. Radford. *Nucl. Instrum. Methods Phys. Res. A*, **361**, 297 (1995). ISSN 01689002. doi:10.1016/0168-9002(95)00183-2.

[54] J. Konki. *Pro Gradu, University of Jyväskylä* (2011).

[55] P. A. Butler, P. M. Jones, K. J. Cann, J. F. Cocks, G. D. Jones, R. Julin and W. H. Trzaska. *Nucl. Instrum. Methods Phys. Res. A*, **381**, 433 (1996). ISSN 01689002. doi:10.1016/S0168-9002(96)00762-0.

[56] M. S. Basunia. *Nucl. Data Sheets*, **110**, 999 (2009). ISSN 0090-3752. doi:10.1016/j.nds.2009.04.001.

[57] C. M. Baglin. *Nucl. Data Sheets*, **99**, 1 (2003). ISSN 00903752. doi:10.1006/ndsh.2003.0007.

[58] C. M. Baglin. *Nucl. Data Sheets*, **111**, 275 (2010). ISSN 00903752. doi:10.1016/j.nds.2010.01.001.

[59] J. Wauters, N. Bijnens, H. Folger, M. Huyse, H. Y. Hwang, R. Kirchner, J. Von Schwarzenberg and P. Van Duppen. *Phys. Rev. C*, **50**, 2768 (1994). ISSN 05562813. doi:10.1103/PhysRevC.50.2768.

[60] B. Singh. *Nucl. Data Sheets*, **130**, 21 (2015). ISSN 00903752. doi:10.1016/j.nds.2015.11.002.

[61] C. R. Bingham, M. B. Kassim, M. Zhang, Y. A. Akovali, K. S. Toth, W. D. Hamilton, H. K. Carter, J. Kormicki, J. Von Schwarzenberg and M. M. Jarrio. *Phys. Rev. C*, **51**, 125 (1995). ISSN 05562813. doi:10.1103/PhysRevC.51.125.

[62] U. J. Schrewe, P. Tidemand-Petersson, G. M. Gowdy, R. Kirchner, O. Klepper, A. Płochocki, W. Reisdorf, E. Roeckl, J. L. Wood, J. Zylicz, R. Fass and D. Schardt. *Phys. Lett. B.*, **91**, 46 (1980). ISSN 03702693. doi:10.1016/0370-2693(80)90659-0.

[63] M. A. Ijaz, J. Lin, E. L. Robinson and K. S. Toth. *Phys. Rev. C.*, **14**, 264 (1976). ISSN 05562813. doi:10.1103/PhysRevC.14.264.

[64] *3rd international conference on nuclei far from stability, Cargese, France, 19-26 May 1976: Proceedings* (1976).

[65] W. Reviol, L. L. Riedinger, J. Y. Zhang, C. R. Bingham, W. F. Mueller, B. E. Zimmerman, R. V. Janssens, M. P. Carpenter, I. Ahmad, I. G. Bearden, R. G. Henry, T. L. Khoo, T. Lauritsen and Y. Liang. *Phys. Rev. C.*, **49**, R587 (1994). ISSN 05562813. doi:10.1103/PhysRevC.49.R587.

[66] G. J. Lane, G. D. Dracoulis, A. P. Byrne, P. M. Walker, A. M. Baxter, R. G. Henry, D. Nisius, C. N. Davids, T. Lauritsen, H. Penttilä, D. J. Henderson, J. A. Sheikh and W. Nazarewicz. *Phys. Lett. B.*, **324**, 14 (1994). ISSN 03702693. doi:10.1016/0370-2693(94)00073-5.

[67] J. Ojala, J. Pakarinen, P. Papadakis, J. Sorri, M. Sandzelius, D. M. Cox, K. Auranen, H. Badran, P. J. Davies, T. Grahn, P. T. Greenlees, J. Henderson, A. Herzáň, R. D. Herzberg, J. Hilton, U. Jakobsson, D. G. Jenkins, D. T. Joss, R. Julin, S. Juutinen, T. Kibédi, J. Konki, G. J. Lane, M. Leino, J. Liimatainen, C. G. McPeake, O. Neuvonen, R. D. Page, E. Parr, J. Partanen, P. Peura, P. Rahkila, J. Revill, P. Ruotsalainen, J. Sarén, C. Scholey, S. Stolze, J. Uusitalo, A. Ward and R. Wadsworth. *Communications Physics*, **5** (2022). ISSN 23993650. doi:10.1038/s42005-022-00990-4.

[68] L. A. Currie. *Analytical Chemistry*, **40**, 586 (1968). ISSN 15206882. doi:10.1021/ac60259a007.

[69] J. C. Batchelder, A. M. Hurst and M. S. Basunia. *Nuclear Data Sheets*, **183**, 1 (2022). ISSN 00903752. doi:10.1016/j.nds.2022.06.001.

[70] P. Rahkila, D. G. Jenkins, J. Pakarinen, C. Gray-Jones, P. T. Greenlees, U. Jakobsson, P. Jones, R. Julin, S. Juutinen, S. Ketelhut, H. Koivisto, M. Leino, P. Nieminen, M. Nyman, P. Papadakis, S. Paschalis, M. Petri, P. Peura, O. J. Roberts, T. Ropponen, P. Ruotsalainen, J. Sarén, C. Scholey, J. Sorri, A. G. Tuff, J. Uusitalo, R. Wadsworth, M. Bender and P.-H. Heenen. *Phys. Rev. C*, **82**, 11303 (2010). doi:10.1103/PhysRevC.82.011303.

[71] F. G. Kondev, S. Juutinen and D. J. Hartley. *Nucl. Data Sheets*, **150**, 1 (2018). ISSN 00903752. doi:10.1016/j.nds.2018.05.001.

[72] B. Singh and J. Chen. *Nucl. Data Sheets*, **169**, 1 (2020). ISSN 00903752. doi:10.1016/j.nds.2020.10.001.

[73] J. Pakarinen. *EXON-2012 Proc. Int. Symp.* (2013).

[74] T. Duguet, M. Bender, P. Bonche and P. H. Heenen. *Phys. Lett. B.*, **559**, 201 (2003). ISSN 03702693. doi:10.1016/S0370-2693(03)00330-7.

[75] B. A. Marsh, T. Day Goodacre, S. Sels, Y. Tsunoda, B. Andel, A. N. Andreyev, N. A. Althubiti, D. Atanasov, A. E. Barzakh, J. Billowes, K. Blaum, T. E. Cocolios, J. G. Cubiss, J. Dobaczewski, G. J. Farooq-Smith, D. V. Fedorov, V. N. Fedosseev, K. T. Flanagan, L. P. Gaffney, L. Ghys, M. Huyse, S. Kreim, D. Lunney, K. M. Lynch, V. Manea, Y. Martinez Palenzuela, P. L. Molkanov, T. Otsuka, A. Pastore, M. Rosenbusch, R. E. Rossel, S. Rothe, L. Schweikhard, M. D. Seliverstov, P. Spagnoletti, C. Van Beveren, P. Van Duppen, M. Veinhard, E. Verstraelen, A. Welker, K. Wendt, F. Wienholtz, R. N. Wolf, A. Zadvornaya and K. Zuber. *Nature Physics*, **14**, 1163 (2018). ISSN 1745-2473. doi:10.1038/s41567-018-0292-8.

[76] P. Van Duppen, M. Huyse and J. L. Wood. *Journal of Physics G: Nuclear and Particle Physics*, **16**, 441 (1990). ISSN 09543899. doi:10.1088/0954-3899/16/3/014.

[77] J. M. Yao, M. Bender and P. H. Heenen. *Phys. Rev. C.*, **87**, 1 (2013). ISSN 1089490X. doi:10.1103/PhysRevC.87.034322.

[78] A. Oros, K. Heyde, C. De Coster, B. Decroix, R. Wyss, B. Barrett and P. Navratil. *Nucl. Phys. A*, **645**, 107 (1999). doi:10.1016/S0375-9474(98)00602-2.

[79] K. Van de Vel, A. N. Andreyev, R. D. Page, H. Kettunen, P. T. Greenlees, P. Jones, R. Julin, S. Juutinen, H. Kankaanpää, A. Keenan, P. Kuusiniemi, M. Leino, M. Muikku, P. Nieminen, P. Rahkila, J. Uusitalo, K. Eskola, A. Hürstel, M. Huyse, Y. Le Coz, M. B. Smith, P. Van Duppen and R. Wyss. *Eur. Phys. J. A*, **17**, 167 (2003). ISSN 14346001. doi:10.1140/epja/i2003-10002-x.

[80] F. R. May, V. V. Pashkevich and S. Frauendorf. *Phys. Lett. B.*, **68**, 113 (1977). ISSN 03702693. doi:10.1016/0370-2693(77)90179-4.

[81] W. Nazarewicz. *Phys. Lett. B.*, **305**, 195 (1993). ISSN 03702693. doi:10.1016/0370-2693(93)90107-S.

[82] N. Tajima, P. Bonche, H. Flocard, P. H. Heenen and M. S. Weiss. *Nucl. Phys. A*, **551**, 434 (1993). ISSN 03759474. doi:10.1016/0375-9474(93)90456-8.

[83] R. R. Chasman, J. L. Egido and L. M. Robledo. *Phys. Lett. B.*, **513**, 325 (2001). ISSN 03702693. doi:10.1016/S0370-2693(01)00382-3.

[84] J. L. Egido, L. M. Robledo and R. R. Rodríguez-Guzmán. *Phys. Rev. Lett.*, **93**, 1 (2004). ISSN 00319007. doi:10.1103/PhysRevLett.93.082502.

[85] K. Nomura, R. Rodríguez-Guzmán, L. M. Robledo and N. Shimizu. *Phys. Rev. C.*, **86**, 1 (2012). ISSN 1089490X. doi:10.1103/PhysRevC.86.034322.

[86] N. A. Smirnova, P. H. Heenen and G. Neyens. *Phys. Lett. B.*, **569**, 151 (2003). ISSN 03702693. doi:10.1016/j.physletb.2003.07.042.

[87] P. Möller, A. J. Sierk, R. Bengtsson, H. Sagawa and T. Ichikawa. *Phys. Rev. Lett.*, **103**, 6 (2009). ISSN 00319007. doi:10.1103/PhysRevLett.103.212501.

[88] P. Papadakis, D. M. Cox, G. G. O'Neill, M. J. Borge, P. A. Butler, L. P. Gaffney, P. T. Greenlees, R. D. Herzberg, A. Illana, D. T. Joss, J. Konki, T. Kröll, J. Ojala, R. D. Page, P. Rahkila, K. Ranttila, J. Thornhill, J. Tuunanen, P. V. Duppen, N. Warr and J. Pakarinen. *European Physical Journal A*, **54**, 1 (2018). ISSN 1434601X. doi:10.1140/epja/i2018-12474-9.

[89] N. Warr, J. Van de Walle, M. Albers, F. Ames, B. Bastin, C. Bauer, V. Bildstein, A. Blazhev, S. Bönig, N. Bree, B. Bruyneel, P. A. Butler, J. Cederkäll, E. Clément, T. E. Cocolios, T. Davinson, H. De Witte, P. Delahaye, D. D. DiJulio, J. Diriken, J. Eberth, A. Ekström, J. Elseviers, S. Emhofer, D. V. Fedorov, V. N. Fedosseev, S. Franchoo, C. Fransen, L. P. Gaffney, J. Gerl,

G. Georgiev, R. Gernhäuser, T. Grahn, D. Habs, H. Hess, A. M. Hurst, M. Huyse, O. Ivanov, J. Iwanicki, D. G. Jenkins, J. Jolie, N. Kesteloot, O. Kester, U. Köster, M. Krauth, T. Kröll, R. Krücken, M. Lauer, J. Leske, K. P. Lieb, R. Lutter, L. Maier, B. A. Marsh, D. Mücher, M. Münch, O. Niedermaier, J. Pakarinen, M. Pantea, G. Pascovici, N. Patronis, D. Pauwels, A. Petts, N. Pietralla, R. Raabe, E. Rapisarda, P. Reiter, A. Richter, O. Schaile, M. Scheck, H. Scheit, G. Schrieder, D. Schwalm, M. Seidlitz, M. Seliverstov, T. Sieber, H. Simon, K. H. Speidel, C. Stahl, I. Stefanescu, P. G. Thirolf, H. G. Thomas, M. Thürauf, P. Van Duppen, D. Voulot, R. Wadsworth, G. Walter, D. Weißhaar, F. Wenander, A. Wiens, K. Wimmer, B. H. Wolf, P. J. Woods, K. Wrzosek-Lipska and K. O. Zell. *Eur. Phys. J. A*, **49**, 1 (2013). ISSN 1434601X. doi:10.1140/epja/i2013-13040-9.

[90] J. Pakarinen, P. Rahkila, A. N. Andreyev, P. A. Butler, E. S. and E. Al. *Proposal to the JYFL-PAC* (2006).

[91] D. G. Jenkins, M. Muikku, P. T. Greenlees, K. Hauschild, K. Helariutta, P. M. Jones, R. Julin, S. Juutinen, H. Kankaanpää, N. S. Kelsall, H. Kettunen, P. Kuusiniemi, M. Leino, C. J. Moore, P. Nieminen, C. D. O'Leary, R. D. Page, P. Rakhila, W. Reviol, M. J. Taylor, J. Uusitalo and R. Wadsworth. *Phys. Rev. C*, **62**, 21302 (2000). doi:10.1103/PhysRevC.62.021302.

[92] J. F. Cocks, M. Muikku, W. Korten, R. Wadsworth, S. Chmel, J. Domscheit, P. T. Greenlees, K. Helariutta, I. Hibbert, M. Houry, D. Jenkins, P. Jones, R. Julin, S. Juutinen, H. Kankaanpää, H. Kettunen, P. Kuusiniemi, M. Leino, Y. Le Coz, R. Lucas, E. Mergel, R. D. Page, A. Savelius and W. Trzaska. *Eur. Phys. J. A*, **3**, 17 (1998). ISSN 14346001. doi:10.1007/s100500050144.

[93] G. D. Dracoulis, G. J. Lane, A. P. Byrne, A. M. Baxter, T. Kibédi, A. O. Macchiavelli, P. Fallon and R. M. Clark. *Phys. Rev. C*, **67**, 5 (2003). ISSN 1089490X. doi:10.1103/PhysRevC.67.051301.

[94] G. D. Dracoulis, G. J. Lane, A. P. Byrne, T. Kibédi, A. M. Baxter, A. O. Macchiavélli, P. Fallon and R. M. Clark. *Phys. Rev. C.*, **69**, 054318 (2004). ISSN 05562813. doi:10.1103/PhysRevC.69.054318.

[95] G. D. Dracoulis, A. P. Byrne and A. M. Baxter. *Phys. Lett. B.*, **432**, 37 (1998). ISSN 03702693. doi:10.1016/S0370-2693(98)00620-0.

[96] J. Uusitalo, J. Sarén, J. Partanen and J. Hilton. *Acta Phys. Pol. B*, **50**, 319 (2019). ISSN 15095770. doi:10.5506/APhysPolB.50.319.

[97] J. Sarén. *The ion-optical design of the MARA recoil separator and absolute transmission measurements of the RITU gas-filled recoil separator*. December (2011). ISBN 9789513945114.

[98] J. Eberth and J. Simpson. *Prog. Part. Nucl.*, **60**, 283 (2008). ISSN 0146-6410. doi:10.1016/j.ppnp.2007.09.001.

[99] G. Duchêne, F. A. Beck, P. J. Twin, G. De France, D. Curien, L. Han, C. W. Beausang, M. A. Bentley, P. J. Nolan and J. Simpson. *Nucl. Instrum. Methods Phys. Res. A*, **432**, 90 (1999). ISSN 01689002. doi:10.1016/S0168-9002(99)00277-6.

[100] I. J. Kim, C. S. Park and H. D. Choi. *Appl. Radiat. Isot.*, **58**, 227 (2003). ISSN 09698043. doi:10.1016/S0969-8043(02)00295-6.

[101] G. A. Brinkman, A. H. W. Aten and J. T. Veenboer. *Int. Jour. Appl. Radiat. Isot.*, **14**, 153 (1963). ISSN 0020-708X. doi:10.1016/0020-708X(63)90110-8.

[102] R. Helmer. *Table de Radionucleides; Laboratoire National Henri Becquerel*, **62**, 1 (2010).

[103] E. Browne and J. K. Tuli. *Nucl. Data Sheets*, **114**, 1849 (2013). ISSN 00903752. doi:10.1016/j.nds.2013.11.002.

[104] A. L. Nichols. *IAEA Co-ordinated Research Project: Update of X-ray and gamma-ray decay data standards for detector calibration and other applications*, vol. 60 (2004). doi:10.1016/j.apradiso.2003.11.025.